
# Insulation coordination for a fault-ride-through test setup's 66 kV air-core reactor

Root-cause analysis and discharge mitigation

Olaf Lennard Götting

Electric Power Systems and High Voltage Engineering, EPSH4-1032, 2022-05

Master Thesis

STUDENT REPORT
AALBORG UNIVERSITY

# Insulation coordination for a fault-ride-through test setup's 66 kV air-core reactor

Root-cause analysis and discharge mitigation

Olaf Lennard Götting

Electric Power Systems and High Voltage Engineering, EPSH4-1032, 2022-05

Master Thesis

STUDENT REPORT

AALBORG UNIVERSITY

The programs that are used in this technical report are: MATLAB® R2021b and PLECS® Standalone Version 4.4.4.

AALBORG UNIVERSITY
Department of Energy Technology
Pontoppidanstræde 101
DK-9220 Aalborg
Denmark
Web address: http://www.et.aau.dk

**AAU Energy**
Aalborg University
http://www.aau.dk

**R&D Test Systems A/S**
https://www.rd-as.com/

AALBORG UNIVERSITY
STUDENT REPORT

**Title:**
Insulation coordination for a fault-ride-through test setup's 66 kV air-core reactor

**Theme:**
Master Thesis

**Project Period:**
Spring Semester 2022

**Project Group:**
EPSH4-1032

**Participant(s):**
Olaf Lennard Götting

**Supervisor(s):**
Claus Leth Bak (AAU)
Filipe Faria da Silva (AAU)
Morten Virklund Pedersen (R&D)

**Page Numbers:** 99

**Date of Completion:**
May 29, 2022

**Abstract:**

The air-core auto-transformer in a 66 kV fault ride through test setup for wind turbines is prone to discharges. Their root-cause is identified as switching overvoltages (OV) due to current chopping (CC).
The coil is modelled as an equivalent circuit using analytically calculated parameters. A simulation in the time domain shows significant OV with a magnitude of up to 11 p.u..
A comprehensive discussion on potential counter-measures proposes a snubber circuit as a feasible solution to mitigate the discharges. The OV is defined by the snubber's RC component and the magnitude of CC.
The simulation results show that the OV is reduced to less than 2 p.u. by including the snubber circuit. As future work, a measurement campaign to determine the value of the chopping current is suggested.

# Summary


### Introduction and problem description

Wind turbines have to be tested to be compliant with regulations regarding their fault-ride-through (FRT) capability, i.e. their ability to stay connected to the grid in various abnormal operating conditions resulting from faults. For this purpose a FRT test has been developed and set up by R&D Test Systems A/S in northern Denmark. The test setup's heart is an air-core inductor rated for 72.5 kV with various taps to set the desired residual voltages and short-circuit ratios. Therefore, the coil is used an auto-transformer. To emulate the fault conditions, $SF_6$ puffer type circuit breakers (CB) are used as event switches. A simplified single line diagram of the setup is presented in Figure 1.1.

During the commissioning and operation of the FRT tester discharges in radial direction at the coils side were observed by the staff at site. These discharges were in timely correlation with the operation of the event switches. As these will significantly decrease the coil's insulation's lifetime and also pose a fire hazard, R&D Test Systems A/S sees the urgent necessity to find the root cause as well as effective and adequate counter measures.

### Root cause analysis

Initially, it is thus necessary, to carry out a comprehensive discussion on potential root causes of this problem, as performed in Chapter 2. Different failure modes were discussed and conclusions drawn regarding their projected severity: Quasi-stationary voltage stress, surface discharges due to pollution, transients introduced by switching activity and internal resonances in the coil

After a comprehensive discussion, it was found that switching transients due to current chopping (CC) and the severe overvoltages caused by this effect pose a hazard in this application. CC occurs when the current through a CB in the opening operation is interrupted before the current's natural zero-crossing. Mainly, this is the case for inductive currents of small magnitude. The CB deployed is rated for a maximum breaking current of 40 kA while the currents in the FRT test setup are in the range of 60 A to 2 kA. The reasoning is based on the mismatch between

the CB's rated values and the actually observed currents, leading to the risk of CC since the CB is overrated. Internal resonances could be excited by the transients, causing higher stresses in sections of the coil.

### Computer model of the FRT setup

The coil is modelled by an equivalent circuit, presented in Figure 3.2. The circuits components are calculated analytically and lump multiple turns together. The coil model's frequency response represents measured sweep frequency response analysis (SFRA) data well. Due to limited data available, the CB had to be modelled as an ideal switch, which opens at a defined chopping current value $i_c = 7\ A$. The development of the model is presented in Chapter 3 and the beginning of Chapter 4. The measurement results in Chapter 4 show that the defined CC leads to overvoltages (OV) with a magnitude of 11 p.u. and a very small rate of decay. Internal resonances were observed, but their magnitude is small compared to the overall OV.

### Counter measures against discharges

Chapter 5 is dedicated to finding an effective counter-measure against the discharges. A comprehensive discussion including various measures to increase the insulation's strength or decreasing the stress on the insulation found that a snubber circuit with adequately selected components poses a promising solution. The snubber circuit consists mainly of a RC-element. Often, it is protected by a fuse and a surge arrester. Its functionality is based upon the RC-element offering an alternative path for the current through the coil in the event of CC. The OV's magnitude is then dependent on the values for $i_c$ and the RC-element. A drawback of this solution is the leakage current around the coil during stationary operation. Section 5.4 proposes an algorithm based on mathematical optimisation to find a solution giving rise to a limited OV (less than 2 p.u.) and leakage current limited to 7.7 % of the coil's current.

### Future work

The final chapter 6 outlines relevant future tasks to mitigate the discharges in the FRT tester in reality. These mainly include measurements to determine the actual value of the chopping current to allow the correct determination of the snubber parameters. Furthermore, the snubber's impact on the FRT tests has to be prudently assessed. Additionally, the comprehensive discussion in Chapter 5 found alternative, equally promising mitigation methods (e.g. exchanging the CB). These were dismissed solely due to the model's limitations in this project. It is thus suggested to investigate these methods in detail.

# Preface

This Master Thesis is conducted by a student in the 10th and final semester at Aalborg University as a part of the Electrical Power Systems and High Voltage Engineering Master's program. The work was carried out in cooperation with R&D Test Systems A/S.

The author is delighted to thank Morten Virklund Pedersen, Rayk Grune and Michael Hejsel Hansen from R&D Test Systems A/S for the interesting project proposal, inspiring technical discussions, friendly guidance and a overall highly valuable and enjoyable experience. Also, the student is grateful to Claus Leth Bak and Filipe Faria da Silva from Aalborg University for sharing their valuable knowledge in interesting technical discussions and constructive feedback on this report.

## Readers guide

Figures and tables in the report are numbered within the respective chapter. The first digit indicates the number of the chapter, while the second digits stand for the number of the figure inside the chapter (e.g. Figure 2.3 is the third figure in the second chapter). Explanatory text is found below the given figures and tables. Figures without reference are created by the author.

On page **ix**, a Table of Contents is given. When viewing this report as a PDF, hyperlinks in the table of contents will allow fast navigation to the desired sections. Page **vii** displays a Nomenclature listing the Acronyms, as well as the variables and their respective units used in this report. Additionally, a List of Figures is found on page **xi**, facilitating the navigation in the report.

The bibliography can be found on page 65. The entries are sorted in order of their appearance in the text. The appendices can be found after the bibliography and are labelled with letters. If a source is used to cite a specific piece of information, the source will appear before the period [source no.]. This may also refer to information cited inside the entire paragraph.

Aalborg University, May 29, 2022

# Contents

# Chapter 1

# Introduction

*This chapter introduces the fault-ride-through test setup and outlines the poblematic discharges observed at its auto-transformer. Afterwards, the problem is stated and the objective as well as the methodology, scope and limitations outlined.*

## 1.1 Background

Wind turbine generators (WTG) are obliged to meet grid codes at the point of connection to the electric power system. These grid codes concern various aspects of the WTG's operation. One aspect is the fault ride through (FRT) operation. Faults in the gird, e.g. a failure of cable insulation, will distort the voltage in the vicinity of the fault. To reduce the area of impact and to allow the protection system to detect the fault, it is necessary that the generators supply a short circuit current. FRT operation can be separated into low voltage (LV) and high voltage (HV) ride through (LVRT and HVRT, respectively), aimed at supporting the grids recovery from voltage dips and swells [1]–[4].

It is imperative for the manufacturers to carry out and document comprehensive tests before introducing a new WTG to the market, of which the FRT tests are one aspect. To allow comprehensive FRT testing in various grid conditions (e.g. different magnitudes of voltage, short circuit power and grid impedance) designated FRT test setups are used to emulate grid faults, decoupled from the public power system.

A FRT test setup developed by R&D Test Systems A/S [5] and deployed in northern Denmark is based on an air-core reactor, which resembles an auto-transformer with 29 taps to set the desired impedance and residual voltage. Figure 1.1 presents a simplified single-line diagram of the setup. In case both event switches E1 and E2 are open, the coil acts as a impedance between WTG and the external 66kV-grid. The event switches allow to emulate voltage dips or swells, depending on the tap configuration. In this case the coil is used as an auto-transformer, with the common winding section between the DUT and event switch connection.

The FRT testing procedure usually involves closing one of the event switches for a short time and then reopening it again. The time during which the switch is closed is typically less than one second. So called double-dip faults are created by closing first one and then the second switch shortly afterwards. Different tapping positions allow to set various values of residual voltage and short-circuit impedance. As circuit breakers for the two event switches, $SF_6$ breakers are used (Details in Table A.2).

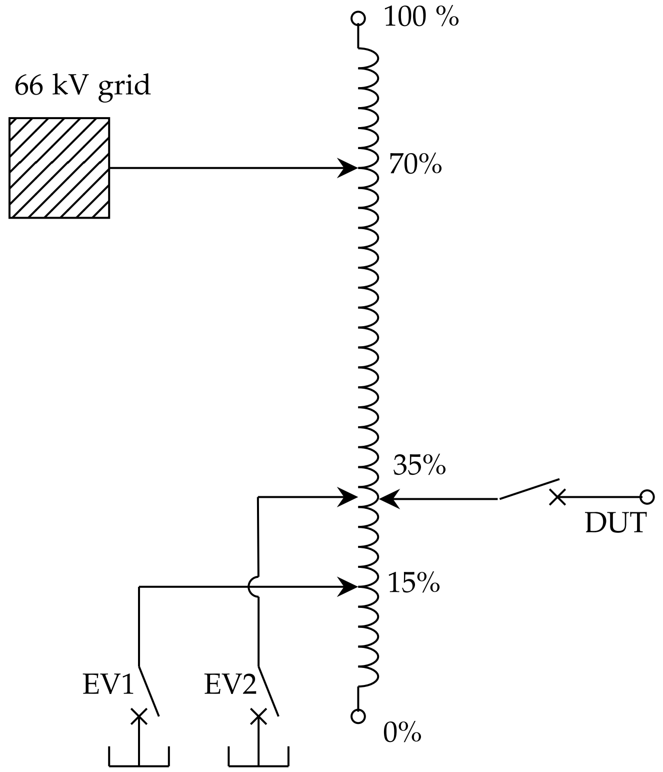


**Figure 1.1:** Simplified single-line diagram of FRT tester with exemplary tap configuration

## 1.2 Technical data and coil's construction

The most important parameters of the coil are presented in Table A.1 in Appendix A. The three coils (one for each phase) mainly consist of aluminum foil and a polyester-based insulation between the turns. The coil is depicted in Figure 1.2. As shown, the coil may be subdivided into three segments (inner, middle and outer segment), separated by rings of glass-fibre reinforced plastic (GFRP). Each section consists of multiple packs, created by cooling ducts. The radial rods serve mechanical purposes, keeping the cooling duct separators, aluminum foil and insulation in place. The electrical interconnection between the three main rings is carried out using a solid copper conductor, similar to a bus bar. As a last step in the manufacturing process, a thin layer of epoxy resin was applied to impregnate the coil against humidity.

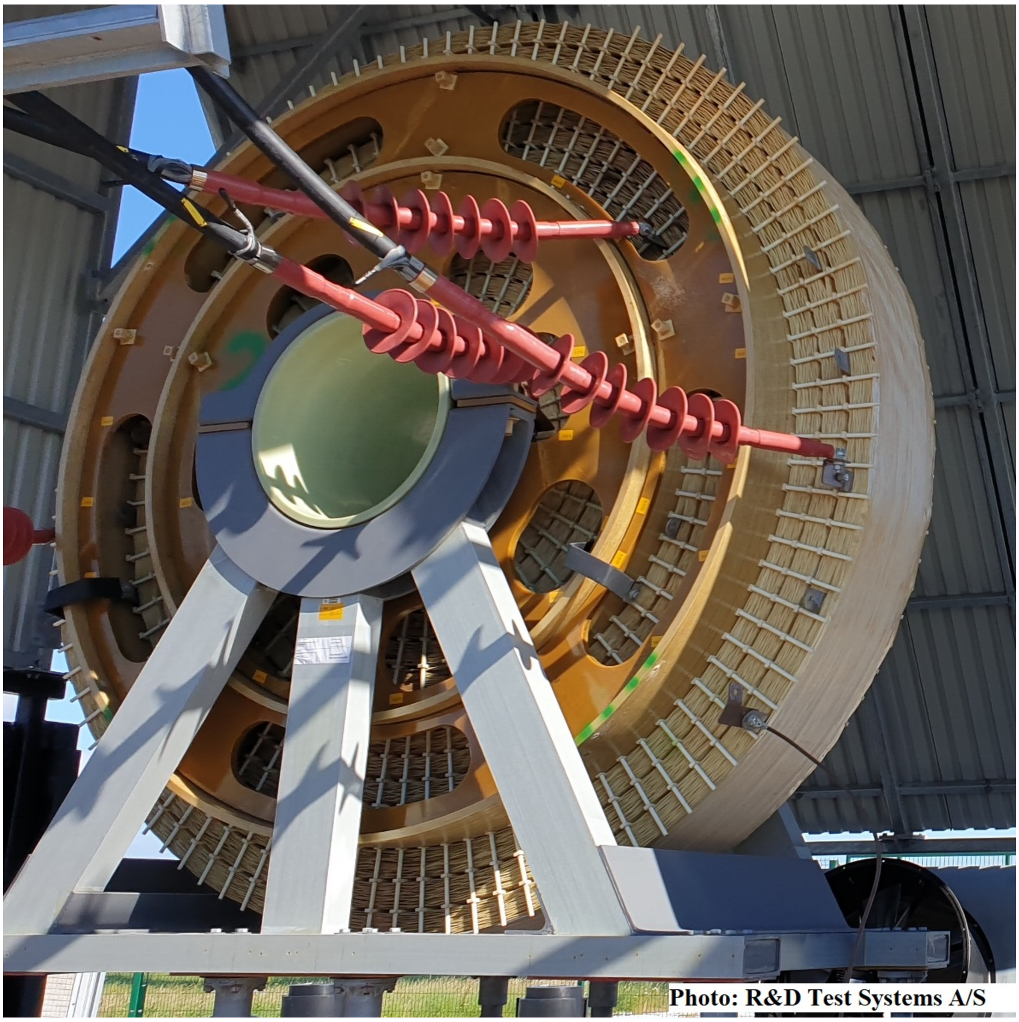


**Figure 1.2:** A picture of the single phase air-core coil used in the FRT tester

The coils were initially set up in an open-air environment in the FRT test center, as depicted in Figure 1.2. During operation, it was found that the salty and humid environmental air is beyond the defined operating conditions of the coils. Thus, the coils are now operated in an enclosure (see Figure 2.2b in Chapter 2). The impact of pollution and surface discharges are discussed in more detail in Chapter 2.3, in which also some additional counter measures against pollution are summarised.

## 1.3 Problem Formulation

During commissioning and operation of the FRT tester, discharges in radial direction on the coil's side were observed by the staff at site. An exemplary picture of the burning marks left by the discharges is presented in Figure 1.3. One of the coils also caught fire during one of these incidents. According to internal information, the discharges were a result of operating the event switches E1 or E2. A detailed description of the incidents is presented in Chapter 2. The developer of the FRT test system, R&D Test Systems A/S, thus sees the urgent necessity to investigate the cause of these discharges comprehensively. Besides the foreseeable insulation's degradation, the discharges can also pose a fire hazard. Thus, it is of great interest for the company to find adequate counter measures. This leads to the below phrased research question:

**Which effect causes the discharges observed at the coils during operation of the FRT test setup and which measures are feasible to mitigate them in future?**

**Figure 1.3:** Picture of burning marks left by a discharge on the coil (after cleaning the radial bars)

## 1.4 Objective

The first objective of this project is to analyse the discharge incidents in detail and formulate a justified hypothesis on the root-cause. Afterwards, based on the result of this analysis, a more detailed study has to be carried out in order to support the originally formulated hypothesis.

The main objective is then to provide R&D Test Systems A/S with a road map of adequate measures against the discharges. These counter-measures can be suggested by the means of computer simulation and verified by experimental analysis. The justification of counter-measures has great importance for R&D Test Systems A/S as their deployment on site can require a significant financial investment. This aspect of justification also implies that a computer simulation has to be verified to be sufficiently accurate. These objectives condense to the below stated working questions:

- What are potential root-causes for the discharges in the FRT-Test setup?
- Which is the most likely root-cause?
- How can the impact of the adverse effects be assessed comprehensively?
- Which counter-measures are feasible to mitigate the discharges?
- Which counter-measure provides the most technically effective solution?
- How can the effectiveness be assessed and verified?

## 1.5 Methodology

The initial analysis of the incidents will be carried out based on data provided by R&D Test Systems A/S and by reviewing relevant literature. This will serve as an initial orientation in the project, based on which initial hypothesises for the root cause are formulated and investigated. In a discussion on the likelihood, the most relevant hypothesis is selected.

This root cause is then analysed in greater detail using a suitable computer simulation. If the simulation results support the previous findings, relevant counter measures can be discussed. The simulation can then be augmented to assess the effectiveness of the counter-measure proposed. Optionally, the effectiveness can also be verified by experimental investigation afterwards.

A comprehensive literature review will support finding the root-cause of the discharges, selecting an appropriate simulation approach and suggesting and assessing potential counter-measures.

## 1.6 Scope and Limitations

As the resources allocated to this project are limited, the limitations and the scope of the project have to be outlined prudently:

- Experimental investigation of any sort is time consuming and has to be thoroughly justified and planned.

- Computer simulations are subject to limitations regarding:
  - the accuracy of available data and measurement results.
  - the computational power available.
- In the initial discussion on the potential root cause, only the most relevant aspects can be considered.
- The available data on the circuit breaker is limited, imposing the use of a simplified model in the time domain simulation.
- The measurement of the current through the CB during breaking at rated voltage was not possible due to the limited time available.
- Financial aspects will not be considered.

## 1.7 Summary

This chapter introduced the FRT test setup and the construction of the coil used as an auto-transformer. The problem of discharges occurring at the coils surface as well as the desired outcome of the project was stated. Afterwards, methodology, scope and limitations of the project are outlined. In the following chapter, an analysis of the root-cause is performed.

# Chapter 2

# State of the art

*Initially, the circumstances of the discharge incidents are presented in more detail. Further, potential failure modes are comprehensively discussed, aided by relevant literature. The discussion is followed up by a short section on resonances in transformer windings, after which the conclusion is drawn.*

## 2.1 Description of discharge incidents

In this initial discussion some relevant failure mechanism of the coil's insulation are briefly discussed based on the discharge incident's description. The discussion is augmented by measuring data provided by R&D Test Systems A/S and helps to delimit the failure cause to the most relevant aspects.

| | **Incident 1** | **Incident 2** | **Incident 3** |
|---|---|---|---|
| Spark observed at Coil | L3 | L1 | L2 |
| Tap Grid | 8 (20%) | 8 (20%) | 29 (100%) |
| Tap DUT | 20 (75%) | 20 (75%) | 16 (55%) |
| Tap Event Switch 1 | 20 (75%) | 20 (75%) | - |
| Tap Event Switch 2 | 21 (75.8%) | 21 (75.8%) | 15 (50%) |

**Table 2.1:** Tap configurations of discharge incidents. Percentage of number of turns given in parentheses.

During the commissioning of the FRT test setup, three initial incidents of discharges were observed by personnel at the testing site. The incidents impacted each of the three coils (L1, L2 and L3) once. An exemplary picture of the burning marks left by a discharge is shown in Figure 1.3. The discharges in all three incidents occurred in the coil's middle section and were guided along the radial bars between the cooling ducts, judging by the burning marks. The discharges were in timely correlation with operation of the event switches. For the human observation, a differentiation of the ignition and extinction of the spark with respect to closing and opening of the event switches was not possible. Typically, the event switches are only closed for a few hundred milliseconds. The tap configuration at the coil is evident from Table 2.1.

In general, the observation of the discharge means that the stress due to the applied electric field exceeded the insulation's strength. As the coil's design seems appropriate for it's purpose at first glance, either the stress must be higher than expected, or the insulation's strength is lower than expected.

There are some relevant aspects to consider, when attempting to explain a lower insulation strength than expected:

- The insulation strength is smaller in some areas due to errors in the manufacturing process.
- The electric fields are less uniform than initially assumed.
- Moisture and pollution leads to a lower insulation strength

Also, some aspects leading to a higher stress than expected can be identified:

- In quasi-stationary operation, the influence of the tapping position leads to a voltage stress beyond specification.
- The breaking of an inductive current causes a high transient stress in the coil.
- Resonances in the coil and transients contradict the assumption of a linear voltage distribution in the coil, leading to stresses beyond specifications in some spots.

As previously mentioned, these three incidents occurred already during commissioning of the FRT Tester. As the sparks were observed at a different coil (in a different phase) each time, a coincidental manufacturing error in a single coil's insulation system can be ruled out. The other aforementioned aspects have to be analysed in more detail.

## 2.2 Quasi-stationary voltage stress

As shown in Table 2.1 and Figure 1.1, due to the tap configuration, the stationary voltage stress in sections of the coil after closing the event switch is far beyond the rated voltage of the coil: The rated voltage is applied to half of the coil, approximately. The reason is the grid being connected to the 70%-tap and the event switch to the 15%-tap. Thus, the grid voltage is applied to 55% of the coil, i.e. the section between the two taps, while the event switch is closed.

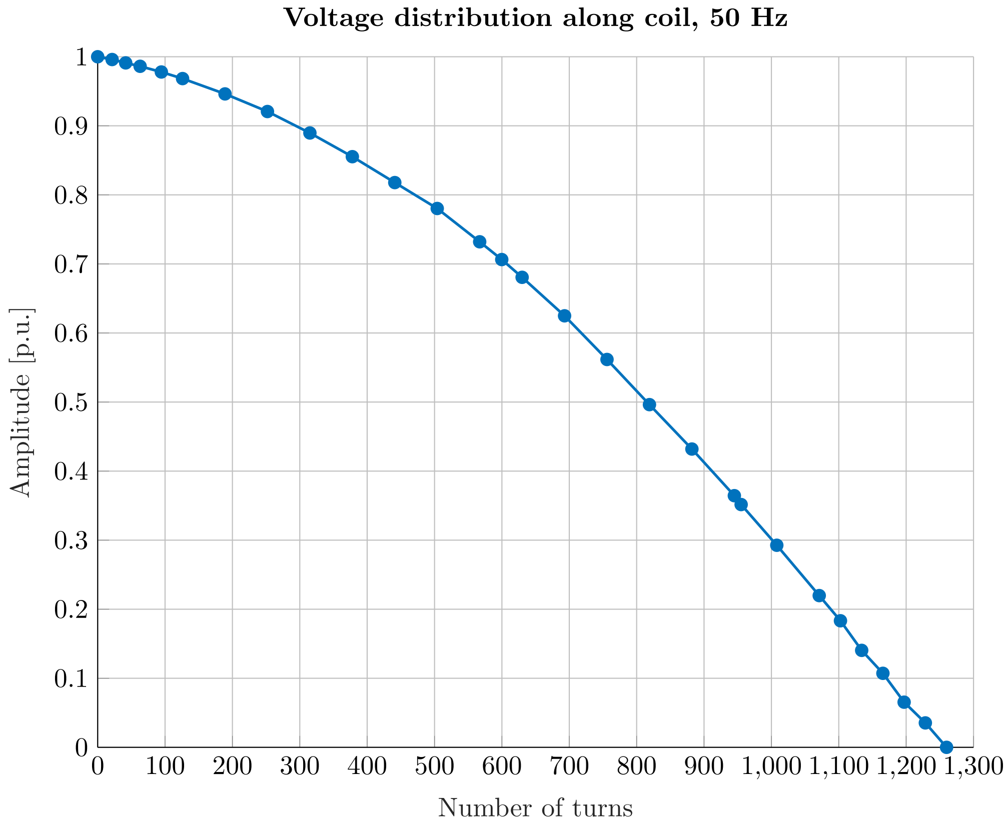


**Figure 2.1:** Voltage distribution in coil measured by manufacturer

Further, data sheets and measurements provided by the coil's manufacturer indicate a non-linear voltage distribution along the turns (see Figure 2.1). Assuming a voltage distribution following the distribution recorded by the measurements, a turn to turn voltage of approximately 70 V can be calculated for the tap configuration of incident 1. Thus, the voltage drop between cooling ducts is approximately 6.2 kV, considering the number of turns between cooling ducts in the coil's middle ring. The distance between the cooling ducts in the middle ring is approximately 63 mm. Thereby the quasi-stationary stress can be estimated with 1 kV/cm, which is far below the breakdown field strength of environmental air (25 kV/cm, [6]).

Additionally, the impact of the overhanging solid insulation has not been considered yet: In the above presented assumption, the stress found refers to the hypothetical uniform field through the windings between two cooling ducts. In reality, a discharge could not occur there, as the breakdown field strength of the solid insulation is more than 20-times higher than in air (see Table A.1). The solid insulation is overhanging the conductor by a few centimeters on each side. Thus, for a discharge to develop in air only the field strength in air with some distance to the conductor may be considered. This value will be lower than the field strength directly at the aluminum foil.

Taking the relatively low quasi-stationary field strength and the impact of the solid insulation into account, it is considered unlikely that the discharges occurred simply due to this quasi-stationary stress. This hypothesis is further supported by the observation that the discharges are occurring in timely correlation with the operation of the event switches.

## 2.3 Surface discharge due to pollution

Surface discharges due to a conductive layer of pollution is a common failure mechanism of HV insulation systems in outdoor applications. Usually, pollution layers are only conductive in wet condition. Elongating the creeping distance (also: leakage distance) and reducing the risk of a continuous conductive pollution layer on the insulator is one of the key design constraints for HV transmission line insulators [6]–[9]. The surface discharge usually follows five steps, according to [6], [7], [10]:

1. Leakage current flows through the conductive pollution layer, leading to partial drying of the pollution layer due to active power loss.

2. Formation of a non-conductive dry band with a significant voltage drop.

3. Either breakdown of the air-gap across the dry band or rewetting of the insulation and redevelopment of a leakage current.

4. Elongation of the dry band arc due to heat dissipation at its roots leading to the expansion of the dry band

5. Eventually, arc spanning the entire insulator, leading to flashover.

During the development of the arc in the gaseous insulation medium (air) it can occur that the leakage current, limited by the pollution layer's resistance, is too small to allow thermal ionisation. Thus, the arc extinguishes. Also, in systems stressed with AC voltages, the zero-crossing of the current leads to the extinction of the dry band arc. In both of these cases, either rewetting of the insulator or the repeated partial breakdown in the next voltage cycle can reignite the arc. Once the arc reaches a critical length of approximately one half to two thirds of the total insulator's length, the final flashover to the other electrode will occur, since the arc's voltage drop is small and it is in series with the remaining surface resistance [6]. Some further work has been dedicated to analyse the surface discharge mechanism and properties of the leakage current under quasi-stationary voltage stress: [11], [12].

Furthermore, impulse or transient stresses due to lightning strike, switching or resonance effects can lead to a surface discharge. In this case, according to [13]–[15], the dynamic propagation of surface discharge is characterised by its kinetic energy and propagation speed. The dynamics are of great importance here as the voltage stress is only present for a short time. Once the discharge reaches the proximity of the other electrode, it accelerates and quickly shunts the remaining insulation distance. It has to be noted that [14], [15] do not discuss polluted insulators, but surface discharges in general for different materials. A. Küchler in [7] further mentions that a impulse stresses can exacerbate existing discharges (at power frequency stress) and potentially lead to the full breakdown of an insulator.

Various of the aforementioned sources [6]–[8], [14], [15], agree that the insulation material and its properties with respect to

- surface texture and diffusion of liquid,
- surface resistance,
- hydrophobic characteristics,
- thermal or chemical degradation of the insulation surface

significantly impact the discharge mechanism.

### 2.3.1 Applicability to problem at hand

As previously outlined, the properties of the insulation material and the severity of pollution (pollution layer's conductivity, thickness and continuity [7]) greatly influence the insulation strength in polluted condition. The coil's insulation material (see Table A.1) is commonly used as slot insulation in electrical machines. Thus, the material's susceptibility to pollution and other relevant parameters are unknown, as it is normally not exposed to these conditions. Further, the severity of pollution has not been measured. A principle for the measurement of pollution severity is outlined in [6].

Additionally, the creeping distance is one of the main influencing factors. It is illustrated in Figure 2.2a, showing a picture of the winding insulation between two cooling ducts. A sketch of the insulation system is provided in Chapter 3, Figure 3.1. As evident from the picture, the minimum creeping distance is found along the radial rods between the cooling ducts thus defines the resilience against surface breakdown. The plastic rings are not considered, because they are not added in all sections of the coil. Knowing the dimensions of the coil[1], the creeping distance can be estimated with 16 cm.

[1] The dimensions are not explicitly stated in this report, as it is confidential information

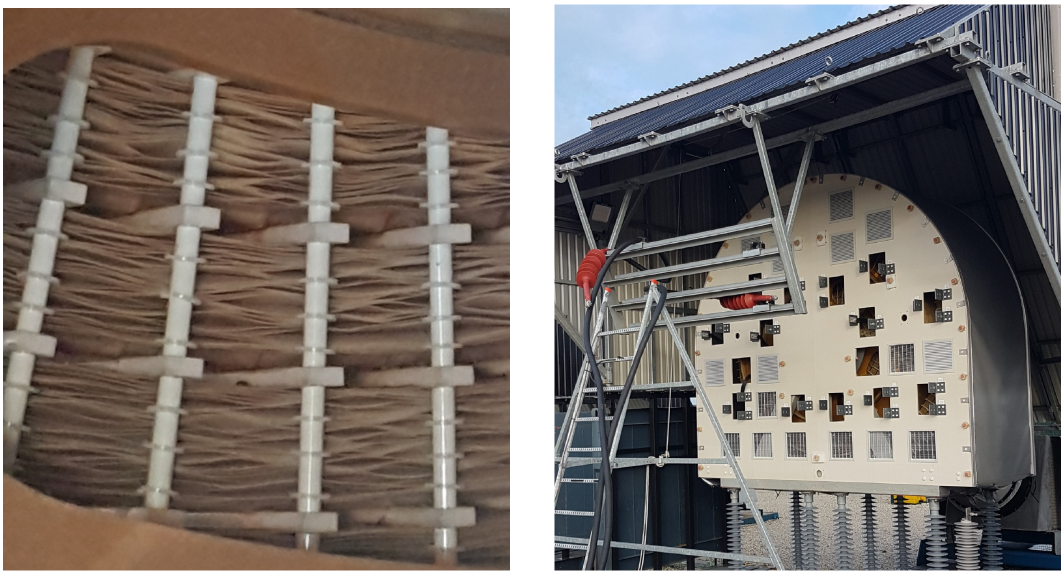

**(a)** Coil's insulation system with rings around radial rods to increase creeping distance

**(b)** Enclosure around coil as protection against pollution

**Figure 2.2:** Pictures of coils with measures against surface discharge

With regard to pollution, the test site can be classified as 'Class III' (see Chapter 9 in [6]) due to its close proximity to the sea. This implies that salty fog can pollute the insulation, creating a conductive layer. Thus, the minimum creeping distance has to be at least 25 mm/kV, based on the rated AC operating voltage, according to [6]. For a leakage distance of 16 cm, the maximum operation voltage between cooling ducts can be 6.4 kV, serving as a value for initial orientation. As estimated in Section 2.2, the voltage stress between cooling ducts in the tap configuration of incident 1 is 6.2 kV. The comparison of these values indicates that the influence of pollution has to be considered, even in quasi-stationary operation.

As aforementioned, transient stresses of the insulation system can lead to surface discharges or exacerbate existing discharges [7], [14], [15]. If the transient stress is sufficiently long, considering the surface discharge's propagation speed, it must be considered as a potential failure mechanism. However, a detailed analysis is only possible when sufficient data regarding the transient stress and the insulation's properties is available. As outlined in the following Section 2.4, the insulation system analysed is likely to be stressed by transients.

Previous to this work, some counter-measures against surface pollution have already been installed at site. These are summarised in the following.

- The coils were cleaned using low pressure water and brushes and dried afterwards.

- The coils are now operated in an enclosure, as shown in Figure 2.2b. Despite some holes for ventilation purposes and to access the taps, the severity of pollution should be reduced. Still, it is imaginable that over a long period of time critical pollution levels are reached within the enclosure.

- The coil's air cooling system was improved to lower the impact of humid and salty environmental air.
- In some critical spots, rings to elongate the creeping distance of the radial rods have been installed, as seen in Figure 2.2a. Figure 1.3 also depicts the rings on some of the rods.

## 2.4 Transient introduced by switching

Switching transients are a well known phenomenon in electric power engineering. Switching transients are introduced to the system by a sudden change of the systems state. Thus, for example, closing a circuit breaker (CB) and connecting an uncharged capacitive load (e.g. long cable or capacitor bank) or opening a breaker and disconnecting an inductive load (e.g. rotating machinery) can introduce transients to the system [6], [7], [16]–[18].

As a simple and illustrative approach to the problem, the energisation of a LC load by an ideal voltage source can be considered: If the CB (in this case considered an ideal switch) is closed at maximum source voltage, a high current will rush into the capacitor, since its voltage has to be continuous. Shortly after the closing instant, the capacitor voltage matches the source voltage and the current would drop to zero. However, the current through the inductor has to be continuous and thus, the capacitor voltage overshoots the source voltage. The voltage will now oscillate with the circuit's resonant frequency and is damped by resistive elements. Similar to the energisation of the load, the breaker's opening can introduce a switching transient as well. This occurs, if the current through the inductor is suddenly interrupted, e.g. due to current chopping (CC) in the CB. The energy stored in the inductor must then be rapidly transferred to the other capacitive and resistive circuit elements, because the inductor's current has to be continuous. Thus, this also creates a oscillatory overvoltage (OV) at the circuits resonant frequency [16]–[18].

In real world applications, these switching OV are more complex than previously described as the CB and it's properties, the electric arc as well as the switching instant will influence the system's response. Especially the CB and its capability to prevent prestrikes, CC and restrikes of the electric arc in the breaking chamber is important. A prestrike occurs if, during the CB's closing operation, the insulation medium in the breaking chamber breaks down before the contacts are fully closed. Naturally, this occurs in case the CB is closed at a considerable instantaneous system voltage since then the voltage across the gap is high. As response, an oscillation as previously described will occur on the load side. Restrikes and

CC are a phenomena during the opening operation of a CB: Once the CB begins to open, an electric arc is drawn between its contacts. The arc current approaches zero towards the natural zero-crossing at power frequency and due to current limiting factors (arc resistance, arc length and cooling by the insulation medium). The arc is successfully extinguished if the plasma's temperature falls below a critical value (around 3000 K [7]), beyond which its resistance increases abruptly since thermal ionisation is no longer occurring.

After the initial arc extinction, the dielectric in the gap between the CB's contact's will begin to recover it's insulation strength. In the first few microseconds (4 - 8 $\mu s$ [17]) after current interruption, the insulation medium is in the thermal recovery stage. This stage is characterised by charged particles drifting between the contacts due to the rate of rise of the recovery voltage (RRRV). These drifting particles are also called 'post-arc current' and act as an energy input to the former arc channel. Only if the electric energy input of the RRRV is smaller than the capability of the dielectric to cool the post-arc region, the arc is successfully quenched. Otherwise the gap will thermally break down and the arc reignites, which is called 'restrike'. These restrikes can occur repeatedly in quick succession in the vicintity of the current's zero crossing.

After the thermal recovery phase, the insulation medium enters the dielectric recovery phase (more than 50 $\mu s$ after current interruption [17]). In this phase, the gap is stressed by the transient recovery voltage (TRV), which is dependent on the power system's characteristics. Only if the gap's dielectric strength is sufficient to sustain the TRV, the arc does not reignite. The TRV is generally defined by the energy stored in the capacitive and inductive circuit elements at the instant of current interruption.

CC is defined as the CB interrupting the current before the natural zero-crossing at power frequency (premature current interruption). This condition occurs especially for small inductive currents. In that case, the arc's low energy causes it to become unstable which leads to a high frequency (HF) transient current to flow in the CB's close electric vicinity. This HF current is superimposed on the power frequency current. This can cause a current zero crossing before the natural zero crossing at power frequency, if the power-frequency current has a small magnitude. During this premature current zero crossing, the arc extinguishes and the system is stressed by a considerably high TRV due to the energy stored in the inductive circuit elements. The high TRV can also lead to a dielectric reignition [6], [7], [17].

In the context of this project, closing one of the event switches leads to an inductive current through the coil, as the only current limiting factor is the coils impedance itself. Only considering the coil's reactance and a grid voltage of $62.5/\sqrt{3}\ kV$, the current would be approximately 57 $A$ at 50 $Hz$. According to internal information, the maximum current through the CB is approximately 2 $kA$, when only a section of the coil is used. Especially the value for the entire coil can be considered small compared to the CB's maximum short-circuit breaking current of 40 $kA$. The main technical information on the CB are presented in Table A.2. The CB's design incorporates features to prevent CC of small inductive currents. However, these features aim at breaking currents of approximately 20% to 30% of the maximum breaking current (40 $kA \cdot 0.2 = 8$ $kA$) as these are already considered 'small' by the manufacturer. Thus, the estimated current in the application at hand is still considerably lower. Therefore, the probability of CC is relevant as the CB might not be designed to break currents at this small magnitude without chopping. Further, the three-phase CB in this application is star connected. This implies the risk of 'virtual CC' [17], [18], during which the arc in one phase becomes instable due to the influence from transients introduced from one of the other phases.

### 2.4.1 400 V switching tests

In an attempt to assess the applicability of surge arresters (SA) to mitigate the transient voltage stress due to switching activity, a low voltage switching test with a wide band measurement of the voltage response was performed by R&D Test Systems A/S. The measurement campaign also incorporates tests with LV varistors to emulate the impact of SA in the setup. It has to be mentioned here that this measurement campaign is not able to represent the effects of CC accurately. Since CC is largely dependent on the magnitude of the interrupted current, which influences the arc's thermal energy, a low voltage measurement is not accurate. The reason is that for the same coil impedance, the current's magnitude will be much smaller at 400 V compared to rated voltage. Still, the measurement results are presented in the following, as they yield some relevant information on the coil's electric properties.

The tap configuration during the LV switching tests is shown in Table 2.2. The connection of the grid is replaced by a 400V plug from the auxiliary voltage supply and the CB for the DUT is open. The tap configuration is also visualised in Figure 1.1.

| Description | Tap position |
|---|---|
| Grid | Tap 19 (70 %) |
| DUT | Tap 11 (35 %) |
| Event switch 1 | Tap 7 (15 %) |
| Event switch 2 | Tap 11 (35 %) |

**Table 2.2:** Tap configuration 400V switching test. Value in parentheses indicates number of turns used.

The voltage was recorded between the grid connection and event switch 1, in parallel with utilised section of the reactor. The response recorded is presented in Figure 2.3. The Figure shows a transient distortion of the voltage, when the coil is

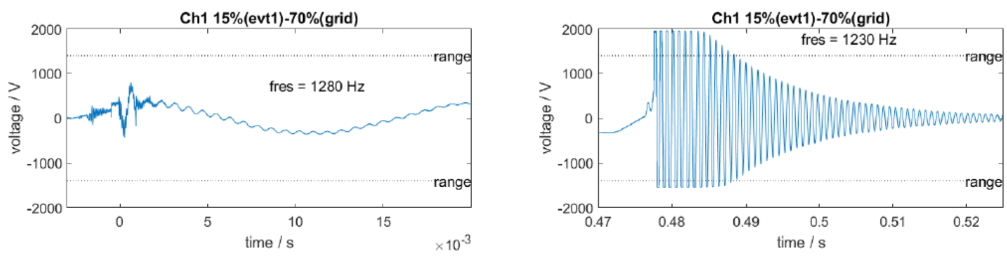


**Figure 2.3:** Transient response of 400V switching test, operating event switch 1

energised (event switch closing, left graph). The transient mainly consists of one cycle with a magnitude of approximately 1 p.u. at a frequency around 1300 Hz. Afterwards, the sinusoidal grid voltage is distorted by a component at the same frequency, but smaller magnitude.

The opening operation (right graph) of the event switch, however, introduces a transient of very large magnitude into the coil. The resonant frequency of this oscillation is given with 1230 Hz and shows a magnitude well above the probe's input range. The time constant of the envelope's decay can be estimated using the data. It was found $\tau \approx 0.0122s$. Using this information and the magnitude of the envelope at an arbitrary point in time ($U_1$, $t_1$), the maximum amplitude at the switching instant $t_0$ can be estimated:

$$U_0 = \frac{U_1}{e^{(t_1-t_0)/\tau}} \approx 3.05\ kV \tag{2.1}$$

Recalling the input voltage was $400V \cdot \sqrt{2/3}$, this value is exceeded the rated voltage by a factor of nine for a short period of time. Higher frequency oscillations are not considered in this approximation. The magnitude of oscillation indicates a very large current gradient in the CB, leading to a large OV in the coil. Recalling the previously described current breaking mechanism, CC is likely to occur in this case: The CB deployed as event switches are designed to break currents in the range of multiple Kiloampères, while in this case the current is small due to the source's low voltage and power. Thus, it is likely that the arc was extinguished before the natural current zero-crossing. As previously mentioned, currents in the range of 8...12 $kA$ are already considered 'small' by the CB's manufacturer as the maximum rated breaking current of the CB model deployed is 40 $kA$.

### 2.4.2 Sweep frequency response analysis

To further analyse the coil's behaviour, a sweep frequency response analysis (SFRA) was also conducted by R&D Test Systems A/S prior to this project. The frequency generator was connected in different tap positions and the impedance and phase angle observed. The measured response for the impedance between taps 7 and 19, as during the switching tests, is presented in Figure 2.4.

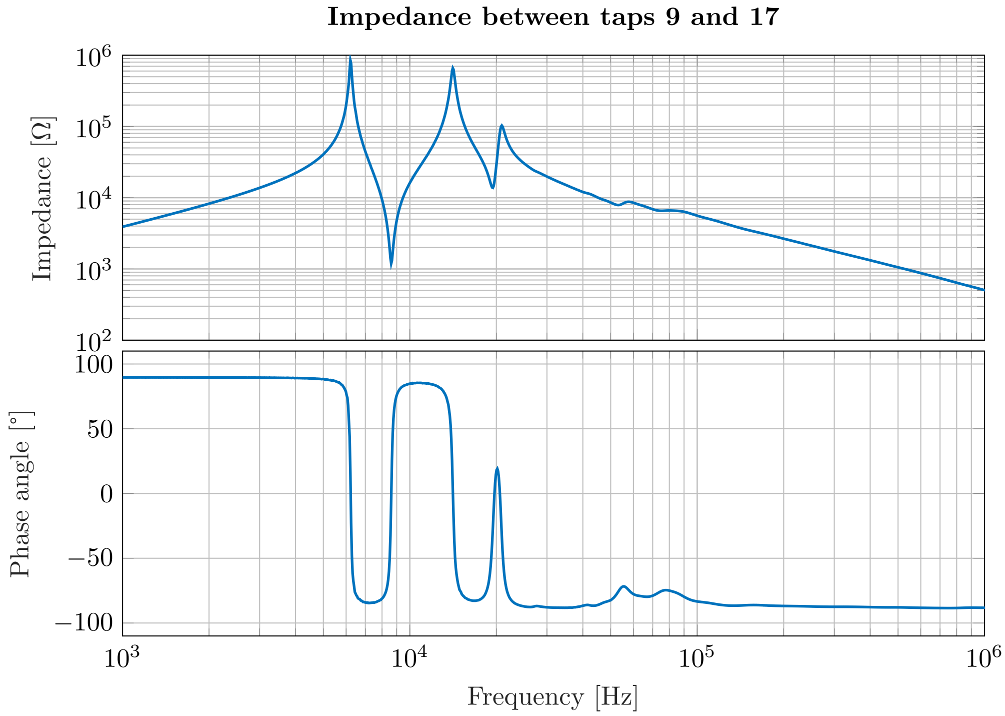


**Figure 2.4:** Frequency response between taps 7 and 19

The response shows an inductive behaviour initially, where the amplitude rises with frequency and the phase angle is around 90°. The first resonant frequency occurs slightly above 6 kHz. After a few series and parallel resonances, the coil shows capacitive behaviour, indicated by a decreasing amplitude and a phase angle of -90°. The explanation is the coil's significant internal capacitance: As the winding consists of aluminum foil with only a thin insulation between the turns, the turn to turn capacitance will be considerably high.

### 2.4.3 Comparison of SFRA and switching tests

The previous sections on the measurement results in the 400V switching campaign and the SFRA show a misfit in response: The expectation that the switching activity creates an oscillation inside the coil at its resonance frequency is not met. The expected oscillation frequency in Figure 2.3 is in the range of 6 kHz to 6.5 kHz, since it is the first resonance observed in Figure 2.4. The cause of this misfit is uncertain, but some hypothesis can be formulated:

- The oscillation of 1230 Hz observed in Figure 2.4 could be influenced by components in the 400V grid or on the HV side of the step-down transformer.

Due to its large transformation ratio (33 kV to 400 V), even a small capacity on the HV side is "amplified" and can significantly impact the LV grid.

- The SFRA was performed on the isolated coils, without any connection to the other components in the FRT Tester. Thus, a similar effect as mentioned before can be ruled out.
- The two measurements were performed a approximately two months apart, during which some more discharges were recorded. Thus, it is imaginable that during this time the coil's electric properties changed. However, a significant change in the coil's properties was not observed during operation of the FRT tester.

The model developed in Chapter 3.4 is based on the analytic calculation on the coil's parameters and shows a SFRA response closely following the measurement result in Figure 2.4.

## 2.5 Internal resonances in transformer windings

In 1975, four failure incidents of auto-transformers in the American power system were attributed to inter-winding resonance (or part-winding resonances (PWR)) phenomena, triggered by transient OV [19], [20]. As a consequence, this phenomenon was studied in more detail and still motivates research to deeply understand the topic [21]–[24] and to optimise the winding design in HV transformer windings, alleviating the stress on the insulation system [25], [26]. Often this phenomenon is associated to very-fast transient overvoltages (VFTO) of oscillatory nature, which might occur due to the presence of CC and restrikes in $SF_6$ insulated switchgear. Martinez-Velasco in [17] also mentions switching transients as a cause for PWR.

Inter-winding or part-winding resonances must not be confused with terminal transformer resonance. The latter is a phenomenon, where the natural frequency of the entire transformer is excited as part of the HV circuit and a resonance can be measured at the transformers terminals. Compared to this, in PWR each turn has to be considered as an individual LC-circuit with its own resonance frequency. If the oscillatory transient OV's frequency coincides with the natural frequency of some of the winding's sections, PWR can develop and the internal voltage exceed the initial voltage magnitude. This phenomenon is not always visible at the transformers terminals, but often requires measurements inside the winding.

S. De, A. De and Bandyopadhyay point out in [25] that in HV transformers with disc type winding the capacitance in the winding is often deliberately increased to achieve a linear voltage distribution inside the winding (between the individual discs). However, this poses the risk of PWR as the high capacitance reduces the resonance frequency inside the winding, bringing it close to the transients occurring in the power system.

The coil at hand can be considered as a large, single disc of a disc-type transformer winding with considerable series-capacitance (turn to turn capacitance) and small ground capacitance. Due to the high series capacitance this setup might be prone to PWR as discussed in [25], [26]. Because the OV is only developing internally due to resonances, surge arrestors at the transformer's (coil's) terminals only have limited effectiveness. An alternative approach discussed in [24] is to filter critical frequencies to prevent the excitation of PWR.

## 2.6 Conclusion

Recalling the low dielectric stress in quasi-stationary analysis as well as the significant OV during the switching tests, OV due to switching activity and transients propagating through the coil are probable to cause the discharges. The CB and its high rated breaking current compared to the small inductive currents during the FRT Tester's operation likely lead to CC. Potentially this also excites the coil's internal resonances. The pollution due to sea salt and humidity further amplifies the probability of discharges, but is most likely not the root cause. As already indicated by the coil manufacturer's measurements (Figure 2.1), there is a non-linear voltage distribution along the turns of the reactor. For higher frequencies and the transient response, this non-linearity will probably increase as the coil's parasitic capacities then define then the voltage distribution. Additionally, the observation of discharges in timely correlation with the switching further supports these hypothesises. The transient voltages introduced by switching could also give rise to internal resonances, stressing the insulation in specific spots.

The following Chapter 3 proposes a detailed model in the frequency domain. This model is simplified to be assessed in the time domain. The origin of discharges and the stress on the insulation is thereby analysed in more detail. The simulation results and auxiliary components used in the time domain are presented in Chapter 4.

# Chapter 3

# Computer model of the air-core reactor

*In this chapter, the modelling approach for the coil is discussed and presented. Initially, an analytic frequency domain model based on an equivalent circuit with one section per turn is developed and analysed. Afterwards, this model is simplified to meet constraints regarding computational power for the time domain simulation (see Chapter 4). The simplified (lumped) model is again analysed in the frequency domain to justify its accuracy.*

## 3.1 Coil's construction and insulation system

The reactor's construction was briefly introduced in Chapter 1.2, also presenting a picture of the coil in Figure 1.2. To emphasize important aspects of the coil's construction and insulation system, the sketch in Figure 3.1 highlights some detail in the coil's construction. As visible in the sketch, the coil consists of aluminum foil and insulation material, which is rolled onto a spindle. For the sake of simplification in the simulation, the resulting spiral is reduced to concentric rings of Aluminium and insulation. To prevent unintentional connections between turns, the insulation material is overhanging the aluminum conductor by a few centimeters. As evident in the sketch, the innermost turn of the coil is labelled as turn 1 while the outermost turn, with the largest radius, is referred to as turn n.

Every few turns, the winding is separated into packs by cooling ducts. These cooling ducts are mainly filled with environmental air, but also with spacers (GFRP bars) in axial direction for mechanical purposes. The spacers are connected by radial rods of the same material. Due to the manufacturing process, a layer of aluminum foil is directly exposed to the cooling duct, as visible in the sketch. On the cooling duct's opposite side, the conductor is fully covered by a layer of insulation material.

The axial spacers for the cooling ducts and radial rods are not considered in the electrical simulations presented in the following sections of this chapter. However, their impact can be of importance for surface discharges, as these two components create a creeping path, shunting several of the coil's turns.

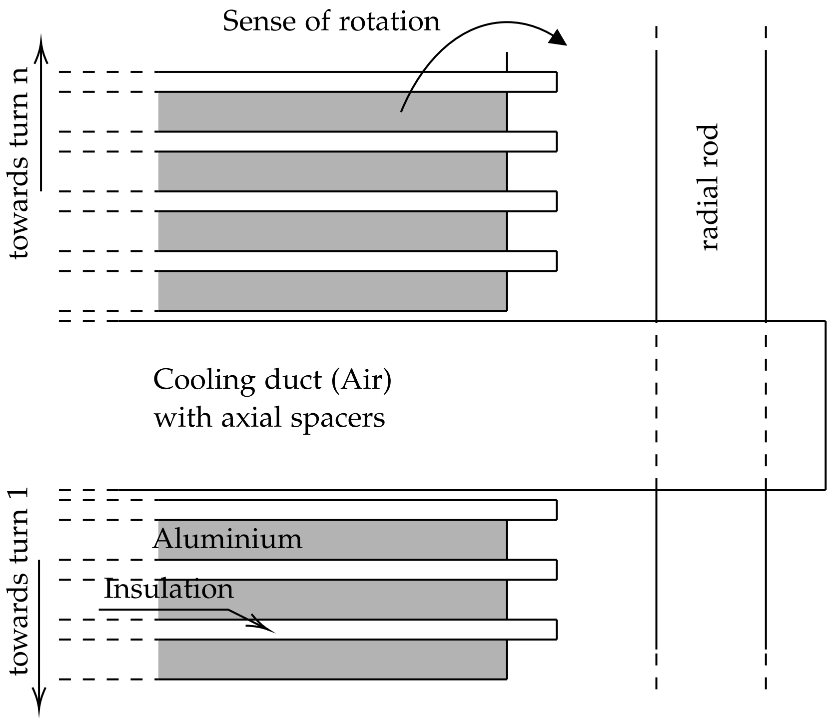


**Figure 3.1:** Sketch of coil's insulation system

## 3.2 Discussion on modelling approach

There are various different approaches to create an electric model of the coils used in the FRT tester. To select the most appropriate one, the desired knowledge gain as well as the drawbacks and limitations of the modelling approaches have to be considered. To achieve a comprehensive result, the reactor's model must ultimately describe the dielectric stress on the insulation dependent on the physical location in the coil as a response to the FRT Test procedure. This allows to propose effective counter-measures (Chapter 5) to prevent discharges in the future. The accuracy of the simulation is naturally limited as simplifications are always necessary or estimations of some influencing factors (e.g. pollution) have to be taken due to randomness or lack of comprehensive data. Thus, counter-measures proposed through the simulation often need to be assessed experimentally.

### 3.2.1 General considerations

As discussed in Chapter 2, the discharges observed are closely correlated to the operation of the event switch. Consequently, the dielectric stress on the insulation must also depend on the switching operation. Thus, a model in the time domain, in which switching can be simulated is projected to be most accurate. Using Fourier transformation and other mathematical operations, the applied stress may also be decomposed into a sinusoidal excitation of the model with various frequencies [27], transforming the model into the frequency domain. This generally simplifies the model and facilitates the computation in some software. But for a non-ideal step input, the amplitude of the sinusoidal components will decrease with increasing frequency. Thus, low resonance frequencies are usually most dangerous for the insulation as the switching impulse can excite these resonances with considerable magnitude. This circumstance has to be considered when analysing a model in the frequency domain.

Independent of the model's domain it is imperative that the coils construction and physical parameters are considered in sufficient detail. It is foreseeable that for example the capacity between the coil's turns has a significant influence on the response. This fact also shows in the frequency response presented in Chapter 2 in Figure 2.4. The response shows the coil section's capacitive behaviour for frequencies beyond 20 kHz. Different approaches to determine the coil's electric parameters and parasitic components will be discussed. A sufficient resolution of the reactor's physical structure is further necessary to gain information on highly stressed regions of the insulation, thus allowing the proposal of adequate countermeasures.

### 3.2.2 Different modelling approaches

Generally there are a two fundamentally different methods to simulate an electric apparatus: analytical and numerical models.

Throughout the last decades, numerical methods have gained increasing attention as the computational power grew and efficient solving algorithms were developed. These methods are often used when a analytic description of the apparatus is infeasible, due to a complex structure, for example. Some prominent numerical methods are the boundary element method (BEM), finite difference method (FDM) or finite element method (FEM). All of these methods rely on discretizing either the surface of the structure (BEM) or the entire volume (FDM and FEM) into small elements. In these elements, a linear or quadratic approximation of the electric field is considered valid, as their dimensions are small. Thus, the accuracy of the simulation increases with the number of elements. The linear or quadratic expressions can then be solved relatively easily, considering information of adjacent elements as boundary conditions. Other numerical methods are for example integral equation methods, using the superposition of charges to compute the electric field, of which the charge simulation method (CSM) is one example. While the CSM eases the computation of space charges and their electric fields, the consideration of different materials is less efficient. FEM and similar methods facilitate the consideration of different insulation materials, thus posing a fitting approach in the problem at hand [6], [7].

The numerical methods permit the computation of the (parasitic) electrical parameters of a complex physical structure. In the case of the air-core coils in this project, a detailed numerical model would deliver the coil's inductance, capacitance and resistance with respect to its construction by computing the electric and magnetic field in the coil. Thus allowing further analysis of the model by the means of frequency domain and possibly and time domain. Some FEM softwares also offer the possibility to analyse the model in frequency domain (e.g. by the means of a frequency sweep analysis) directly in the same tool.

The analytical methods applicable in the given project can be subdivided into lumped parameter equivalent circuit models and distributed parameter models based on telegraph's equations. The latter approach has some relevance for modelling transformer windings stressed with VTFO [24], [28], [29]. These distributed parameter models are similar to a multi-conductor transmission line model with distributed parameters and allow the accurate description of the voltage distribution in the coil for frequencies beyond 1 MHz [29]. The coil in this project is similar to a single disc of a disc-type winding in a power transformer. Often, equivalent circuit models lump the electrical parameters each disc together, in order to describe the voltage distribution between the discs of a power transformer [19]. Naturally, this would not lead to a satisfactory result in the problem at hand, if all electric parameters of the coil are lumped into a single section. Instead a equivalent circuit with a lumped section for each turn would be required for a reasonable resolution. Lumped parameter models of transformers are considered accurate for frequencies up to 1 MHz [29].

### 3.2.3 Conclusion

In the context of this project, the large physical size of the coil, the high amount of turns and the small distance between the individual turns (insulation thickness is less than a millimeter) would lead to a very high amount of elements, if a numerical modelling approach was chosen. However, it is possible to simplify the model (see section 3.3) and thereby reduce the complexity. It is important to realise that in this case valuable information on for example the capacitance, might be lost. Thus a simplified FEM model might not be suitable for frequencies beyond power frequency, but can act as validation for another model at the given frequency.

The analytical models are more compelling in the context of this project. The reason is the relatively simple geometry: The coil can be simplified into 1260 concentric rings, representing the individual turns, allowing the analytical calculation of the model's parameters. The effects of this simplification will be discussed in more detail in the following section 3.4. Furthermore, a lumped parameter equivalent circuit is less complicated than a model based on multi-conductor transmission line. As shown in Figure 2.4, the frequency range of interest is most likely well below 1 MHz as the first resonances appear around 7 kHz. Thus, a lumped parameter equivalent circuit is considered sufficient.

## 3.3 Simplified finite element model

A simplified FEM[1] model developed by R&D Test Systems A/S lumps the sections between the 29 taps of the coil together into 28 circuits. These circuits are arranged in a 2D rotary symmetric model, using the geometric parameters of the coil. Each circuit contains the number of turns between the adjacent taps. The 28 turn circuits are considered as concentric rings, containing the number of turns and thereby significantly simplifying the winding structure. This simplification allows to solve the FEM model quickly, but contradicts gaining detailed information on the capacitance between the turns of the coil. Therefore, this simplified FEM model may only be considered valid at low frequencies (i.e. up to the first resonance point). The self- and mutual inductance of the 28 circuits are considered as well as the resistance of the winding, which can be calculated analytically.

Calculated using this FEM model, the power frequency impedance is within 5% range of the rated values given in the data sheet in table A.1.

Due to the simplification of the FEM model, the voltage and E-Field distribution depending on the location in the coil can only be analysed coarsely, for the different tap positions. This is considered insufficient for a detailed analysis and further not of great interest as the results would only be valid for low frequencies.

## 3.4 Analytic frequency domain model

### 3.4.1 Introduction and equivalent circuit

As discussed previously in Section 3.2, an analytic lumped parameter model is projected to sufficiently represent the coil for the frequency range of interest. The model developed by R&D Test Systems A/S is based on the equivalent circuit presented in Figure 3.2, consisting of $n = 1260$ sections, i.e. one for each turn of the coil.

[1]The model is developed in the FEMM [30] toolbox for Matlab and Octave.

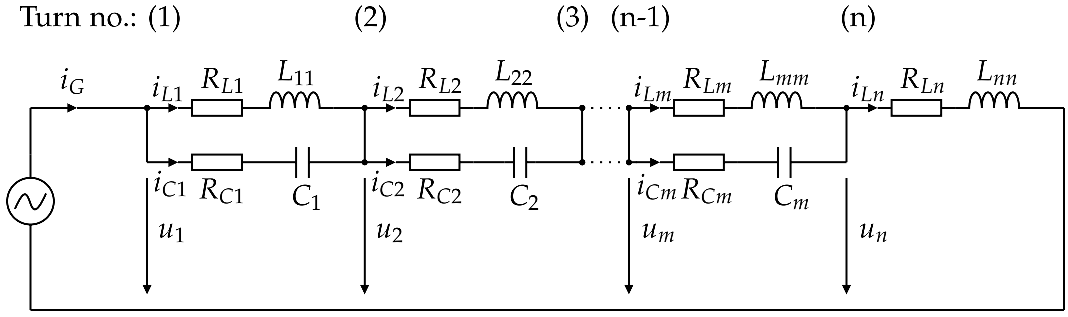


**Figure 3.2:** Equivalent circuit for analytic model

The equivalent circuits consists of one node for the beginning of each turn and frequency-invariant components to express the electrical behaviour. The voltages $u_1$ ... $u_n$ express the voltage drop from the beginning of each turn to the end of the coil's last turn. The inductors $L_{11}$ ... $L_{nn}$ are representing the self inductance and mutual inductance of each turn with all other turns. The resistors $R_{L1}$ ... $R_{Ln}$ and $R_{C1}$ ... $R_{Cm}$ are based on the finite conductivity of the winding material and the insulation, respectively. The capacitors $C_1$ ... $C_m$ contain the capacitance between adjacent turns of the coil. The capacitance to ground and to turns other than the adjacent ones is not considered. Thereby, the complexity of the model is reduced, assuming that the capacity between adjacent turns is much larger than other stray capacitances in the coil. Considering the construction of the coil out of thin aluminum foil and dielectric foil between the turns, this assumption is reasonable.

The series resistance of the insulation $R_C$ is assumed as zero, i.e. the active power losses in the insulation are disregarded. Thereby the model is further simplified, without imposing it's accuracy. This is based on assuming that the active power loss in the conductor dominates the active power loss in the insulation due to the significant rated current and short circuit current (see Table A.1).

### 3.4.2 Analytic parameter calculation

#### Inductance calculation

The inductance of each turn is analytically calculated using Grover's tables for concentric ring coils [31]. Grover considers the geometric parameters of the concentric coils and provides look-up tables to find the mutual inductance. A detailed description of Grover's method as well as the tables used for the calculation can be found in the Appendix B. The concentric turns of the coil at hand have an equal length and are aligned with each other, i.e. are not laterally displaced. The data in the tables presented in Appendix B was interpolated to find the values for an arbitrary pair of turns.

Generally, Grover's method is widely accepted and considered accurate [32], [33], although the error claimed by Grover of $10^{-4}...10^{-5}$ is not met in all geometric configurations. According to [32], the error of Grover's method is small for significant differences of the coils radii ($\alpha < 0.6$) and equal lengths of the coils, or when the coils are not laterally displaced ($s = 0$) and have equal length. In reality, due to tolerances in the manufacturing process, the rings will be laterally displaced. An indication for the overall error can be found by comparing the coil's rated inductance to the simulated value. The error is less than 5%.

**Resistance calculation**

The resistance $R_{Ln}$ of a single turn is described by the simple formula (3.1), in which $r_n$ is the turn's radius, $\rho = 2.44 \cdot 10^{-8}\ \Omega m$ is the resistivity of aluminium at $0°C$ and $A$ is the cross section area of the conductor, i.e. the foil's width multiplied with the thickness. Further, $a = 0.0039\ K^{-1}$ is the temperature coefficient of aluminium.

$$R_{Ln} = \frac{2\pi \cdot r_n \cdot \rho \cdot (1 + a \cdot 20°K)}{A} \tag{3.1}$$

Furthermore, it has to be assessed, whether the skin and proximity effect will have a significant influence on the resistance of the conductor at hand. These effects may be disregarded if the current sufficiently penetrates the conductor in frequency range of interest (i.e. the first resonances in Figure 2.4.2), leading to only a minor change in resistance value. The high frequency skin depth (depth of penetration) $\delta$ in the aluminium conductor at hand can be calculated, according to [34], [35]:

$$\delta = \frac{1}{\sqrt{\pi f \mu \sigma}} \tag{3.2}$$

In equation 3.2, $\mu$ and $\sigma$ are the conductor's magnetic permeability and conductivity respectively. According to Hayt in [34], the resistance of a rectangular conductor with width $b$, length $L$ and infinite thickness at frequency $f$ and considering the skin effect is equal to the resistance of the same conductor but with thickness $\delta$ and not considering the skin effect.

$$R(f) = \frac{L}{\sigma\delta(f) \cdot b} \tag{3.3}$$

Using formula (3.1), the DC resistance of the conductor can be compared with its frequency dependent equivalent, Equation (3.3). The relation is plotted in Figure 3.3. For instances where the skin depth is larger than the aluminum foils thickness (at frequencies up to 30 kHz), the ratio is equal to 1. The graph clearly shows that for the frequency range of interest (up to some tens of kilohertz), the skin effect will only have a minor influence. At a frequency of 100 kHz, the aluminium foil's resistance would only increase by a factor of 1.8. Consequently, the skin effect can be disregarded in the problem at hand.

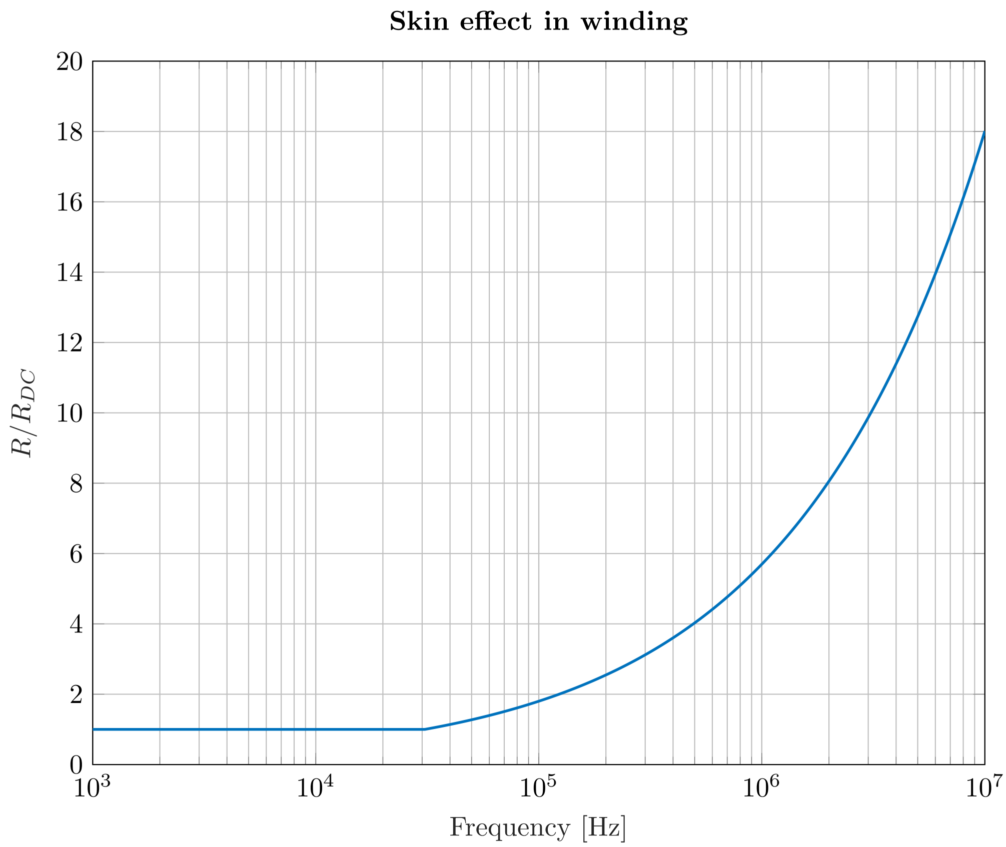


**Figure 3.3:** Skin effect: resistance as function of frequency

In the coil at hand, the current in adjacent turns will have the same orientation. Thus, the magnetic field strength between the conductors will be decreased, while it is increased outside of two adjacent conductors. In [36], this is referred to as the 'anti-proximity' effect, while two conductors carrying current in opposite direction are subject to the proximity effect. According to [36], the anti-proximity effect does only play a significant role for rectangular conductors, if the skin depth is smaller than the conductors thickness ($t_{Alu}/\delta > 1$). Consequently, it is disregarded in the context of this project, as the frequencies where this effect has a significant influence are beyond the scope of interest.

### Capacitance calculation

The capacitance $C_m$ between two turns can also be computed analytically by the means of a simple expression (3.4). In this expression $\epsilon_0 = 8.8542 \cdot 10^{-12}$ is the permittivity of vacuum and $\epsilon_r = 2.3$ the relative permittivity of the insulation material. The latter value was found by iteration to archive minimum error between the measured and simulated SFRA response, as seen in Figure 3.4. Further, $r_n$ and $r_{n+1}$ describe the radii of the two adjacent turns, respectively. The aluminum foil's thickness $t_{Alu}$ and the coil's length $l$ (which is the same as the aluminum foil's width) are required geometric parameters to calculate the capacitance:

$$C_m = \frac{2\pi \cdot \epsilon_0 \epsilon_r \cdot l}{log(r_{n+1}/(r_n + t_{Alu}))} \tag{3.4}$$

### 3.4.3 Model validation in frequency domain

The model is solved by defining an arbitrary current as input from the grid, which is the node source current of the first turn in the model. Then, by the means of Kirchhoff's laws, the currents in the branches $i_L$ and $i_C$ of the equivalent circuit and the node voltages $u_n$ can be computed, using the admittance matrix. The impedance of the coil as seen from the grid is then the node voltage $u_1$ divided by the initial input current. To achieve comparable results, this value was normalised to the rated voltage of the grid $66/\sqrt{3}\ kV$, which is considered as $1p.u.$.

The simulated total resistance and reactance of the coil at 50 Hz are within an error margin of 5% of the rated values presented in table A.1 and are within 0.1% deviation range to the values obtained through FEM (Section 3.3).

The coil's manufacturer provided measurements of the voltage distribution at power frequency. Figure 3.5 displays the measured data points as well as the node voltages calculated in dependency of the number of turns (i.e. the number of nodes in Figure 3.2) for the detailed and the lumped model developed in the following Section of this report. As evident from the figure, the voltage distribution is very similar to the measurements carried out by the manufacturer. It is further visible that even at power frequency, there is a non-linear voltage distribution on the coil. In regions where the graph shows a steep gradient, the insulation system is stressed more, because the potential difference between turns is larger.

To further justify the chosen modelling approach, the models frequency response can be compared to the measured SFRA, as presented in Figure 3.4. As opposed to Figure 2.4, now the entire coil is considered and not only a section of it.

The comparison of the simulated and measured SFRA shows that the model is accurately representing the measurement data. For the first resonance at approximately 7 kHz, the amplitude of the impedance is similar. For higher frequencies, the amplitude differs increasingly, with the model's amplitude being too high. Most likely, this is due to the resistance's frequency dependency, which was not considered in the model. For frequencies beyond 20 kHz, the model shows resonances, which are not visible in the measurement due to damping. Thus, effects

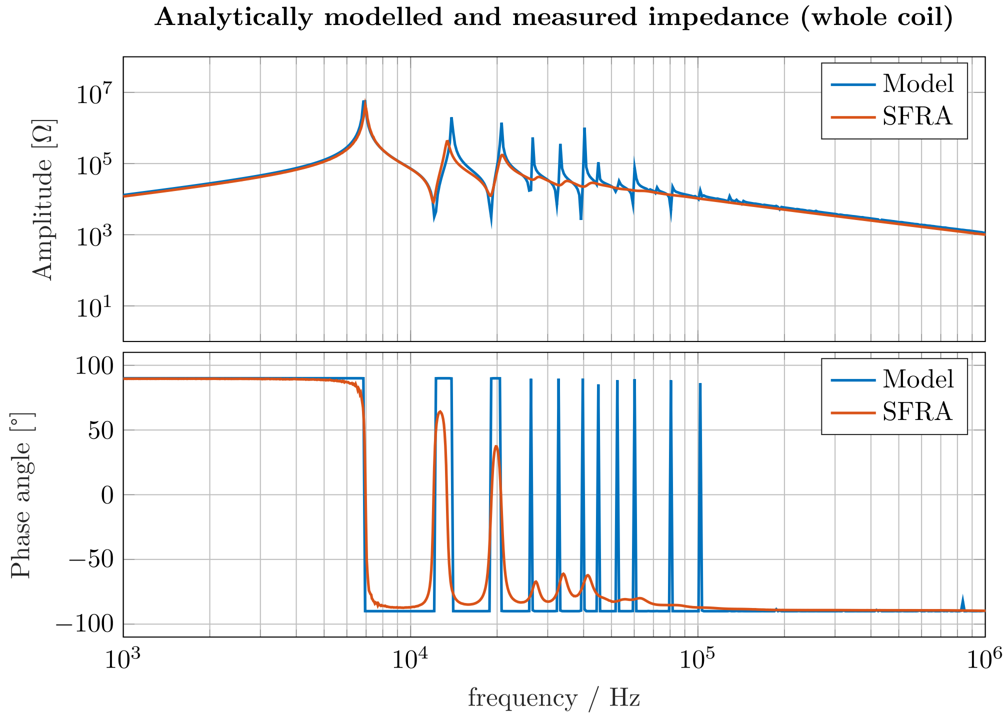


**Figure 3.4:** Simulated and measured SFRA

observed beyond this frequency can be disregarded to some extend.

### 3.4.4 Summary

The model developed in this section is based on the analytical calculation of the coil's parameters. The components are then assembled in an equivalent circuit with one section for each of the coil's turns. Since the coil's geometry is the basis for the parameter calculation, the voltage distribution along the turns, $u_n$, can be used to assess the voltage distribution as a function of location in the coil. The comparison of the model's impedance in the frequency domain with measurement data is a strong basis for confidence in the model. The model and the measurement show especially good agreement in the first resonance point, which is most important because it usually corresponds to the lowest damping due to it's low frequency.

## 3.5 Lumped, analytical model for time domain simulation

In Chapter 2, transients introduced by switching operation and chopping of the inductive current through the coil when reopening the event switch were identified as the root-cause for the discharges observed at the reactor. Thus, it is desirable to analyse the model in time domain as this domain offers the possibility to assess the coil's response to switching activity. Further, it is also beneficial to assess counter measures in the time domain model.

As the software tool, PLECS Standalone [2] is chosen. This software offers convenient time-domain simulation with useful features, for example directly analysing simulation results in MatLab. PLECS considers all components to be ideal, which drastically reduces the computer systems requirements and increases simulation speed compared to other software tools. Since the coil's parasitic components are already expressed in the equivalent circuit or may be disregarded as previously discussed, PLECS' approach does not contradict the result's accuracy.

Due to computational limitations, it is necessary to simplify the coil's model, as presented in the following section. As shown, this model still gives accurate results in the frequency domain.

### 3.5.1 Discussion and lumped section approach

The core of the model in time domain will be an equivalent circuit similar to the one presented in Figure 3.2. However, it is necessary to further simplify the model as the time-domain simulation is more resource-demanding. The most prominent approach is to lump multiple turns together and thereby reduce the number of sections in the equivalent circuit. When simplifying the model, the desired simulation result has to be considered. Thus, the lumping scheme still must be sufficiently detailed to offer conclusions regarding the voltage distribution inside the coil, as a function of location. A model with 28 lumped sections, as used in the FEM simulation (Section 3.3) is not considered sufficient due to the previously mentioned constraint.

Without major loss of detail, the model can be reduced to 126 lumped turns, consisting of $k = 10$ of the original model's turns each. During the development of the time-domain model, it was found that the inductance matrix resulting from this lumping scheme has a determinant numerically very close to zero. Thus the PLECS solver is not able to solve the circuit matrix, resulting in an error. Consequently, a non-symmetrical lumping approach was chosen: In the coil's outer and inner segment (see Section 1.2) each $k = 20$ turns are merged together. In the middle segment, in which most of the discharges were reported, only $k = 10$ turns are lumped. Thus, resulting in a model with 81 lumped sections.

The lumped turn's radius is the mean value of the individual turns' radii. Caution has to be paid that none of the lumped turns lays within one of the cooling ducts, i.e. only turns within one pack are merged together. This is important because the cooling ducts are representing a distortion in the coil's winding scheme. Thus, it is imaginable, that the sudden change in capacitance and inductance leads

[2] https://www.plexim.com/, last accessed 02.05.2022

to the reflection and refraction of a travelling wave in the coil. As this effect might effect the voltage distribution in the coil and thereby the discharge mechanism, it still has to be represented in the simplified coil model.

The parameters for this lumped model's equivalent circuit are again calculated analytically, using the same approach presented in section 3.4.2. For each of the circuit components, the number of lumped turns $k$ has to be considered:

- The resistance increases by factor $k$, as the conductor's length is proportional to the resistance.
- The aluminum foil's thickness $t_{Alu}$ is considered $k$-times, when calculating the capacitance.
- When calculating the inductance matrix using Grover's method presented in Appendix B, $k$ is the number of turns of each concentric single layer coil.

### 3.5.2 Model validation

The lumped model can be validated to some extend by analysing it in the frequency domain. As a first step, the voltage distribution at power frequency can be compared to the manufacturer's measurement, Figure 3.5. As evident from the graph, the simulated voltage distribution is in good agreement with the detailed model and the measurements. Also the SFRA and detailed model are accurately represented by the lumped model for frequencies below 100 kHz, as shown in Figure 3.6. From this Figure, it is evident that the largest deviation between the lumped and detailed model in the frequency range of interest occurs at the first anti-resonance at approximately 12 kHz. While the detailed model is resembling the measurement data quite accurately, there is a larger deviation to the lumped model. The resonance in the lumped model occurs at 12.5 kHz, which is 500 Hz higher than the measurement data. The reason is most likely the lumping scheme and the slightly altered turn arrangement: Because the lumped turns may only represent turns within one pack, the number of turns in the pack has to be a multiple of $k$. Thus the geometry was slightly altered because a few packs consisted of 89 or 101 turns respectively. While this necessary adjustment only has little influence on the inductance, it does apparently have a larger influence on the capacitance, leading to the altered response in frequency ranges, where the capacitance is dominating.

From theory regarding the modelling of cables using a number of equivalent circuit sections (e.g. $\pi$ sections), it is clear that the coil's measured frequency spectrum can only be represented by the model, if the number of equivalent circuit sections is sufficiently high [16]. Furthermore, as discussed previously, a relatively large number of sections is required to allow for the assessment of voltage distribution as a function of location in the coil. The previously presented figures

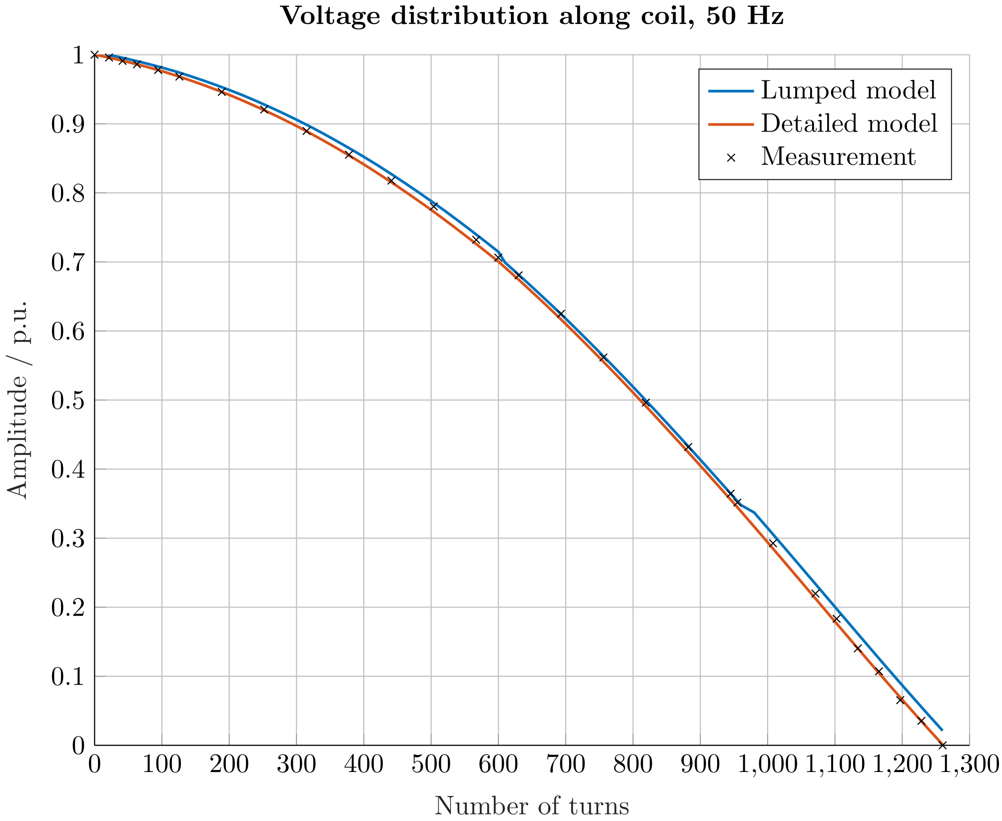


**Figure 3.5:** Spatial voltage distribution of lumped and detailed model compared with measurement, 50 Hz

show that the lumped section model is still sufficiently detailed to show the coil's resonance characteristic.

It would be very desirable to justify the model by recreating the switching response observed in Figure 2.3. However, there is a misfit between measured switching response and measured SFRA, as outlined in Section 2.4.2. Furthermore, during the switching test, the voltage probe reached it's limits. Thus, the actual measured magnitude of the OV remains unknown and can consequently not be used as a factor for validation of the simulation. The oscillating frequency of the measured switching response does not correspond to the SFRA. Some possible explanations for this circumstance were pointed out in Section 2.4.2. All in all, these circumstances of the switching response measurement contradict its use for validating the time-domain simulation.

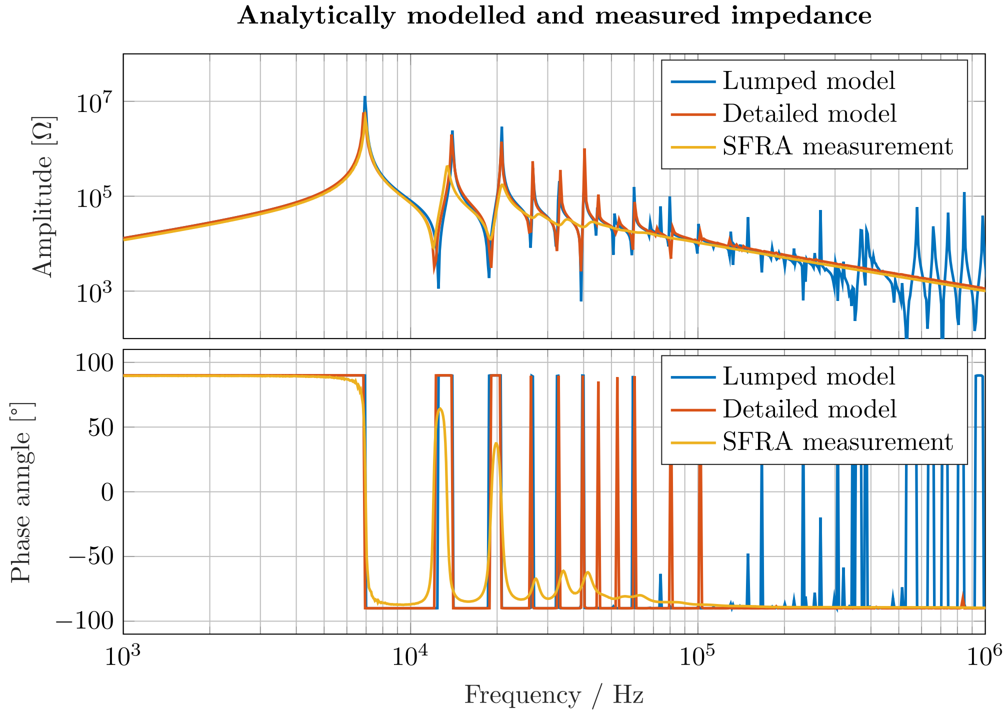


**Figure 3.6:** Impedance characteristic of detailed and lumped model compared to SFRA measurement

## 3.6 Summary

This Chapter comprehensively discussed different modelling approaches and introduced an analytical approach to obtain the coil's electrical parameters in a detailed turn to turn resolution. These parameters are then assembled into an equivalent circuit with one section for each turn. The comparison of this detailed model with measurement data in the frequency domain indicates an accurate representation of the real coil by the model.

To allow the analysis of switching events, the model is ported to the time-domain. While the equivalent circuit's scheme remains unchanged, it is necessary to simplify the model by lumping turns together. Before the results obtained in time domain are presented in the following Chapter 4, the lumped model is also analysed in the frequency domain. While the deviation between lumped model and measurements is larger, the inaccuracy is still tolerable.

# Chapter 4

# Simulation results of coil model in time domain

*This Chapter initially introduces some auxiliary components in the time domain model. Afterwards, the model's settings, such as solver settings, but also the coil's tap configuration are presented. Further, simulation results obtained in the time domain are displayed and comprehensively discussed.*

## 4.1 Models for grid, circuit breaker and device under test

### 4.1.1 Device under test

The device under test (DUT, i.e. the wind turbine) will be excluded and not considered in the simulation. The reason is that considering the DUT would increase the simulation's complexity drastically while not influencing the result significantly: When the event switch is open, before the fault scenario is emulated, the DUT would deliver a certain current through the coil and into the grid, as the coil only acts as an impedance between grid and DUT. Once the event switch closes, the coil draws a high inductive current from the grid, only limited by its impedance. This current's magnitude will exceed the DUT's load current significantly. As discussed in Chapter 2, the highest voltage stress is most likely occurring resulting from a switching OV once the Circuit Breaker (CB) is opened. Consequently, the DUT's current will only have a minor influence on the discharges observed at the coil. This hypothesis is further supported by the fact that the first three discharge incidents (see Section 2.1) were reported during commissioning, when no DUT was connected.

### 4.1.2 Circuit breaker model

It is foreseeable that the CB and its model will have a significant influence on the observed switching response. The reason is that the CB will dictate the magnitude of CC, which greatly influences the switching OV (see Section 2.4). CB models used in Literature often require comprehensive and detailed data on the breaker and the arc's properties (Models by Cassie-Mayr and modified by Schwarz-Avdonin) [17]. However, in case the chopping current $i_c$ can be reasonably estimated, a simplified model using an ideal switch can be used instead [37], [38].

In the context of this simulation, the CB is modelled as a an ideal switch. The switch's operating logic is current dependent: Once the current falls below the value of $i_c$, the switch opens, chopping the current. Due to limited measurement data available, the value of $i_c$ can only be estimated. In [37], [38], equation (4.1) is suggested to estimate the current value based on the capacitance $C$ in the circuit and the chopping constant $k$. $N$ is the number of breaking chambers in the CB, which is 1 for the CB deployed.

$$i_c = k \cdot \sqrt{N \cdot C} \tag{4.1}$$

The chopping constant $k$ is an empirical value, dependent on the insulation medium and on constructional parameters of the CB. It is based on the arc's time constant $\Theta$ and it's equilibrium power $P_0$, which is also part of Cassie-Mayr's arc model. The equation does only represent the CB satisfactory, if the equivalent network shows capacitive behaviour in the frequency range of the arc's time constant. In other words, it is only valid to use the low frequency capacitance in (4.1), if the capacitive behaviour seen from the CB does not significantly change for very high frequencies. According to [37], the arc's time constant $\Theta$ for a $SF_6$ breaker of that time (year 1988) is in the range of 0.05 to 0.5 µs, corresponding to 5000 to 150 kHz ($f = 1/(2\pi \cdot \Theta)$). Due to the coil's unique manufacturing method, its capacity in the range of 32 nF should be dominating over other capacitive components in the network, as the connection lead to the CB is quite short. Further, Figure 2.4 indicates that it is reasonable to assume a capacitive behaviour in the previously specified frequency range. Thus, for the purpose of this project, Equation (4.1) is considered adequate.

For $SF_6$, according to [37], $k = 4...17 \cdot 10^4 AF^{-0.5}$. Calculating the total capacitance of the coil, the chopping current can be estimated with $i_c = 7...30A$.

The range of values in this estimation of chopping current is quite large, ranging from 5% to 22% of the rated current's value. Due to the previously discussed limitations and data available, the true chopping current's value remains unknown. At the same time, the value $i_c$ will significantly impact the OV's magnitude. Thus, as long as the value for the chopping current is constant, the simulation would still allow comparative conclusions regarding the qualitative effectiveness of potential counter measures. The value is chosen with $i_c = 7A$, which is the lower end of the previously specified range.

Furthermore, it is important to realise that this ideal CB model shows the worst case scenario. In the simulation, the current decreases from $i_c$ to zero within one simulation time step, i.e. 100 ns in simulation time, leading to a very steep current slope. In reality, the current will have a less steep slope due to the unavoidable inductances in the connection lead between CB and coil. Thus, the voltage rise should be more moderate in reality than in the simulation.

Alternatively to estimating $i_c$ based on a (sophisticated) CB model, a measurement at site could shed light on its true value. However, it would be necessary to carry out the measurement during operation at rated voltage. Thus, a HV current transformer with sufficient bandwidth and insulation strength is required. A current measurement at low voltage is not considered sufficient as the physical process behind the CC is dependent on the arc's energy and thus dependent on the arc current's value. Unfortunately, a measurement like this could not be carried out within the limited time frame allocated to this project.

### 4.1.3 Grid model and parameters

The FRT Test setup is connected to the public grid (31.5 kV line to line RMS voltage). Using a step-up transformer, the desired rated voltage of 62.5 kV for the testing setup is acquired. The grid's data is presented in Table 4.1. While the X/R ratio was assumed based on experience, the other values in the table were calculated using data provided by the transmission system operator and R&D Test Systems A/S at the FRT Tester's point of connection and data on the transformer used.

| Parameter | Value | Unit |
|---|---|---|
| Rated voltage (L-L) | 62.5 | kV |
| X/R ratio | 10 | |
| Short circuit power | 246 | MVA |
| Grid impedance | 1.58 + j15.7997 | Ω |

**Table 4.1:** Grid data used in the time domain simulation

Furthermore, a cable is added between the transformer and the 31.5 kV grid. Since detailed information are not available, it's shunt capacity and resistance is based on typical values found in [39] for a 30 kV cable with polymeric insulation. The cable ($185mm^2$ cross-section, VPE-insulated, $8mm$ insulation thickness, 30kV rated voltage) is considered with a shunt capacity of 62.6 $pF/m$ and a series resistance of 93.2 $\mu\Omega/m$. The length is approximated with $l = 2500m$. The cable's impedance is transformed to the 60kV grid, so that the transformer in the model can be omitted.

## 4.2 Model configuration

### 4.2.1 Single phase model

The time domain model will be simulated as a single phase only. In the real FRT tester, the three-phase CB is star-connected to a floating neutral point. As long as the CB is open, the coil is at the same potential as the grid voltage, since no DUT is considered in the simulation. Once the three-phase CB closes, symmetric three phase currents will add up to zero at that point. In the simulation, this would occur as the three coils would be identical. In the real FRT Tester, the CB's phases will not open simultaneously (i.e. the arc will not extinguish simultaneously). Thus creating an asymmetry at the neutral point for a short period of time. This can lead to reignition of the arc in some of the phases through a superimposed oscillation from a phase in which CC took place (virtual CC [17]). Thereby, the OV observed in the coil would be influenced across phases.

In the simulation, the CB is modelled in a very simplified approach. Due to it's idealised behaviour, virtual CC would not be represented. However, for the future work in this project, a more detailed CB model could be included, which would then also show interference between phases. Consequently, it is considered sufficient to model the coil in as a single phase circuit only, as long as no more sophisticated CB model is included.

### 4.2.2 Simulation and solver settings

In PLECS, two fundamentally different types of solvers can be chosen to simulate a given model: variable-step and fixed-step solvers. In the latter case, the user defines the length of a simulation time step and the software simulates the model using the linear state space equations and discretizing them according to the time increment. In the case of a variable-step type solver, the software adjusts the time increment in accordance with the dynamics of the simulation result. While in the fixed-step solver, the time increment has to be well balanced between the system dynamics and the computational effort, the variable-step solver eases this requirement to some extend. For the variable-step, a maximum step size can be defined to prevent the solver from 'missing' dynamic events. Of course, this increases computational effort throughout the simulation [40].

Further, PLECS offers two different variable-step solvers, DOPRI and RADAU, for non-stiff and stiff models respectively. A model is considered as 'stiff' if the model contains time constants are differing by several orders of magnitude [40].

Due to the greater computational efficiency, a variable-step type solver was chosen to simulate the previously developed model. Due to the high frequency oscillation resulting from CC, the model can be considered as 'stiff' and consequently the solver RADAU is adequate. The maximum time step is initially set to

1 ms and will be refined in case the simulation result is too coarse. Further, due to the inductance matrix' numerically small determinant, the option 'Use extended precision' was checked in the solver settings. Due to this option, PLECS calculates the state space matrices with higher precision [40].

### 4.2.3 Coil and event switch configuration

In the simulation, the entire coil will be energised, to observe the oscillations at resonance frequencies visible in the SFRA in Chapter 3.4.3. Therefore, the coil is connected as presented in Table 4.2 and Figure 4.1. The second event switch and also the DUT are not connected. The connection of the different voltage probes is labelled as Channel 1, 2 and 3, respectively. Channel 1 is connected from the grid to the event switch, parallel to the coil. Thus, Channel 1 is displaying the grid voltage as long as the event switch is closed. Channel 2 is the grid voltage, connected from the grid tap to ground. Channel 3 is connected in parallel to a section of the coil only: from tap 11 to tap 29, where the event switch is connected. The configuration of measurements is also presented in Figure 4.1.

| **Description** | **Connection tap** |
|---|---|
| Grid | 1 (0%) |
| Event Switch 1 | 29 (100%) |
| Channel 1 | 1 to 29 |
| Channel 2 | 1 to Ground |
| Channel 3 | 11 (35%) to 29 |
| DUT | - |
| Event Switch 2 | - |

**Table 4.2:** Tap configuration in the simulation. Winding percentage given in brackets.

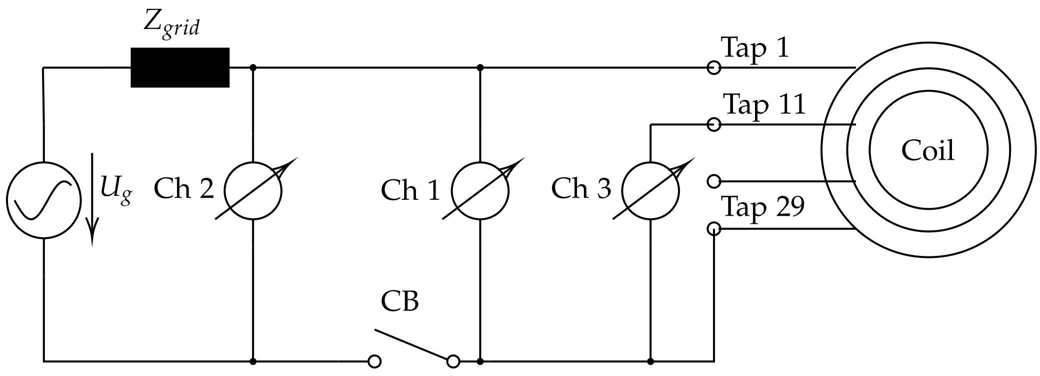


**Figure 4.1:** Coil and measurement configuration in time domain simulation

The time instances at which the event switch is operated in the simulation are shown in Table 4.3. It has to be mentioned that the instance $t_2$ has some tolerance to it: while the signal to open the switch is given at that instance in time, the defined CC value of $i_c = 7A$ adds some delay, as the the switch in the simulation only opens once the current reaches this predefined value (see Section4.1.2). The phase angle given refers to the grid voltage's phase angle.

| Description | Variable | Time [s] | Phase angle [deg] |
|---|---|---|---|
| Closing event switch | $t_1$ | 0.2067 | 120 |
| Opening event switch | $t_2$ | 0.4600 | 0 |
| End of Simulation | $t_{max}$ | 1 | 0 |

**Table 4.3:** Switching operations in simulation

## 4.3 Simulation results

The following section will comprehensively introduce the system's response observed in the simulation. After presenting an overview initially, the signal is analysed in more detail at significant time instances. Afterwards, the voltage distribution in the coil is assessed.

### 4.3.1 System level response

The simulated voltage response over the entire simulation duration is presented in Figure 4.2 as an overview. The Figures 4.3, 4.5 and 4.7 show important parts of the trace in more detail.

During $t < t_1$, the Grid voltage shows a 50 Hz oscillation with a magnitude of $62.5 \cdot \sqrt{2/3}$ kV. The voltage across the coil (i.e. Channel 1 and 3) is zero. At instance $t = t_1$, the event switch closes and the coil's inductance is energised. For $t_1 < t < t_2$, the voltage probe channel 1 is in parallel with channel 2 and thus shows the same waveform. Since the probe for channel 3 is only connected in parallel to a section of the coil, it shows a slightly distorted 50 Hz oscillation with smaller magnitude. At $t = t_2$, the event switch is opened and the defined CC occurs. This incident leads to a significant OV with a high frequency, measured by channel 1 and 3. The oscillation is decaying in amplitude over time.

Compared to the 400V switching test and switching OV theory presented in Chapter 2, the general shape of the response is reasonable. As visible in Figure 4.2, the high frequency oscillations in the coil are slowly decaying over time with a time constant of approximately $\tau = 0.42\ s$. In the measured switching response (see Section 2.4), the transient decays at higher rate, indicating a higher damping in the real coil. Thus, the model shows a worse case when considering the stress on the insulation. The OV's magnitude in this simulation reaches approximately

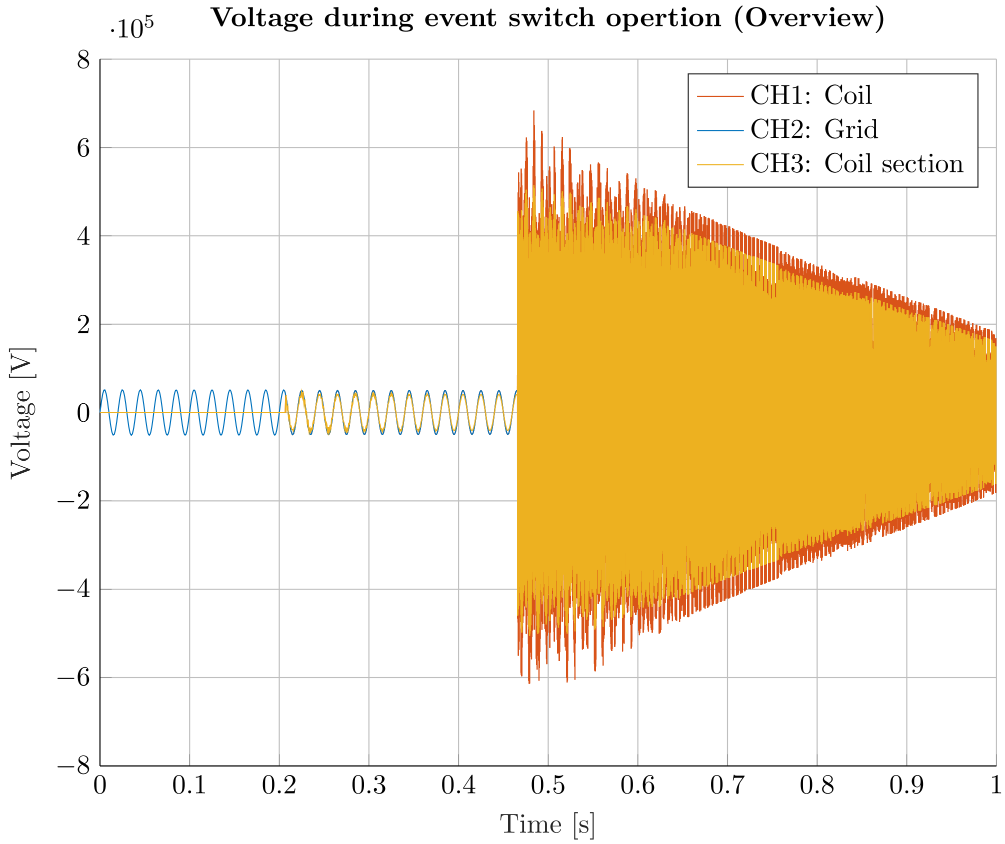


**Figure 4.2:** Simulated voltage response: Overview

11 p.u. of the phase-ground peak voltage in the grid. Considering the approximation in the 400 V switching measurements showed a magnitude of 9 p.u., the simulation results is reasonable as both values are within the same order of magnitude. Naturally, changing the value $i_c$ in the simulation could correct this error. The simulated OV's magnitude gives an initial approximation for the stress applied to a reinforced insulation system, as discussed in Section 5.1.1.

To assess the response in more detail, Figures 4.3, 4.5 and 4.7 present selected instances in the response, augmented by the signal's Fourier transform (FFT) in Figures 4.4, 4.6 and 4.8. The FFT's fundamental frequency is always 50 Hz and considers the first 0.02 $s$ (one period of the power frequency) after the incident (i.e. closing or opening the CB or starting the simulation).

### Initialisation

For the first tens of milliseconds, the measured grid voltage is distorted by a oscillation at a frequency of 3550 Hz, as evident from Figures 4.3 and 4.4. The oscillation's

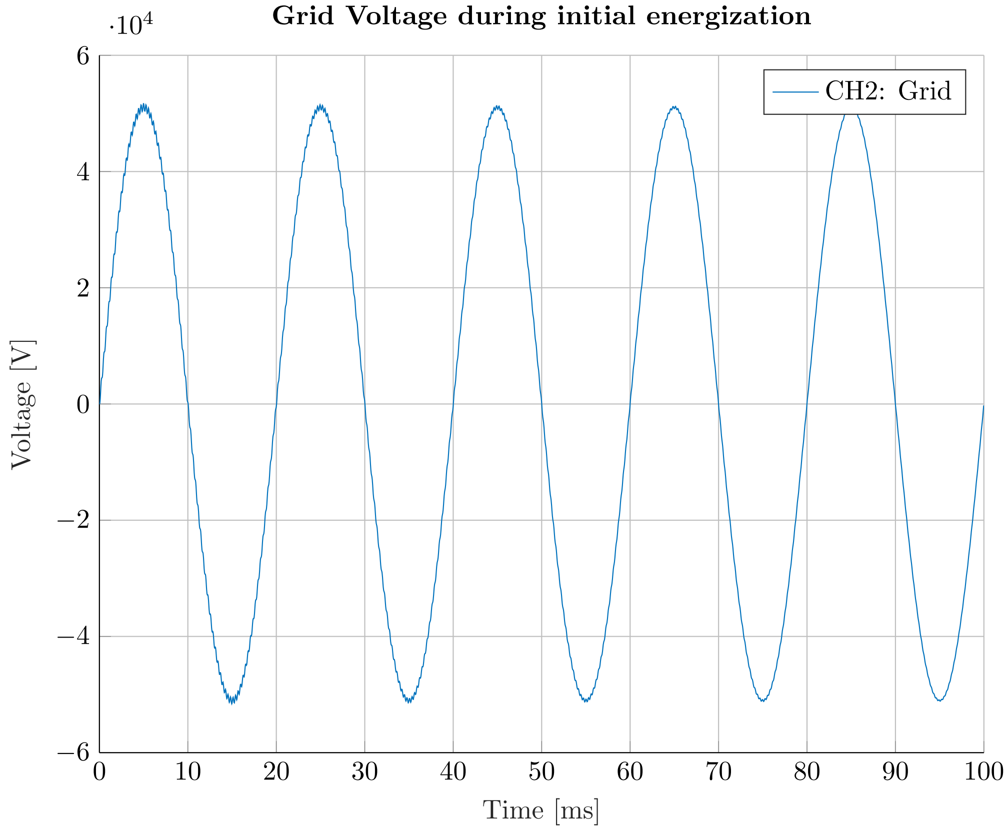


**Figure 4.3:** Grid voltage shortly during initial model startup

frequency corresponds to the resonance frequency of the grid's inductance and the cable's capacitance (see also Table 4.1):

$$\omega_r = \frac{1}{\sqrt{15.8\Omega/(100\pi) \cdot 15.9pF/m \cdot 2500m}} = 3559.6Hz \cdot 2\pi \tag{4.2}$$

This oscillations magnitude of approximately 300V is small compared to the fundamental's magnitude.

### Closing event switch

As a response to closing the event switch and energising the coil, the system shows the signal presented in Figure 4.5. In this graph, Channel 1 is not visible, because it is zero up until the closing instant and then equal to the grid voltage for $t > t_1$.

The voltage measured by Channel 1 and 3 increases from zero the grid voltage's value in the instant of closing the switch, charging the coil's parasitic capacitance. The voltage response after closing the event switch, during and shortly after the coil's energisation shows frequency components at 3.6 kHz, 12.3 kHz and

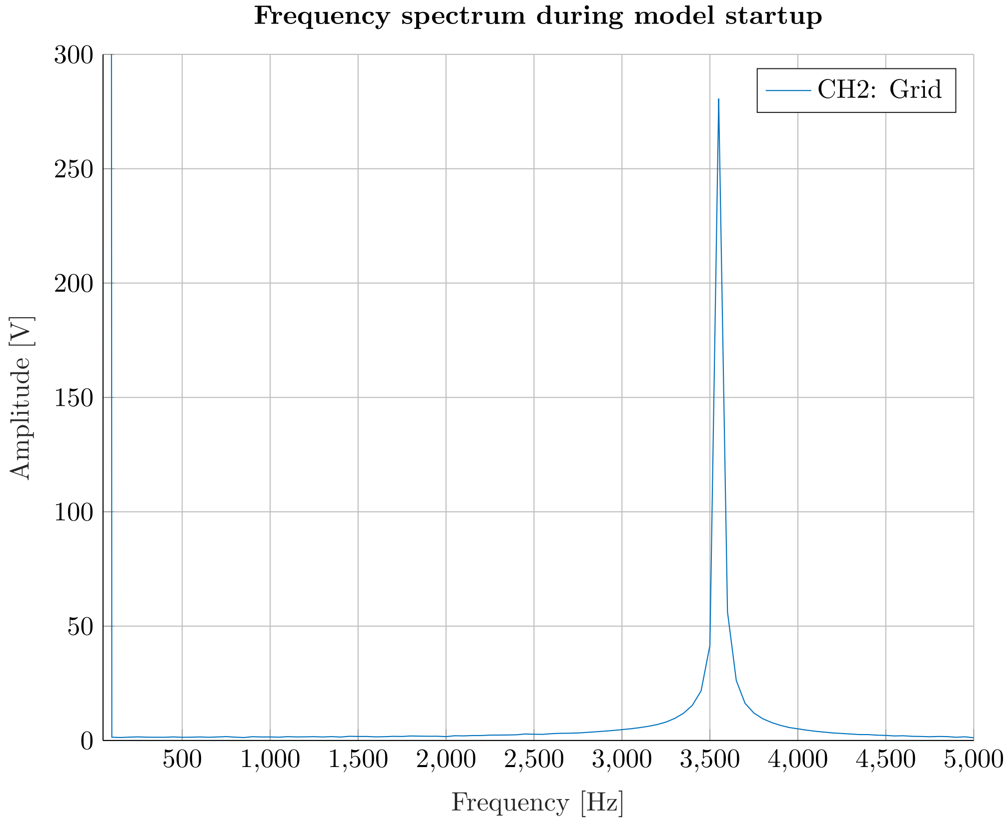


**Figure 4.4:** FFT of the signal presented in Figure 4.3

18.8 kHz, as evident from Figure 4.6. The grid voltage is also slightly distorted by a high-frequency component, which is dominated by the grids resonance frequency at 3.55 kHz.

The frequencies in Channel 3's signal do not correspond to the resonances observed in the SFRA measurement (see Sections 2.4.2, 3.4.3 and 3.5.2). The reason is the grid's influence: If the coil is considered as an autotransformer with Channel 3 across the (unloaded) common winding, then the common winding is in parallel to the series connection of series winding and grid (see tap configuration in Figure 4.1). Thus, the observed frequency spectrum is influenced by the grid parameters and the resonances are not shown in the SFRA. The magnitude of the 18.8 kHz component is approximately 3.4 kV, which is equivalent to 6.67% of the grid voltage's peak value. Compared to the magnitudes reached when breaking the current through the coil, these values can be considered small and are most likely not violating the insulation system's dielectric strength.

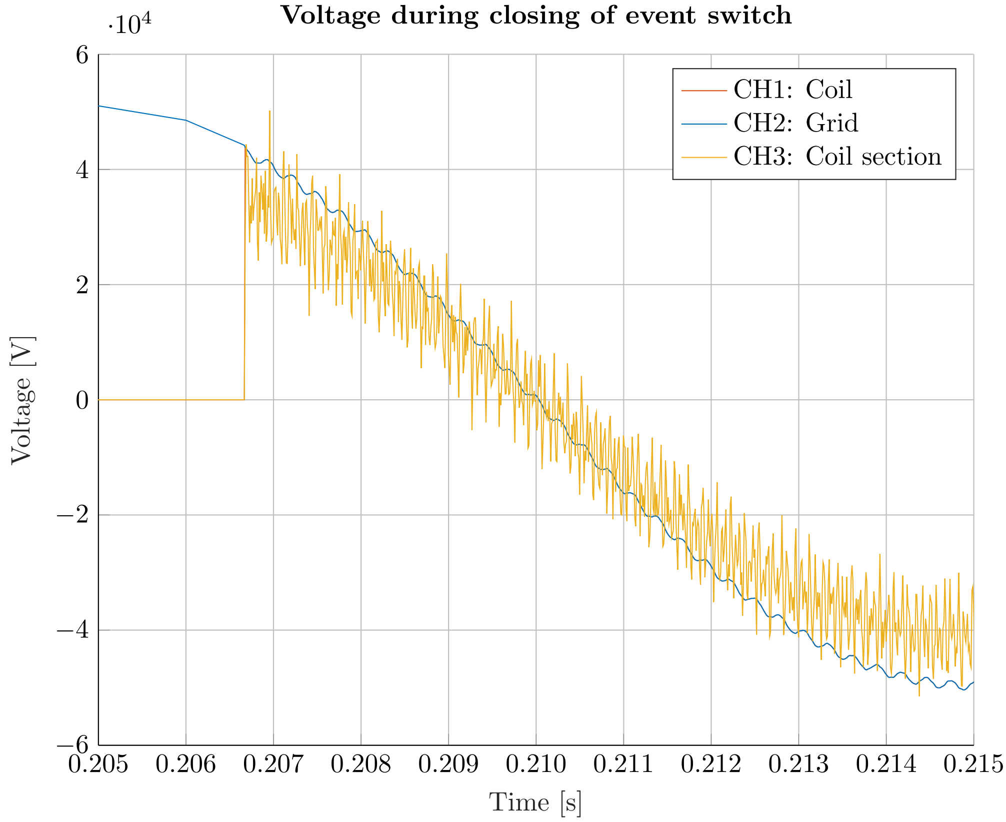


**Figure 4.5:** Voltage response during closing operation of event switch

### Opening event switch

The systems response to opening the event switch and breaking the current in the coil with the defined CC is presented in Figure 4.7. The corresponding FFT of Channel 1 and 3 is shown in Figure 4.8. The grid voltage in Channel 2 is only distorted by a 3.55 kHz component, which is the grid model's resonant frequency, and is thus not included in the graph.

The voltage response in Figure 4.7 shows that the voltage across the coil increases significantly after the current was chopped. The highest voltage magnitude visible in the selected time window reaches almost 600 kV (Channel 1, across entire coil). The signal further shows a high frequency oscillation with multiple frequency components, as the voltage waveform is not sinusoidal but distorted in some instances. The FFT in Figure 4.8 reveals that the signal contains components at 7 kHz, 14 kHz and 21 kHz.

The observed frequency spectrum coincides well with the impedance characteristic measured in the SFRA and modelled in the frequency domain. The SFRA is plotted in Figures 3.4 and 3.6. The time and frequency domain simulations

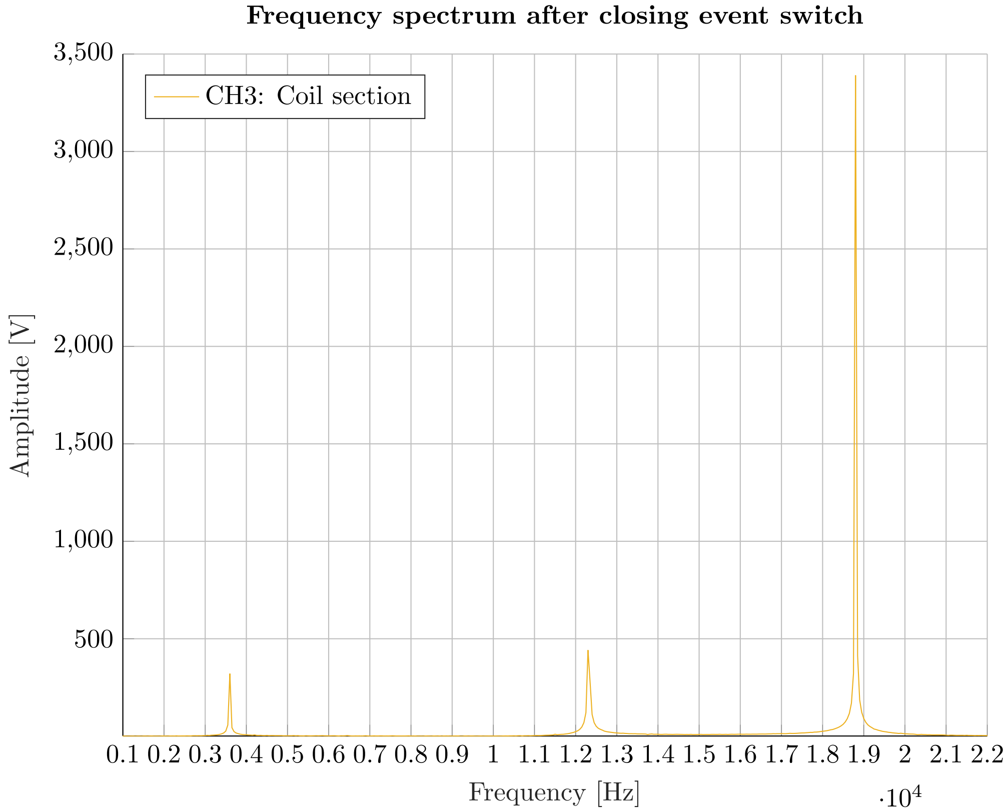


**Figure 4.6:** FFT of the signal recorded by Channel 3 in Figure 4.5

showing the same frequency characteristics builds trust in the time domain model and is further supported by the theory in Chapter 2. The FFT also indicates that the component at the first resonance frequency (7 kHz) has by far the greatest magnitude. In the physical coil this frequency component is also projected to be the most severe as the damping due to higher frequency effects (e.g. skin effect) has reduced influence in that case. Thus, potential counter measures against the discharge incidents could be aimed at reducing the magnitude of this component.

The magnitude of more than 500 kV for a duration of at least 0.1 seconds (see also Figure 4.2) would explain the discharge incidents: If a linear voltage distribution in the coil's winding is assumed, this magnitude would correspond to approximately $V_{turn} = 500\ kV/1260\ turns = 0.4\ kV/turn$. Thus, the voltage between adjacent cooling ducts could reach up to 40 kV. Considering the distance between the cooling ducts (6.3 cm), the breakdown field strength of environmental air in a *uniform* electric field (25 kV/cm) and the most likely non-uniform E-Field distribution on the winding's side, this OV could already violate the insulation's strength. Further, the pollution discussed in Section 2.3 reduces the insulation strength. However, the simulated OV is still far from violating the strength of the

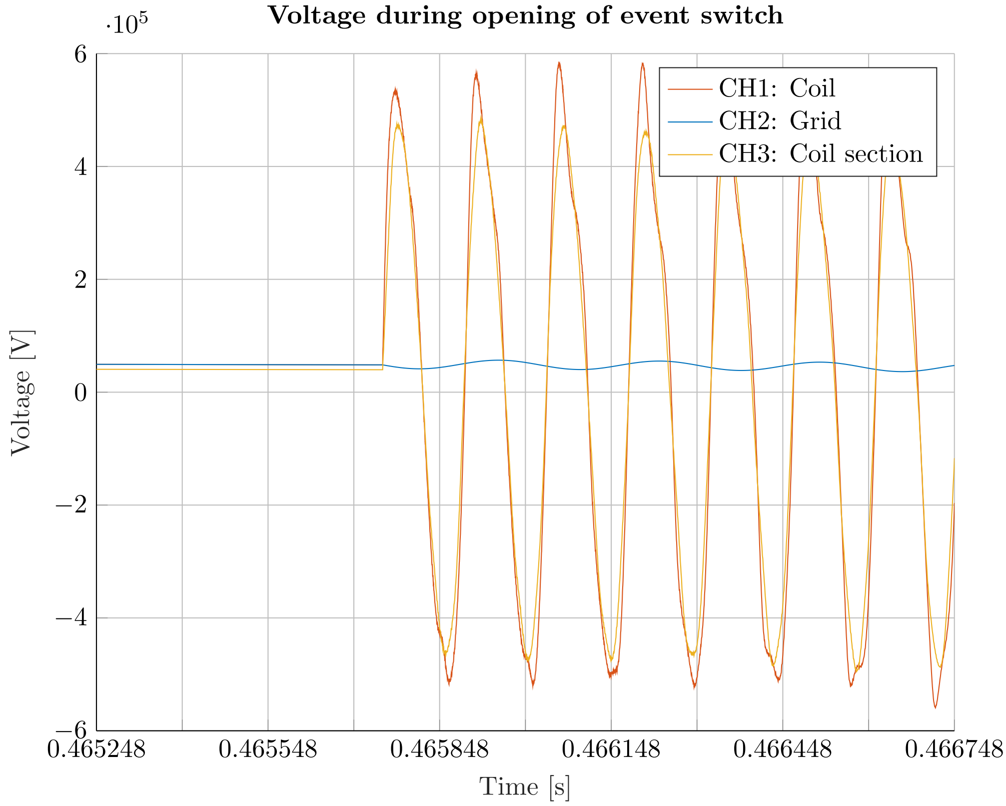


**Figure 4.7:** Voltage response during opening operation of event switch

turn to turn insulation in the uniform field between the turns (insulation strength: 55 kV/mm, as evident from Table A.1).

### 4.3.2 Voltage distribution in winding

A major advantage of the time domain model compared to measurements on the real coil is the possibility to display the voltage of each (lumped) turn. The *turn to turn voltage* refers to a hypothetical voltmeter being connected to adjacent turns, across the insulation. The cumulative sum of the turn to turn voltage reveals the spatial voltage distribution in the coil, referred to as *turn voltage*. This would be equal to attaching one of the voltmeter's probes to the first turn and the other to an arbitrary turn, measuring the voltage across multiple turns at once. Thus, once the event switch is open, the grid's voltage does not influence the turn voltage, because there is no current flowing through the coil. The current is only oscillating inside the coil, exchanging energy between the capacitive and inductive elements. When measuring from any turn to ground, the grid's voltage would be visible as it would be equal to measuring across the grid's open terminals (i.e. the open CB).

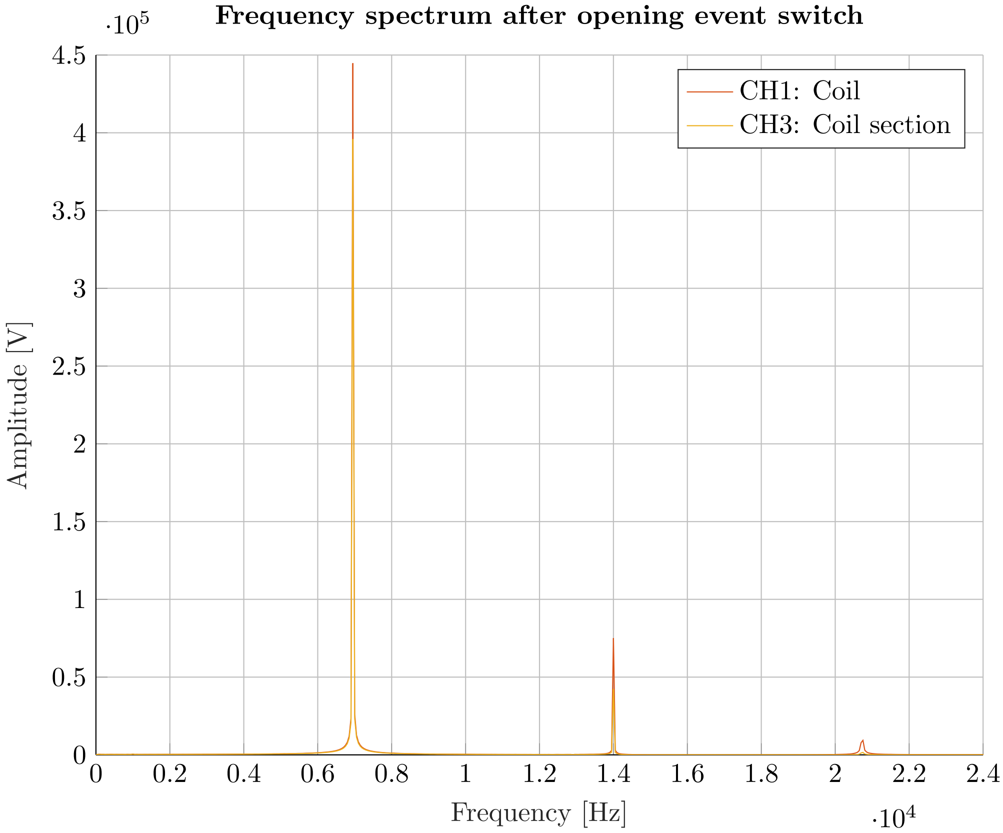


**Figure 4.8:** FFT of the signals recorded by Channel 1 and 3 in Figure 4.7

Since the discharges at the coils are observed across several turns, studying the *turn to turn* voltage instead of the turn to ground voltage is reasonable.

The analysis of the spatial voltage distribution is of great interest as it would reveal internal resonances, as discussed in Section 2.5. The voltage profile could hint at regions inside the coil which are more prone to discharges due to an increased turn to turn voltage. Such discontinuities could offer the possibility to reinforce the insulation in highly stressed regions only, offering a more cost-effective solution compared to altering the entire insulation.

The surface plot in Figure C.1 shows the spatial turn voltage distribution as a function of time and number of turns shortly after CC. The turn to turn voltage in Figure C.2 can be considered as the graph's gradient with respect to the number of turns. Both Figures can be found in Appendix C.

As evident from figure C.1, the previously observed frequency components (see Figure 4.8) interfere with each other. The voltage for number of turns $n = 1260$ is equivalent to the 2D graph presented in 4.7. The turn to turn voltage in Figure C.2 further shows that the voltage distribution can no longer be assumed

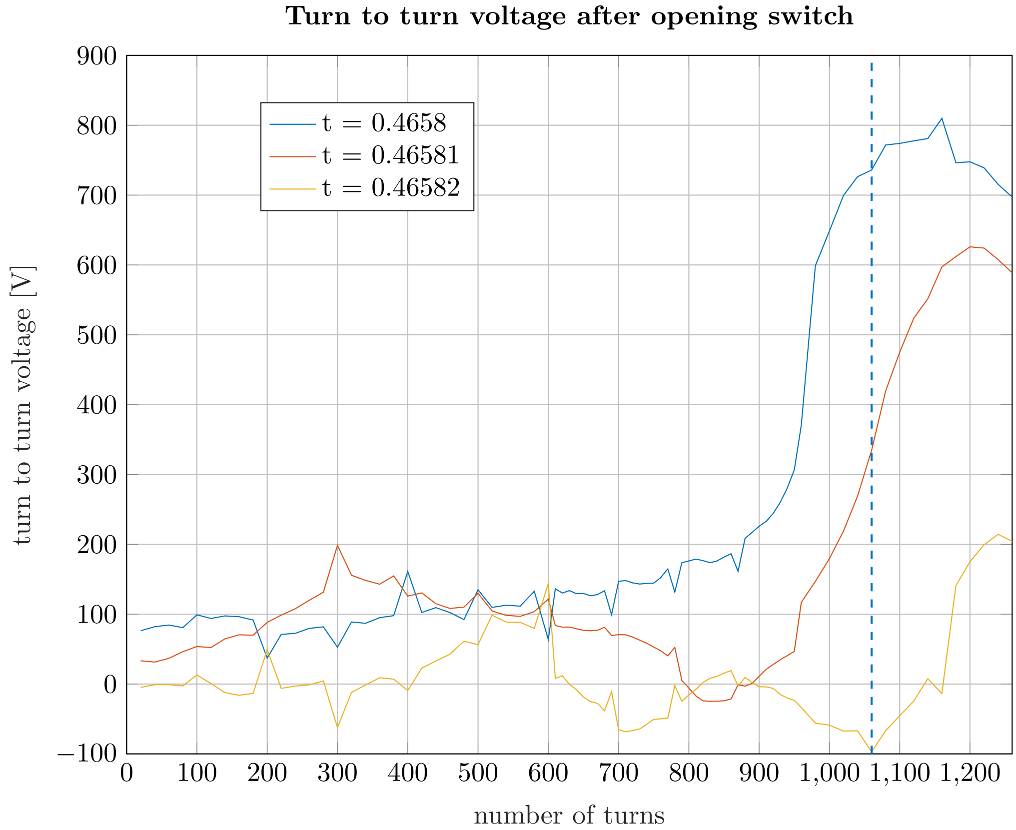


**Figure 4.9:** Turn to turn voltage after current chopping.

as linear: for some instances in time, the turn to turn voltage ranges from negative values to more than 700 V per turn. To further illustrate this point, the 2D plot in Figure 4.9 is presented. Assuming a constant turn to turn voltage amplitude of 700 V, the transient would lead to a voltage drop of approximately $700\ V/turn \cdot 90\ turns = 63\ kV$ between two adjacent cooling ducts in the outer coil's segments. This magnitude is equal to the grid's phase to phase RMS voltage and most likely violates the insulation strength of environmental air in the non-uniform E-field around the coil. Potentially, a reinforced insulation could mitigate discharges at the coil in this region (see Section 5.1.1).

In general, the turn to turn voltage increases with the number of turns, towards the coil's outer layers. A reason for this behaviour could be that the CB, the transient's source, is connected to turn 1260 in the simulation. Thus, for turns at the beginning of the coil, the CC instance is damped more as most of the coil is in series with the CB, resulting in more a gentle current slope. Further, discharges on site were often observed in the electrical vicinity of the CB connection tap, supporting this hypothesis.

However, the absolute value of the OV does most likely not appear in the physical system as the selected value $i_c = 7\ A$ has a major influence on the OV's magnitude. Integrating the turn to turn voltage over the number of turns in Figure 4.9 at $t = 0.4658\ s$ (blue curve) shows that in that instance in time 50% of the coil voltage drops between turns 1060 and 1260, i.e. across approximately 16% of the winding only. This is indicated by the vertical dashed line in the figure. This strongly non-linear voltage distribution is independent of the value $i_c$ and illustrates the stress on the insulation in the coil's outer sections.

Further, especially in the first voltage cycles after CC, the turn to turn voltage reveals some discontinuities in its profile (Figure C.2). These always correspond to the turns adjacent to the cooling ducts (e.g. turns 200, 600 or 1060) and seem to oscillate with a high frequency component, superimposed on the coil's resonance frequencies. These discontinuities are also visible in Figure 4.9 as small voltage spikes. These oscillations occur due to the coil's internal resonances at these discontinuities and can be considered part-winding resonance (PWR). Some theory and sources behind PWR is presented in Section 2.5. However, due to their small amplitude, these PWR are not considered harmful for the insulation system. Thus, PWR are not considered seperately in the discussion of mitigation methods in Chapter 5.

On the other hand, the model's limitations have to be kept in mind when assessing a high frequency phenomenon like this: It is foreseeable that the idealized CB model does not stress the coil in the same fashion its physical counterpart, since in the simulation, the chopping current's slope is only dependent on the simulation time step. At the same time, multiple restrikes around the natural current zero crossing can be considered a high-frequency periodic excitation of the coil (see Section 2.4 and [17]). Thus, it is challenging to predict to which extend PWR are stressing the coil internally, since a more sophisticated model would be necessary to motivate a definitive answer on this question.

## 4.4 Summary

This Chapter introduced and discussed the required auxiliary components for the time domain simulation. Further, the model's settings and configuration are presented. Afterwards the simulated voltage signal as a response to the operation of the event switch (circuit breaker, CB) is analysed in detail.

The simulation showed a significant OV as a response to CC. The frequency spectrum of that voltage contains the resonance frequencies observed in the SFRA in Chapter 2 and 3. Studying the spatial voltage distribution in the coil revealed that the voltage per turn (turn to turn voltage) is varying significantly in dependence of the location. The turn to turn voltage can reach values of more than 700 V, which corresponds to 63 kV between two cooling ducts. This would most likely violate the insulation strength of environmental air in the non-uniform field around the coil. Further, the analysis showed that the outer coil sections are stressed more than the inner sections. This is in line with the observation that all observed discharge incidents were also located in the vicinity of the CB tap.

The discussion and analysis in this Chapter revealed two general approaches for mitigating the discharges on the coil's side (details in Section2.1): Counter measures can be aimed at reducing the stress on the insulation by reducing the OV's magnitude, or the insulation can be reinforced. The OV's magnitude can be reduced by either decreasing the chopping current value, extracting energy from the system in the frequency range of the oscillation (e.g. through filters) or by protecting the coil from OVs through surge arresters, for example. A comprehensive discussion and simulation of some selected methods for mitigation is carried out in Chapter 5.

# Chapter 5

# Countermeasures against discharges

*Based on the simulation results in Chapter 4 and the knowledge about the discharge incidents, potential counter measures to mitigate these flashovers in the future are presented and discussed in this chapter. Selected methods are also incorporated into the time domain simulation to determine parameters and analyse their effectiveness.*

## 5.1 Discussion: Mitigation approach

There are two fundamentally different approaches to mitigate the observed discharges in the future: increasing the insulation's dielectric strength or decreasing the dielectric stress on the insulation. To allow a comprehensive discussion on the mitigation approaches, the main ideas are presented below:

1. Increase dielectric strength:
   (a) Submerge entire coil in oil
   (b) Cover aluminum foil edges (winding) in solid insulation (e.g. resin)
   (c) Cover exposed winding in cooling duct with solid insulation
   (d) Reduce and prevent pollution on coil's surface
2. Decrease dielectric stress:
   (a) Protect coil from OV by surge arresters (SA)
   (b) Reduce chopping current value
   (c) Damp oscillation at resonance frequency after current chopping

The aforementioned approaches are explained and discussed in detail in the following two subsections, enumerated with their respective number in the list.

### 5.1.1 Increasing insulation strength

The previously listed measures to increase the insulation strength all face the same fundamental problem: The current dielectric strength of the insulation system is unknown and the stress can only be estimated. The latter is the case mostly due to the simplified CB model as discussed in Section 4.1.2. Using a validated and more sophisticated model of the CB, the value of the chopping current $i_c$ could be estimated with larger accuracy. Alternatively, an on-site measurement of the current waveform through the CB during operation would shed light on the true value of $i_c$. The value would then justify the selected chopping current value and the thereafter observed switching OV. If the measurement was carried out multiple times, different values of $i_c$ would be measured as the physical process of arc interruption has some statistical variance. The improved insulation has to be able to withstand the worst case, i.e. the OV due to the highest recorded value of $i_c$. Observed discharges during these experiments would imply conclusions regarding the current insulation system's strength. However as this method is rather imprecise due to many influence factors and parameters. The insulation's strength could also be assessed by analysing samples of it in a HV laboratory. For this purpose, an impulse generator (Marx generator) could be used. Experiments in the laboratory would further permit testing of the effectiveness of the proposed methods to increase the dielectric strength at relatively low effort.

Despite this fundamental challenge when designing one of the proposed solutions, the general idea of the proposed mitigation approaches as well as further challenges associated to the specific approaches can be discussed.

**1a Submerge coil in oil.** Insulating HV components in oil, as proposed in approach 1a, is a mature and widely-spread solution for HV transformers and other devices. For all oil-insulated components there are a few aspects, which can delimit the applicability and have to be considered beforehand, e.g environmental constraints in e.g. water reservoirs and the fire load of oil. In the specific context within this project, the oil insulation faces another significant challenge: The coil's 29 tapping points are currently freely accessible, as shown in Figure 1.2. In its current insulation configuration all devices (event switches, DUT, grid) can be connected to any of the taps. This flexibility is desired and necessary for the operation of the FRT Tester to set the desired residual voltages and voltage distortions for the DUT. Thus, if the coil was submerged in oil, all 29 tapping points would need to be lead out of the oil tank. While it is a mature technology to lead a HV connection through an oil tank, the amount of taps increases the cost and complexity of the insulation system.

Additionally, the oil insulation would increase the effort to transport the coils to another site. This aspect should not be forgotten, since the FRT Tester is designed to be disassembled relatively effortlessly, to test another wind turbine.

**1b Cover winding foil edge.** As previously described, the coil mostly consists of wound layers of solid insulation material and aluminium foil (Sections 1.2 and 3.1). It is foreseeable, that electric field strength at the aluminum foil's edges will exceed the uniform field between the turns significantly [7]. The foil edge is thus a weak spot in the insulation system as the dielectric strength of environmental air surrounding the edges is low. A feasible approach to prevent discharges originating at the foil edges could be filling the void between insulation layers (see Sketch 3.1) with an insulation medium of higher dielectric strength. Potentially, it would already be sufficient to cover the foil edges with a thin layer of insulation material only.

With respect to the constructional challenges and effort, utilising varnish or resin with suitable viscosity poses a prominent solution. These could be applied to the aluminum foil edges without disassembling the coil. Especially in the case of using resin, cavities filled with air in the highly stressed field regions (i.e. in close vicinity of the foil edges) have to be avoided. Cavities would be a source of discharges and lower the insulation's life time significantly. Therefore, the effectiveness of this mitigation approach is highly dependent on overcoming the practical challenges when applying the resin. Usually cavities in insulation systems are avoided by drying the device in a vacuum environment. This seems infeasible due to the coil's large physical dimensions and thus an alternative solution would need to be found.

**1c Cover winding in cooling duct.** The winding on one side of a cooling duct is not covered by insulation material, as shown in the Sketch 3.1. The detailed study of the burning marks, using a camera probe, indicated the origin or termination of the discharges at the exposed winding in the cooling ducts. Thus, the insulation system's strength could be improved by covering this winding spot. It is probably infeasible to add another layer of the polymeric insulation material already used in the coil. The reason is that its implementation would require the disassembly of the entire coil, due to the axial spacers seen in Figure 3.1. Thus, a similar approach as previously mentioned, using varnish or resin, seems more efficient. Similar challenges regarding air-filled cavities and their adverse effects would apply in this case. Further, both approaches 1b and 1c could be combined to increase the effectiveness in preventing discharges.

**1d Remove and prevent pollution.** The adverse effects of (conductive) pollution on insulation systems and surface discharges were already comprehensively discussed in Section 2.3. It is therefore clear that the insulation system's strength could be improved by removing and preventing the coil's pollution. Some measures were already implemented at site and are described in Section 2.3. However, despite these counter-measures, discharges were still recorded after the implementation. At the same time, one major shortcoming of the current cooling system can be identified: In its current form, a fan is used to blow environmental (polluted and humid) air at the coil. By drying and cleaning the air before using it for cooling purposes, the pollution load could be reduced. On the other hand, it is uncertain, how significant the pollution's impact on the insulation strength is, since no structured and comprehensive measurement or assessment on this topic was performed yet.

Considering the previously mentioned aspects, the options 1b and 1c (using resin or varnish), or a combination of both, seem to be the most reasonable to increase the insulation's strength. The options can be implemented without disassembling the coil and thus pose a solution with relatively low effort. However, before the implementation, their effectiveness must be assessed experimentally, or at least in a computer simulation. For the latter, a comparative FEM simulation with the current state and improved insulation suggests itself. This simulation would need to model each turn individually and would thus need to be quite detailed, while also considering impurities and air cavities in the insulation system. These considerations give rise to concerns regarding the accuracy of the FEM simulation and thus these questions need to be assessed prudently beforehand. Naturally, only a section of the coil would be assessed as a sample experimentally or modelled as proposed.

The oil insulation (approach 1a) is considered too complex with respect to the accessibility of all 29 taps. The drawbacks of the oil insulated coil require prudent and extensive work before implementation. Other issues, such as the challenges when transporting the coil, have to be considered as well. The oil insulation might be feasible for a new, redesigned coil with an entirely reworked insulation concept. In that case, the choice for the solid turn to turn insulation material should also be reevaluated. Potentially an automatic tap changer inside the oil tank could lower the amount of connections lead through the tank to the outside.

Despite the adverse effects of pollution on the insulation, counter measures against it should only be further analysed and studied, after the pollution's impact was evaluated in more detail. At the current state, the information available can not justify extensive counter measures (e.g. an air filtration system) against saline pollution on the coil.

### 5.1.2 Decreasing stress on insulation

Compared to increasing the insulation's dielectric strength, it can also be a feasible option to lower the stress on the insulation. This can be achieved in a few different ways, which have been listed previously and are discussed below.

**2a Surge arresters to protect coil.** A surge arrester (SA) is a device commonly used to protect HV equipment, for example transformers, against OVs. SA can be electrically considered as a voltage dependent resistor: Once the voltage exceeds a certain threshold value (rated voltage), a SA's resistance decreases to a defined value, exposing the protected device to a defined residual voltage only. Thus, they pose a prominent approach to protect the coil within this project as well. One major challenge is the correct determination of the SA's rated voltage with respect to connection configuration as the SA must only trigger when the coil is stressed by an OV and not during normal operation [7], [17], [18], [41].

Because SA are so widely spread and pose such a prominent solution, their application within this project has been studied as part of the 400 V switching tests performed by R&D Test Systems A/S (see Section 2.4). In the measurement campaign, SA were replaced by LV varistors to assess the effectiveness. It was found that a varistor from the event switch (CB) tap to the grid tap, in parallel with the coil, gave the most promising results. As sketched in Figure 1.1 and described in Chapter 1, the FRT Tester has two event switches and thus both would need to be equipped with SA. A permanent installation of the SA is desired to facilitate the FRT Tester's operation. However, it is then challenging to select SA with the correct rated voltage: In the tap configuration sketched in Figure 5.1, if event switch 1 (EV1) is permanently open (unused) and EV2 is closed, the voltage drop across SA1 would exceed the grid voltage, because SA1 is connected in parallel with the common and the series winding of the resulting auto-transformer ("auto-transformer effect"). If the SA's rated voltage was only slightly above the grid voltage, it would trigger and interfere with the FRT Testing. Also, the SA would potentially act as a source for transient distortion of the voltage. Thus, the SA's rated voltage has to be significantly higher than the grid voltage, since in the most extreme case less than 30% of the coil's impedance is used between grid and CB. After internal discussion and analysis a SA with a rated voltage of 96 $kV$ was selected. The rated voltage exceeds the grid's peak phase to ground voltage by a factor of approximately 1.8. SA with these specifications were then installed at site by R&D Test Systems A/S as a consequence of the measurement campaign. However, despite the installed SA, flashovers at the coils were still observed afterwards.

According to [18], SA do not protect the device against the steep front of the incoming voltage surge as they do not trigger with the rate of rise of voltage. In the initial moments, the winding section closest to the connection of the surge's source (i.e. the CB in this case) are stressed significantly, which can lead to discharges. Therefore, with respect to [18], the coil would not be fully protected by a SA alone. This could be a reason for the prevailing discharges after the installation of SA. Also, with consideration of Section 2.5, the SA would not protect the coil against internal resonances. These can be excited by voltage surges and lead to localized stresses exceeding the coil's insulation strength.

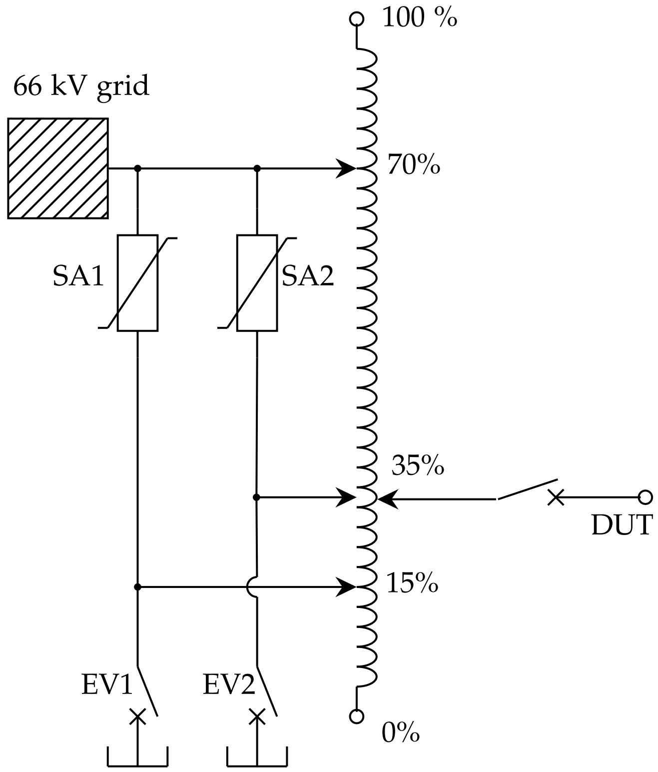


**Figure 5.1:** Simplified single-line diagram of FRT tester with surge arresters

**2b Reduce chopping current.** In Chapter 2 and 4, current chopping was identified as the root cause of the problem. Further, literature [7], [17] show that the magnitude of the chopped current is proportional to the resulting OV. Thus, it is natural to discuss measures to reduce $i_c$. There are mainly three options which propose themselves:

- A resistor in series with the CB.
- A capacitor in parallel with the coil.
- Exchange the CB with a model better suited for small currents

The first two options primarily aim at altering the current's power factor. As discussed in literature, current chopping is mainly occurring when the CB interrupts small, inductive currents [17]. If the power factor of the current is changed by the means of a capacitor or resistor, current chopping might be less likely to occur as the current would be less inductive.

The resistor in series with the CB would also reduce the current's magnitude and damp the resulting oscillation. It is uncertain, if this is beneficial, because on the one hand a lower current magnitude in general could lead to a smaller value of $i_c$, if the current is still chopped at the same phase angle. On the other hand, considering the physics of the unstable arc around the current's zero crossing (see Section 2.4), it is imaginable that the smaller current magnitude leads to a higher probability of current chopping, in which case the problem might even become more severe.

Another option is to reduce the chopping current would be to exchange the CB and utilise a model which is better suited for interrupting inductive currents within the range of 60...2000 $A$, as specified and discussed in Section 2.4. In this case, another CB technology can be considered as well. However, it is known that also vacuum circuit breakers are especially prone to current chopping. In recent times, also $CO_2$, Air and alternative gas mixtures in CB have seen increasing popularity, due to the negative environmental impact of $SF_6$ [42].

**2c Damp oscillation at resonance frequency.** Another approach to delimit the OV at the coil can be to damp the oscillation at resonance frequency resulting from current chopping. There are a few different options to implement this into the FRT setup:

- A filter or snubber circuit in parallel with the entire coil
- A tuned RC-component across a winding section or the entire winding
- An additional, open, and magnetically coupled turn terminated with a tuned RC element

Snubber circuits can be used in various applications to protect medium voltage (MV) devices, for example transformers but also capacitor banks, against transient OV, such as switching OV [18], [43], [44]. These circuits usually consist of a series connected RC element in parallel to a SA. Often, the RC element is also protected by a fuse to prevent excessive currents from damaging the capacitor and resistor. In the application at hand, the snubber circuit would be installed in parallel with the entire coil, as suggested in [18], [44]. The idea behind the snubber circuit is that the RC component decreases the rate of rise of the voltage by providing an alternative path for the coil's current once the arc in the CB extinguished. The SA would not be triggered under normal operation circumstances and expected chopping current values. After current chopping, the snubber circuit dissipates the energy stored in the coil and thus damps the oscillation, as discussed in [18], [44].

If the snubber circuit is permanently added into the FRT test setup, the same challenge as previously discussed for the SA arises: If only a section of the coil is energised, the snubber circuit is exposed to voltages beyond grid voltage (similar to the situation in Figure 5.1). Thus, selecting the appropriate rated voltage might be challenging.

For the tuned RC components in the different configurations as mentioned in the list above, the idea is comparable: While acting as a very high impedance for power frequency, the capacitor shall be tuned to let a current pass at resonant frequency of the coil. The resistor would then dissipate active power and thereby damp the oscillation in the coil. When the RC element is connected in parallel to a section of the coil, it has to withstand the voltage drop across these turns while one of the event switches (CB) is closed. Thus, depending on the amount of turns selected, the RC-component's voltage rating has to be adjusted accordingly. The tap configuration of grid and event switch largely determines the voltage drop per turn. Thus, the worst case, i.e. highest voltage drop per turn, has to be considered for the component's rated voltage.

Instead of using existing turns in the coil, another open turn could be added as well. This turn would only be capacitively and inductively coupled, while being galvanically isolated. The open terminals of this damper winding (DW) would be closed through the series-connected, tuned RC element.

The previous discussion showed that the permanent installation of SA, as proposed in 2a, is challenging due to the increased voltage drop across the SA attached to an unused event switch (see Figure 5.1. Further, despite the installation of SA as specified, discharges were still observed at the coil and can thus not be considered as a feasible solution to the problem on their own. An explanation is that SA do not trigger with the rate of rise of voltage but only depending on the voltage's magnitude, allowing the surge voltage to initially propagate into the coil. Thus, the coil's winding sections in the CB's electrical vicinity will be highly stressed according to [18].

For the analysis of reducing the chopping current value (item 2b) and the assessment of the measures proposed, the computer model's limitations have to be considered: The CB model used in the simulation is based on an ideal switch and a predefined value of $i_c$ (see Section 4.1.2). Therefore, the impact of a resistor in the CB path or a capacitor could not be assessed as the CB model does not use information on the current's power factor. Instead of a predefined current chopping value, the current's phase angle at which the switch is opened, could be defined and thus a lower value of $i_c$ achieved, when adding a resistor in series. Naturally, this would lower the OV observed in the simulation. However, it must be questioned if this would resemble the response observed in reality. As the physical process behind the current chopping is so complex (see Section 2.4 and Literature [7], [17]), it is almost certain that the model would not give an accurate representation of reality. While more sophisticated models to simulate the arc's behaviour in the CB [17] exist, the amount of data required makes those infeasible for this project. These limitations also apply to the suggested idea of exchanging the CB with a better suited model, capable of switching smaller currents without current chopping. The latter approach would also imply a significant monetary investment, which might make exchanging the CB only feasible in a second, new and reworked FRT test setup.

Thus, the measures for reducing current chopping (item 2b) are dismissed solely due to the simulation's limitations. Since these measures pose a prominent solution in theory, their applicability should be assessed prudently in a separate project.

The final approach 2c of damping the OV created by current chopping seems to offer a solution which can be incorporated into the existing FRT setup with reasonable effort and moderate investment (compared to submerging the coil in oil, for example). While the snubber circuit will be exposed to voltages higher than the system voltage due to the "auto-transformer effect", this problem is alleviated by the use of a RC component only, which would be attached to a fixed number of turns or an additional DW only. Still, if the voltage stress on the snubber in the worst case is known, it's components can be selected accordingly.

The SA as part of the snubber circuit will also protect the RC element against OV. A major benefit of the RC element compared to the SA by itself is that it also alters the steepness of the voltage surge due to it's time constant. This lowers the stress on the winding section in the CB's electrical vicinity [18]. Also, this measure reduces the risk of restrikes and pre-strikes since it reduces the rate of rise of the TRV, alleviating stress on the CB's gap between contacts. While the changed steepness of the TRV will be visible, it's impact on restrikes and pre-strikes can not be assessed due to the simple CB model.

### 5.1.3 Summary

The measures proposed to increase the insulation's strength all face the fundamental challenge that the dielectric strength of the system in reality is unknown and can also not be assessed with the simulation at hand. Comprehensive measurements, e.g. the assessment of insulation samples in the laboratory, or a fundamentally different simulation method, e.g. FEM, would be necessary to evaluate these satisfactory. Consequently, the measures 1a to 1d will not be further considered in this report. Still, the ideas suggested might be valuable for R&D Test Systems A/S in the future.

Within this project, reducing the stress on the insulation is deemed more feasible. However, with respect to the necessary simplification of the CB model, the counter measures proposed in approach 2b can not be assessed using the simulation developed in this project and are consequently not further discussed. Still, the previous discussion will be valuable for the future work of R&D Test Systems A/S, improving their design of the FRT Tester. Furthermore, some of the other proposed methods in item 2c also lead to a change in power factor of the current, e.g. by connecting a snubber circuit in parallel with the coil. Also, the snubber circuit will lower the risk of pre-strikes and restrikes due to the reduced rate of rise of voltage [18]. Thus, these methods may even more impactful, due the reduced probability of current chopping and other transient effects in reality.

Considering the concept of the snubber circuit, as introduced in item 2c, SA will not be discussed individually, but only as part of the snubber circuit. This is mainly because SA have already been incorporated into the setup by R&D Test Systems A/S and were not able to prevent discharges completely.

The mitigation of the OV by damping the oscillation using a tuned RC element does pose a promising solution. This approach can be simulated using the model developed in Chapter 3 and 4, considering its limitations and drawbacks. All options, attaching the RC element to a fixed winding section, to a separately added damper winding or in parallel with the entire coil, as well as the snubber circuit seem feasible at first glance. Thus, these options will be incorporated into the simulation and assessed in detail in the following sections of this chapter.

## 5.2 Tuned filter with separate damper winding

The damper winding (DW) is an additional, open turn added to the coil, which is only coupled to the coil by the means of magnetic and electric fields. Thus, it has no galvanic connection to the coil itself. The turn is closed through a tuned RC component and placed either as the innermost or outermost turn of the coil.

### 5.2.1 Parameter determination and modelling of damper winding

The inductance, resistance and capacitance are calculated analytically as described in Section 3.4.2. The DW only has a single turn and its parameters are part of the parameter matrices for the entire coil. Figure 5.2 presents the coil's schematic as implemented in PLECS. In the time domain simulation, the grid is connected to the second row of the vectorized component, leaving the terminals of the first component open. The added RC filter is then attached to these open terminals. Further information on the use of vectorized components in PLECS is presented on the developer's website [45] and in the program's manual [40]. In the Figure $n$ denotes the number of turns (lumped turns). Thus, the coil's inductance $L_{coil}$ is a [n x n] component, containing self and mutual inductances. $R_{coil}$ and $C_{coil}$ have the dimension [1 x n]. It has to be noted that the value $C_{coil}(n)$ is describing the capacitance from the outermost turn to the ground plane. It was estimated as the capacitance of two concentric rings. The distance between the rings is approximately the clearance from the coil to ground in the physical FRT setup.

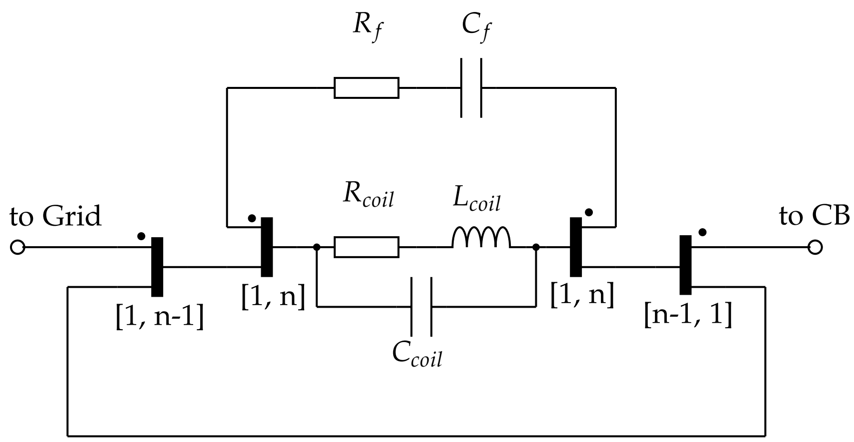


**Figure 5.2:** Sketch of coil implementation in PLECS with an additional damper winding as innermost turn.

As previously mentioned, the main idea is that the RC component acts as a high-pass filter to damp the oscillation in the coil after current chopping. Thus, it has to be tuned to the coil's resonance frequency $\omega_r = 6950\ Hz\ \cdot 2\pi$ with the inductance of the DW $L_{coil}(1,:) = L_{DW}$ in parallel to the filter. The resistor $R_f$ is then selected to match the impedance of the damper winding $|Z_{DW}|$ at resonance frequency, to dissipate the highest power:

$$C_f = 1/(\omega_r^2 \cdot L_{DW});\ R_f = |Z_{DW}| \tag{5.1}$$

In the simulations, the remaining parameters regarding chopping current value $i_c$, switching instances and other components remain unchanged. Details on those auxiliary components and simulation settings can be found in the beginning of Chapter 4. In the following section, the grid is connected to Tap 1 (0 % of winding) and the CB to tap 29 (100 % of winding). All other devices (i.e. second event switch and DUT) are disconnected.

### 5.2.2 Simulation results with damper winding

The Figure 5.3 shows the voltage across the entire coil (Channel 1 as in Figure 4.1) after current chopping. The Figure compares the simulated switching OV for the case without any counter measures (see Section 4.3) to the case where the DW is connected as the innermost turn or outermost turn. In both cases, the filter components were selected in similar manner.

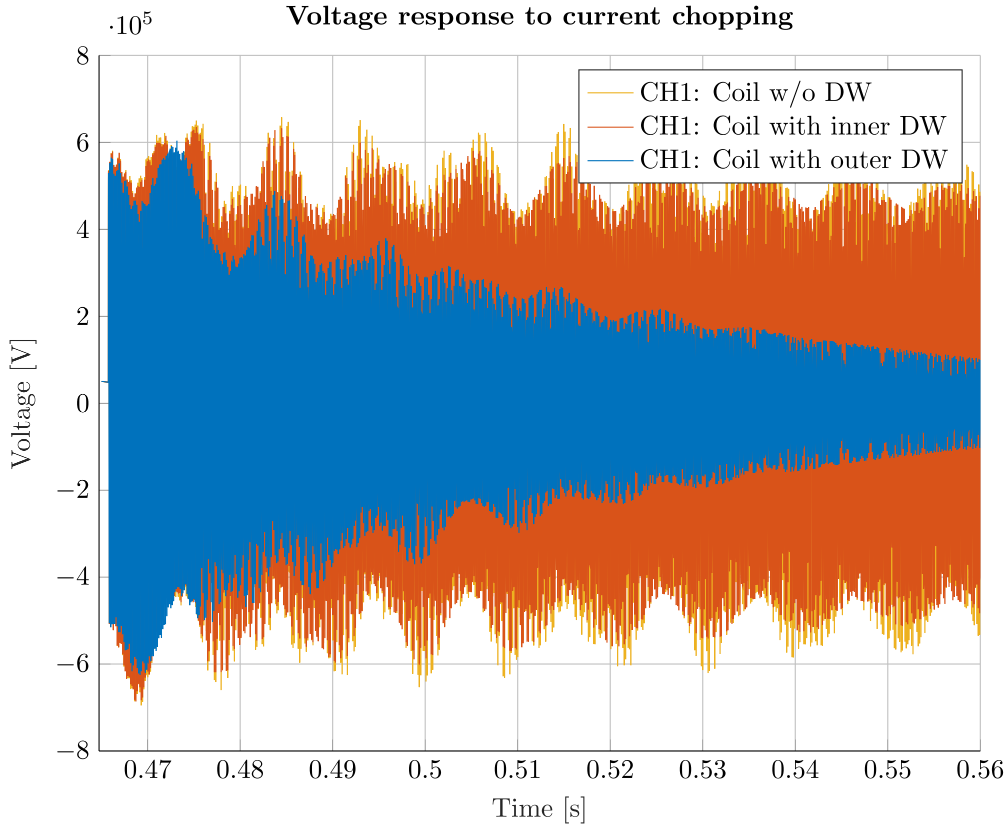


**Figure 5.3:** Switching overvoltage with and without damper winding

As evident from the Figure, especially the DW as the outermost turn damps the oscillation in the coil significantly faster than in the simulation without counter measures. However, the initial magnitude of the OV remains almost unchanged. The difference in the oscillation's decay is occurring due to the different electric and magnetic couplings of the two DW: For the DW as the outermost turn, the capacity between it and the coil's adjacent turn is significantly larger due to the turns' greater circumferences compared to the DW as the innermost turn.

From Literature [6], [7], it is evident that the surge breakdown voltage is, among other factors, dependent on the rate of rise of voltage, the duration for which the surge exceeds the stationary breakdown voltage, and statistical effects (e.g. presence of a starting electron). These factors generally lead to a higher breakdown voltage when a system is stressed by a transient voltage instead of a (quasi-) stationary voltage. However, the discharge process in gases is occurring within a time scale of a few tens of nanoseconds, depending on the previously mentioned factors.

The envelope of the switching OV in the case the DW is installed as the outermost turn has a time constant of approximately $\tau = 0.05\ s$. The frequency of the oscillation is approximately $f_r = 6.95\ kHz$ (first resonance frequency of coil). Considering these values and the significant magnitude in the first tens of milliseconds, this configuration can not be considered sufficient to mitigate the discharges observed at the coils. For the fast breakdown process the voltage decay is too slow. Obviously, the configuration with the DW as the innermost turn is even less effective.

## 5.3 Tuned filter in parallel to winding

As previously discussed, the RC component can also be attached to two existing taps, in parallel to a section of the coil or the entire coil. In the latter case, the RC element can be regarded as a snubber circuit if a SA is added in parallel to it.

### 5.3.1 Parameter determination and configuration of RC-Filter

The RC-element, consisting of $R_f$ and $C_f$, is added into the circuit as sketched in Figure 5.4. For the connection, two existing taps in the coil's outer section were chosen. The Tap configuration of two simulation runs and the selected values for the filter components are evident from table 5.1. The values for $C_f$ and $R_f$ were calculated as presented in Section 5.2.1, utilising the coil's parameters in parallel to the filter in the respective configuration.

| Description | Configuration (a) | Configuration (b) |
|---|---|---|
| Grid | Tap 1 (0 %) | Tap 1 |
| DUT | Tap 11 (35 %) | Tap 11 |
| EV 1 | Tap 29 (100 %) | Tap 29 |
| EV 2 | - | - |
| Filter IN | Tap 18 (55 %) | Tap 1 |
| Filter OUT | Tap 20 (60 %) | Tap 29 |
| $C_f$ [nF] | 1.849 | 0.258 |
| $R_f$ [Ω] | 767 | 724 |

**Table 5.1:** Configuration of RC-component in parallel with winding section

The tap configuration in (a) was chosen as presented, because these two taps span over the outer packs of the coil's middle segment (see Section 1.2). According to the fault analysis is Section 2.1, this region was subject to discharge incidents and thus seems to be significantly stressed. By connecting the RC-component in the

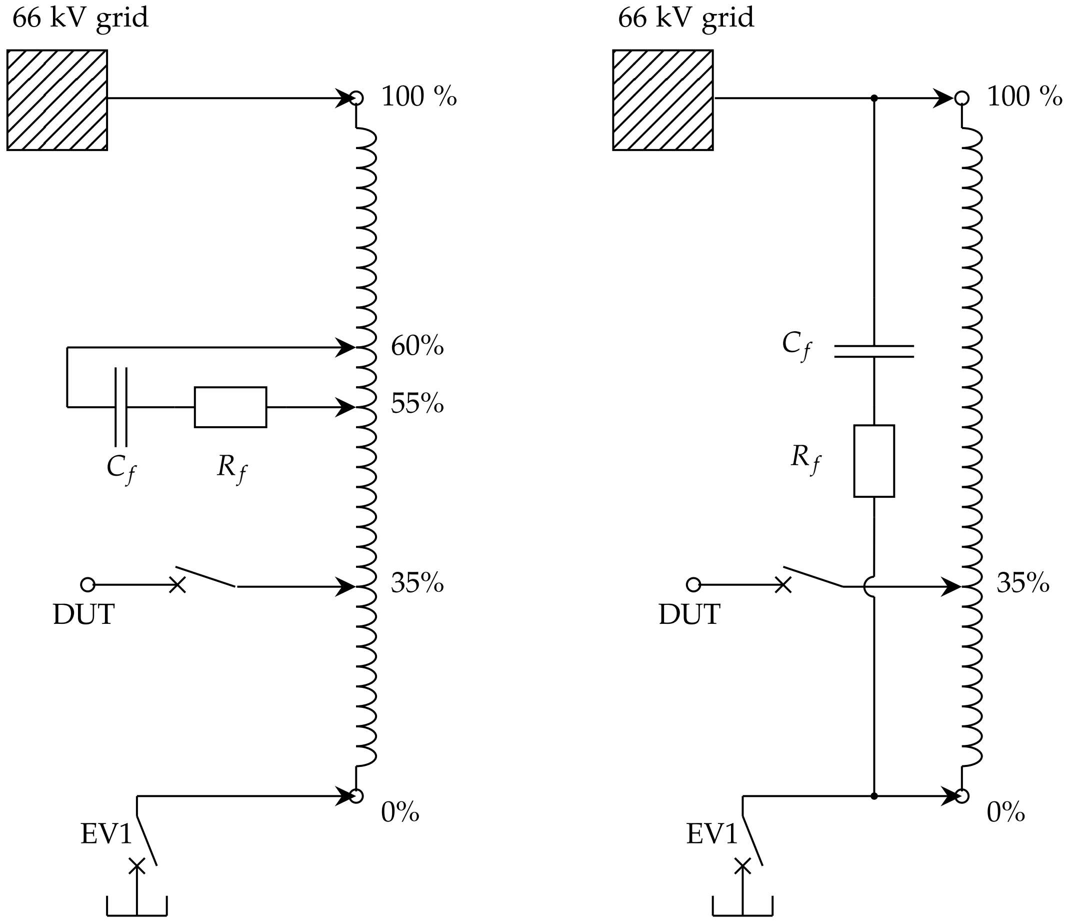


(a) Filter parallel to coil section

(b) Filter parallel to entire coil

**Figure 5.4:** Simplified single-line diagram of FRT tester with RC element in two configurations

vicinity of this coil section, the stress is projected to be alleviated in this particular region.

To achieve comparable results, the tap configuration of the different measurement channels remains unchanged. The different measurement channels are shown in figure 4.1. However, in the initial analysis of the simulation results, only channel 1, which is in parallel with the entire coil, is depicted.

### 5.3.2 Simulation results RC-Filter

The simulated OV to current chopping is presented in Figure 5.5, comparing the impact of connecting the RC component either to the a section only (a) or the entire coil (b).

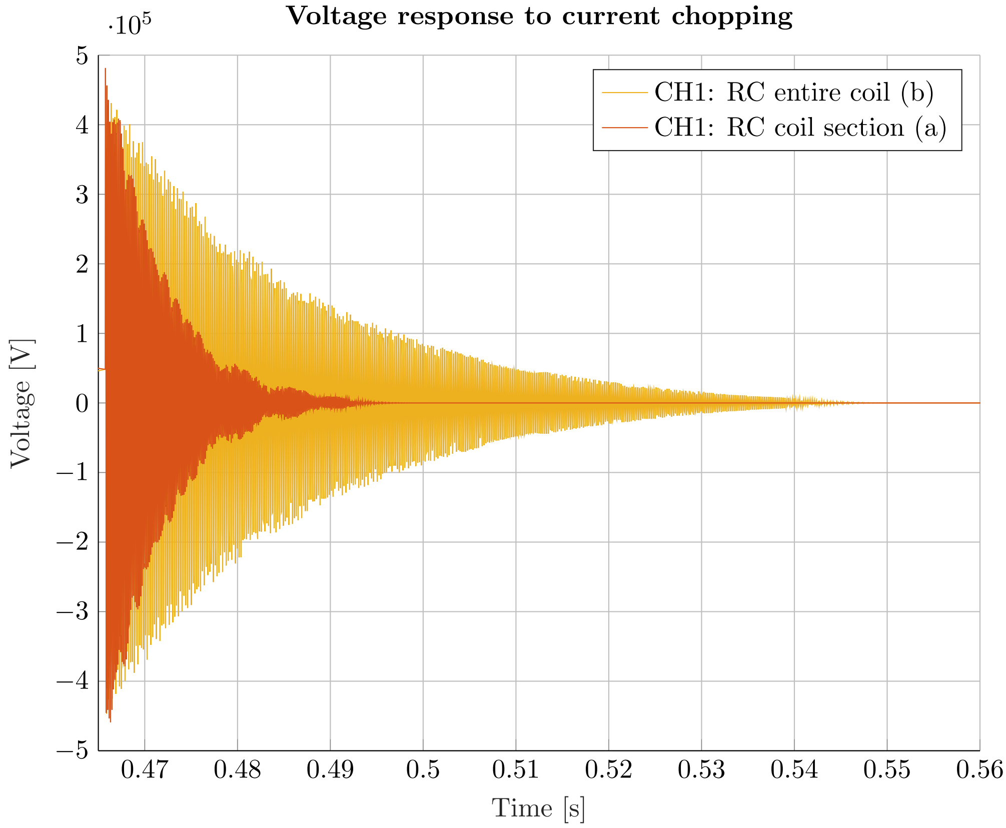


**Figure 5.5:** Switching overvoltage compared for RC-component configurations (a) and (b)

It is evident from the figure that neither of the mitigation approaches is capable of reducing the initial magnitude of the OV significantly. After current chopping, the voltage across the coil quickly rises to approximately 450 kV in both cases. The oscillating frequency in case (a) is approximately 6450 Hz and 5050 Hz in case (b). Both these frequencies do not correspond to the coil's resonance frequencies, due to the impact of the added RC components.

When the RC component is connected as specified in (a), the oscillation after the switching instant decays quickly, with a time constant of approximately $\tau = 0.006\ s$. This is one order of magnitude faster than the outer DW presented in Section 5.2. Again, this value has to be related to the time frame in which a gaseous discharge occurs: As previously elaborated, a breakdown in gas due to a voltage surge occurs within some tens of nanoseconds. Thus, also in this case, the rate of decay and the period duration of the oscillation are some orders of magnitude longer than the discharge process. Considering the simulated magnitude of the OV as well as its slow decay, it is very likely that both measures are not sufficient to protect the coil against discharges.

## 5.4 Snubber circuit in parallel with coil

As aforementioned, the RC component in parallel with the entire coil can be considered as part of a snubber circuit. In this case, however, the values for $R_f$ and $C_f$ have to be selected in a different manner.

### 5.4.1 Selection of snubber components

After the CB opened, the circuit depicted in Figure 5.5(b) can be considered a series RLC circuit, independent from the grid components, due to the open terminal. The coil is here simplified as an inductor only, disregarding its small capacitance and resistance. When current chopping occurs, a certain amount of energy, depending on the inductance and the instantaneous current value, will be stored in the inductor:

$$E_{coil} = 0.5 \cdot L \cdot i_c^2 = 0.5 \cdot 2.03\ H \cdot (7\ A)^2 \approx 49\ Ws \tag{5.2}$$

Because the current in the coil can not change instantaneously, this energy will be transferred to the capacitor and dissipated in the resistor. Disregarding the resistor in an initial approximation, one can select a capacitor value so that it can store the entire energy $E_{coil}$ when charged with the grid's maximum phase to ground peak voltage. This voltage is chosen because it is the coil's rated voltage.

$$C_f = 2 \cdot \frac{E_{coil}}{u_c^2} = 2 \cdot \frac{49\ Ws}{\left(72.5\ kV \cdot \sqrt{2/3}\right)^2} = 27.9\ nF \tag{5.3}$$

The resistor in the RC component can be chosen to critically damp the RLC circuit. Thereby, an underdamped condition and the resulting oscillations are avoided while the energy $E_{coil}$ is dissipated as fast as possible:

$$R_f = 2 \cdot \sqrt{\frac{L_{coil}}{C_f}} = 16.9\ k\Omega \tag{5.4}$$

These two values are incorporated into the circuit presented in Figure 5.5(b). The simulated result in Figure 5.6 presents the voltage across the coil (Ch1) and the voltage across the coil and the CB (Ch2) as previously sketched in Figure 4.1. In this application, the trace displayed as Ch1 is also the voltage drop across the RC snubber circuit as it is in parallel with the entire coil.

As evident from Figure 5.6, the coil is still exposed to a significant OV, shortly after the current is chopped. The magnitude of this voltage spike is approximately 120 kV. The transient voltage is very quickly damped afterwards, with only minor overshoot, indicating an effective measure to dissipate the energy stored in the coil.

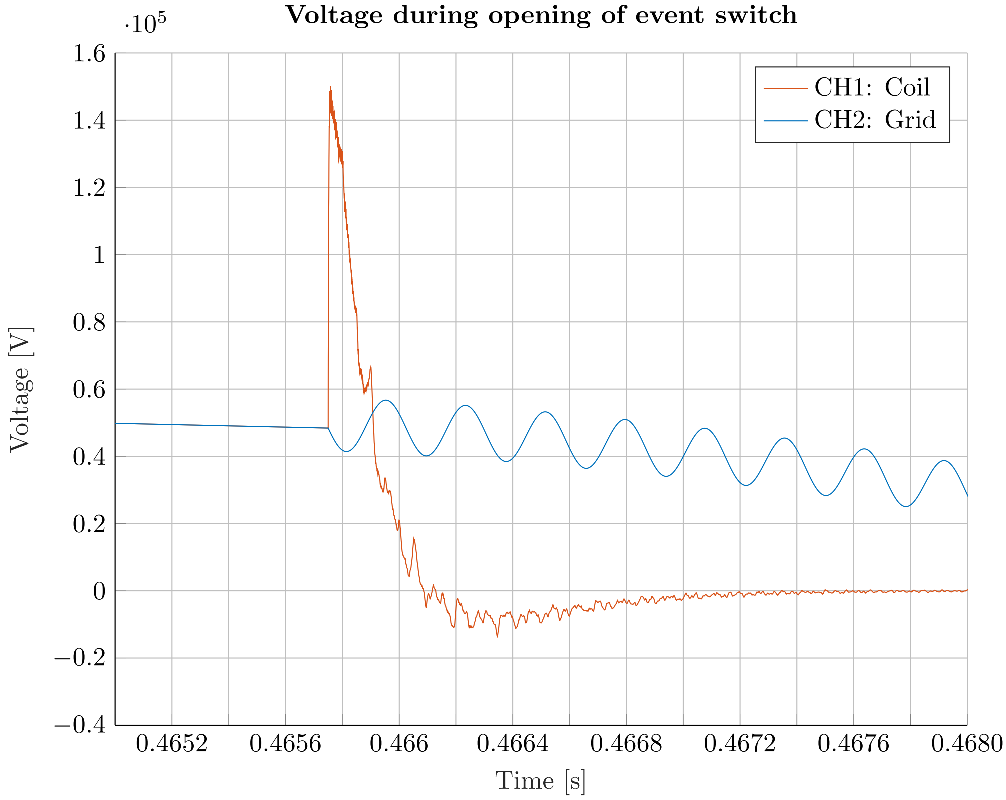


**Figure 5.6:** Switching overvoltage with snubber circuit, critically damped

Further investigation showed that the initial voltage spike is governed by the resistance and chopping current value: After current chopping, the coil's inductance can be regarded as a current source, which drives current into the snubber circuit to keep the current through itself continuous. This creates a current impulse with a very steep front, due to the almost immediate interruption of current through the CB. In the initial moments after current chopping, the capacitor can be considered as a short circuit due to the high frequency content of the steep current slope. Therefore, the resistor gives rise to a voltage drop depending on the chopping current and it's value:

$$u_R = R_f \cdot i_c = 16.9\ k\Omega \cdot 7\ A = 118.3\ kV \tag{5.5}$$

Thus, the resistor's value is a trade-off between damping the oscillation to dissipate the energy in the coil and giving rise to an initial OV which could damage the coil.

Further, since the RC component is connected in parallel to the coil, it will impose a leakage current $I_{snubber}$ around the coil. A smaller resistor and larger capacitor leads to a larger leakage current. Thus, the relation $|Z_{snubber}| >> |Z_{coil}|$

should be fulfilled for power frequency, to not interfere with the FRT Testing procedures. After internal discussion, it was decided that the relation

$$I_{snubber} \leq 0.01 \cdot I_{coil} \tag{5.6}$$

$$\frac{1}{\sqrt{R_f^2 + (1/\omega C_f)^2}} - \frac{0.01}{\omega L_{coil}} \leq 0 \tag{5.7}$$

should be fulfilled for power frequency. This condition is fulfilled when the impedance of the snubber circuit $|Z_{snubber}| \geq 100 \cdot |Z_{coil}|$ at 50 Hz.

Due to the energy exchange after current chopping, the resulting OV will also be dependent on the capacitor's value. The capacitance value does not impact the initial voltage spike but rather the oscillation afterwards. As seen in Figure 5.5, the coil is exposed to a significant OV if the selected capacitor is too small. In this figure, the initial voltage drop due to the resistor and the chopping current through it is not visible since the resistor's value was only 724 Ω. By inserting equation (5.2) into (5.3), the relation

$$u_C = \sqrt{\frac{L_{coil}}{C_f}} \cdot i_c \tag{5.8}$$

can be found. Because, the highly inductive current is chopped in the vicinity of the current's zero crossing, the voltage spike will be added on top of the grid's voltage around the peak voltage. This is visible in Figure 5.6. In the worst case, the voltage to which the coil is exposed is

$$u_{coil} = U_g \cdot \sqrt{\frac{2}{3}} + u_C + u_R = 72.5\ kV \cdot \sqrt{\frac{2}{3}} + i_c \cdot \left(\sqrt{\frac{L_{coil}}{C_f}} + R_f\right) \tag{5.9}$$

because the voltage drop across the snubber circuit is added on top of the grid's peak voltage. In this equation, the simplification, that all energy is transferred from the coil into the capacitor is made. In reality, the resistor will immediately begin damping the oscillation and dissipate energy. Thus, the equation (5.9) shows an idealised, worst case scenario. Assuming the values presented in Table 5.1 for the snubber circuit in configuration (b), the calculated OV using equation (5.9) is 658.2 kV for a chopping current of $i_c = 7\ A$. As evident from Figure 5.5, the simulated response does not quite reach this value due to the previously discussed reasons. Still, this illustrates that the equation yields a result on the safe side.

The discussion shows further that some level of OV has to be accepted for the coil. According to [41], citing standards by NEMA and ANSI, outdoor equipment in substations rated for 72.5 kV must be able to withstand a 10 second power frequency OV of 145 kV (2 p.u.). The equipment used in the FRT Tester within this project must comply with similar standards. Thus, by selecting a permissible

OV of 2 p.u., discharges should be avoided with sufficient margin as the insulation is generally stressed less when exposed to a short surge compared to a quasi-stationary OV [6], [7]. Thus, equation (5.9) can be rephrased as the condition

$$u_{coil} \leq 2 \cdot U_g \cdot \sqrt{\frac{2}{3}} \tag{5.10}$$

$$U_g \cdot \sqrt{\frac{2}{3}} \geq i_c \cdot \left( \sqrt{\frac{L_{coil}}{C_f}} + R_f \right) \tag{5.11}$$

to determine appropriate values for $C_f$ and $R_f$.

**Mathematical optimisation of snubber components**

Due to the complexity of the problem, it is convenient to use Matlab's optimisation toolbox [46] and the function 'fmincon()' to minimise the cost function (5.9) subject to the non-linear inequality constraint (5.6) of the leakage current. The theory of optimising such problems can be found for example in [47]. Both, the cost and the constraint function, are only dependent on the values $C_f$ and $R_f$. The expected OV is then the cost function when evaluated at the proposed values for $C_f$ and $R_f$. Furthermore, a boundary condition to avoid unrealistic capacitance values has been set.

$$C_f \leq 100\ \mu F \tag{5.12}$$

Within a few iterations, it became clear that the target of the maximum OV (5.10) being less than 2 p.u. can only be achieved if a higher leakage current is tolerated. Thus, the algorithm depicted in Figure 5.7 was developed to find a tolerable OV with the smallest possible leakage current. Thereby, obtaining a result within the boundaries set for the permissible OV is valued higher than staying within the specified range of the leakage current.

Generally, the problem could also be considered a multi-objective problem, when both, the OV and the leakage current shall be minimised. However, the leakage current has to be considered the less important objective: In many cases, the coil is only partly energised (e.g. as presented in Figure 1.1). In these cases, the coil's impedance is smaller. Thus, the leakage current through the snubber circuit is smaller as its impedance is relatively larger with respect to the coil section. Furthermore, it is the OV's magnitude which has to be minimised to ultimately allow a safe operation of the FRT Tester. The theory for solving multi-objective optimisation problems can be found in literature [47].

The solution was found within $k = 67$ iterations and is summarised in Table 5.2. Incorporating these values into the time domain simulation yields the results presented in section 5.4.2. As evident from the table, the algorithm has found a constrained solution, since the capacitance value matches the value set as boundary

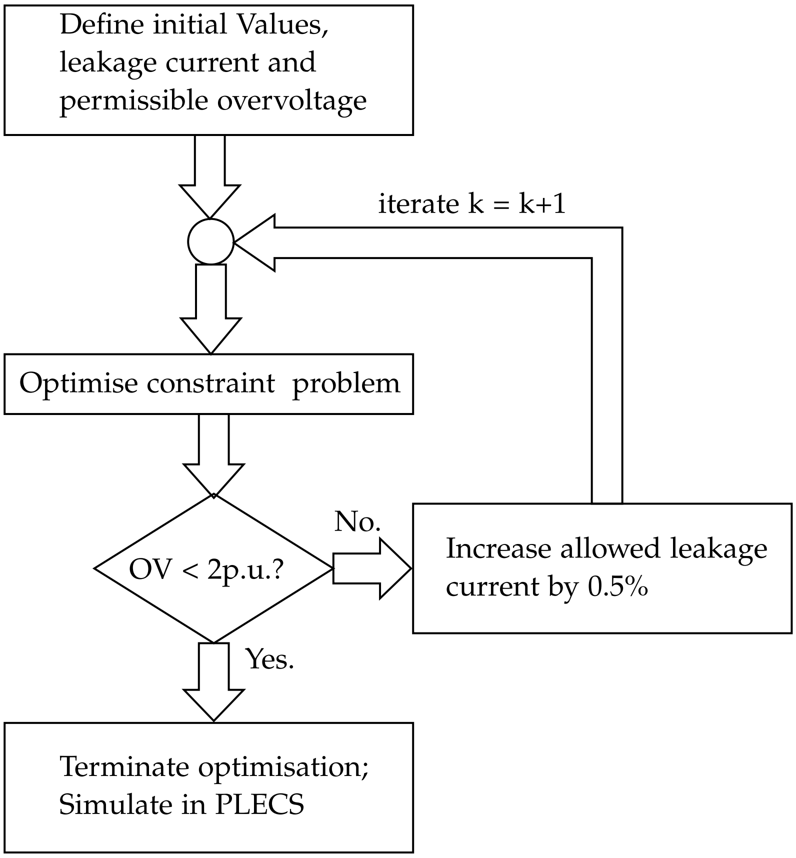


**Figure 5.7:** Flowchart for Optimisation process

in (5.12). Thus, a better solution can be found if this boundary is altered. The mathematically optimal solution, without the boundary (5.12) would be $C_f = 55.1\ kF$ and $R_f = 7.14\ n\Omega$ with a leakage current of 2.9%. However, these values for snubber components are technically unrealistic, illustrating the necessity to incorporate the boundary.

| **Description** | **Value** | **Unit** |
|---|---|---|
| Snubber Resistor $R_f$ | 8282 | $\Omega$ |
| Snubber Capacitor $C_f$ | 100 | $\mu F$ |
| Expected max. Voltage | 118.2 | kV |
| Leakage current | 7.7 | % |
| Number of iterations | 67 | - |

**Table 5.2:** Snubber data found through mathematical optimisation process.

### 5.4.2 Simulation results with snubber circuit

#### Energising entire coil with snubber circuit

The snubber circuit as specified in Table 5.2 was added to the time domain simulation. As previously, the entire coil is energised. Thus, the grid is connected at tap 1 (0% of winding) while the CB is connected to tap 29 (100%). The snubber circuit is also connected to these taps, as also presented in Figure 5.5(b). The observed OV is shown in Figure 5.8.

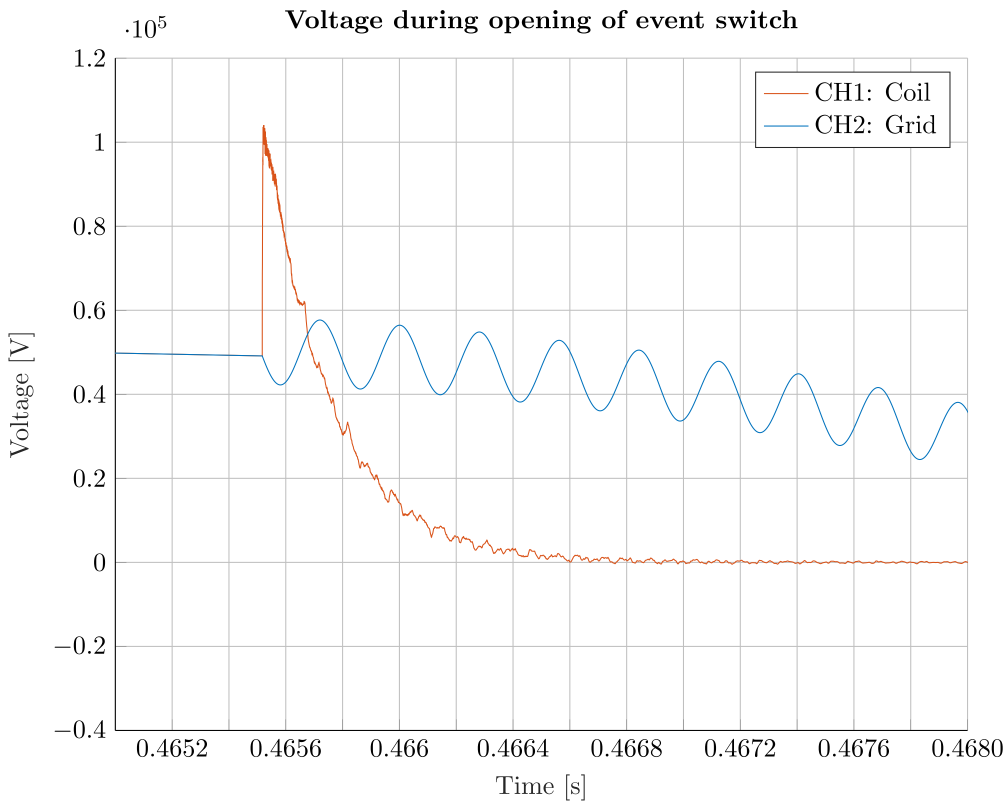


**Figure 5.8:** Switching overvoltage with snubber circuit, mathematically optimised

As seen, the voltage across the coil initially jumps to a value of 104 kV, which is equivalent to 1.75 p.u., considering the rated system voltage (72.5 kV) as the base value. After the initial spike, the voltage decays with a time constant of $\tau \approx 233\ \mu s$. The grid voltage (Ch2) shows a oscillation at the grid's resonant frequency of 3550 Hz as in the previous simulation in Chapter 4.

The observed result is in accordance with the previously specified maximum allowed OV of 145 kV (Equation (5.10)). Further, due to the simplification discussed (i.e. assuming all energy is transferred to the capacitor, disregarding the energy loss in the resistor), there is a significant margin between the calculated and simulated OV for the selected value of $i_c$. The approximate calculation is on the safe side, which is desirable from a design perspective.

Further, the turn to turn voltage inside the coil as a function of time and number of turns can be analysed. The turn to turn voltage would be measured if a voltmeter was attached between two adjacent turns. The cumulative sum of the measured value over the number of turns yields the measured voltage across the entire coil, presented in Figure 5.8.

Figure C.3 in Appendix C shows that the voltage drop per turn does not exceed 200 V after current chopping. This value can be considered low compared to the result observed without the snubber circuit in Figure C.2.

In both figures, however, it is visible that some coil sections are initially charged with a higher voltage than adjacent ones, showing as a peak in the initial microseconds after current chopping. The locations of those peaks correspond to the cooling ducts in the coil. The turn to turn capacity is several magnitudes smaller across a cooling duct than inside the uniform winding, due to the larger distance between the turns. Assuming the coil's magnetic energy is distributed uniformly across the entire coil in the instant of current chopping, these smaller capacitances are charged to a higher voltage. This could motivate improving the insulation design in the cooling ducts as previously mentioned in aspect 1c in the initial discussion.

These voltage oscillations in cooling duct capacitances can be considered internal or part-winding resonances as discussed in Section 2.5. While they are also visible in Figure C.2, their magnitude is small and thus overshadowed by the generally high turn to turn voltage. In general, the comparison of Figure C.3 and Figure C.2 further emphasises the effectiveness of the proposed counter measure: While some turn to turn voltages reached values of more than 800 V without counter measures, the snubber circuit reduces the turn to turn voltage to less than 200V and also leads to a much faster decay of the OV.

### Energising part of coil with snubber circuit

As previously mentioned, the coil is often only partly used in the FRT Tests. Thus, it is of great interest to analyse the effectiveness of the snubber circuit and the turn to turn voltage in this scenario. For the simulation, the most extreme case was chosen. According to internal information, the grid is connected to tap 1 (0% of winding) and the event switch to tap 11 (35%), utilising only 35% of the coil's winding. Due to the non-linearity of the coil's impedance (see Figure 2.1), this corresponds to less than one third of the impedance.

The simulated voltage across the utilised section, from the grid tap to the CB tap (Ch1), as well as the grid voltage (Ch2), and the voltage across the entire coil (Ch3) is presented in Figure 5.9. Thus, Ch3 is equal to the voltage drop across the snubber circuit.

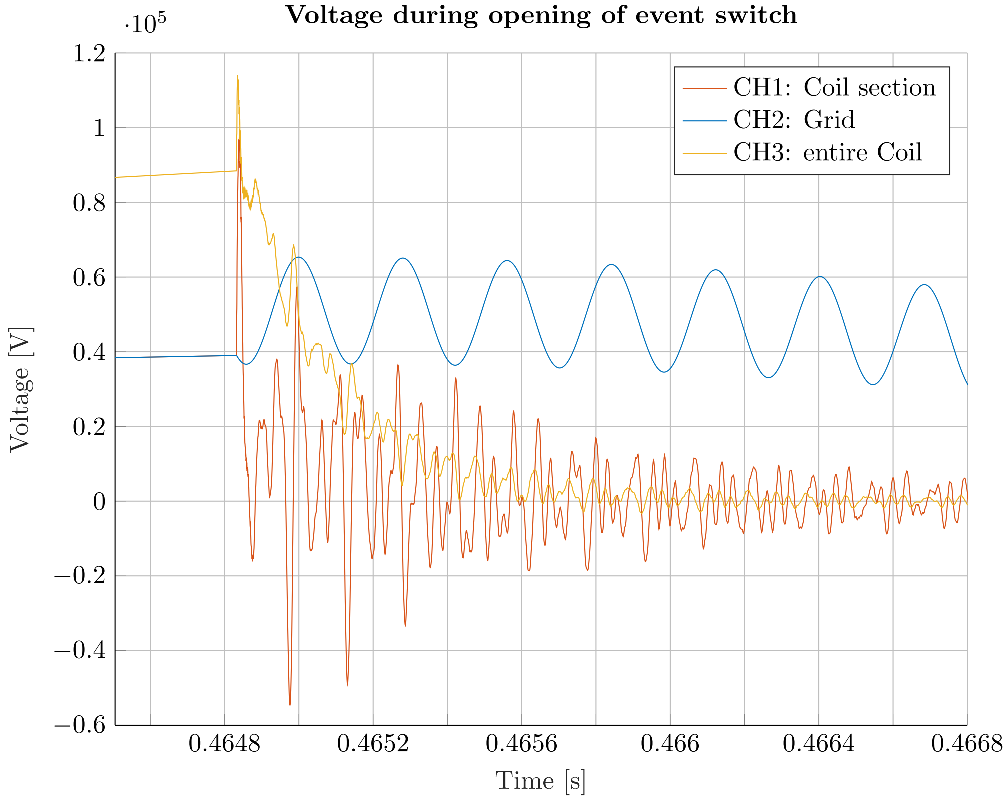


**Figure 5.9:** Switching overvoltage with snubber circuit and partly energised coil

As seen, the energy stored in the coil in the instance of current chopping is dissipated quickly. This matches the behaviour in the previous scenario, where the entire coil was energised. The maximum voltage magnitude across the entire coil reaches 113.3 kV and across the energised section only 96.6 kV. In the instant of switching, Ch3 shows a greater voltage magnitude than the grid voltage due to the transformer ratio between it and the energised coil section.

Also, Ch1, tracing the voltage across the energised section only, shows a distortion with relatively higher magnitude compared to Ch3. The reason is most likely that the RC component is mistuned when only considering a coil section since part of the coil are in series with the snubber circuit seen from Ch1's terminals. However, the simulation shows that also in this case, the snubber circuit provides an effective measure to decrease the OV's magnitude since the voltage across the coil does not exceed the specified limit of 2 p.u..

Furthermore, the turn to turn voltage in this scenario is depicted in Figure C.4. In the figure, the energised coil section corresponds to turn 1 to turn 411 (35% of winding). In this case, the simulated turn to turn voltage does not exceed 350 V. This value is larger than in the previous scenario. The reason is that, when energising a section of the coil only, the turn to turn voltage is at a higher value before the switching instance already.

It is visible in Figure C.4 in Appendix C that, again, the smaller capacitances across the cooling ducts give rise to a discontinuity in the voltage profile. In the energised section, these lead to a high frequency oscillation in the initial microseconds after current chopping. However, this oscillation decays quickly. It is interesting that the internal resonances of the cooling ducts are not excited in the unused part of the coil.

Although the turn to turn voltage is higher in this scenario compared to the previous one, it is unlikely that the observed voltage leads to a discharge. However, since the coil's true insulation strength is unknown, this remains an assumption. Still, it can be concluded that the snubber circuit with the parameters selected is capable of reducing the OV significantly, which also alleviates the stress on the turn to turn insulation.

### 5.4.3 Installation and component selection of snubber circuit

In general, the snubber circuit has to be installed as close as possible to the protected device (i.e. the coil). Otherwise, according to [44], the inductance between it and the device will make the snubber ineffective. SA would have to be deployed in similar fashion. Snubber circuits in transformer applications are often connected to the transformer's HV terminals inside the transformer housing or tank, to decrease the impedance as much as possible.

The components for the snubber circuit have to be chosen prudently. The resistor has to be chosen in accordance with the projected power dissipation. According to Table 5.2, the resistor will conduct 7.7% of the current through the coil in stationary operation, while the CB is closed. During voltage dip tests, this period can extend up to several minutes, according to internal information. When the entire coil is energised, the current through the resistor is largest since then the entire impedance of the coil is used. Thus, the maximum effective current through the resistor will be

$$I_R = 7.7\% \cdot \frac{72.5\ kV}{\sqrt{3} \cdot Z_{coil}} = 5.054\ A \tag{5.13}$$

Consequently, the resistor must be able to dissipate 211 kW in steady operation. A power surge during the switching instances does not have to be considered due to the resistors large thermal capacity. However, it is important that the resistor's design has a low inductance to provide a sufficiently low impedance path for the steep voltage surge. Steel grid resistors or thick film resistors as proposed in [44] could pose an adequate solution in this application. The fuse in the snubber circuit will delimit the energy intake in case the capacitor malfunctions (short circuit).

The capacitor used in the snubber circuit has to be able to be suitable for impulse and AC stresses. Generally, impulse voltages impose a high thermal stress on the capacitor's internal connections since the current inside it is proportional to the voltage slope. There are designated surge capacitors, offered by various manufacturers, which are a adequate choice for this application.

The selected values in Section 5.4.3 are for illustrative purposes only. The reason is that the chopping current value $i_c$, as evident from Equations (5.2) and (5.9), has a significant influence on the energy stored in the coil. Thereby it also determines the selected component values for the snubber circuit and the calculated OV. Thus, it is highly advisable to reevaluate the component values once a measurement of the chopping current or a more detailed simulation of the CB was performed.

Furthermore, as discussed initially, many snubber circuits also often incorporate a SA and a fuse. Both of these components are for protective measures only. Ideally, neither the SA nor the fuse would trigger during operation. However, it is still advisable to include these components. The fuse must be selected in accordance with the chosen capacitor and the permitted rated current.

To select an appropriate surge arrester, the previously discussed autotransformer effect has to be considered (see Figure 5.1). Therefore, it is not sufficient to base the SA's rated voltage on the system's phase-ground voltage only. Before selecting the component, the maximum voltage drop across the snubber circuit has to be evaluated prudently, considering the different tapping configurations. In this context, the SA's capability to dissipate the energy dissipated during these TOV has to be considered and can be a limiting factor. Afterwards, the arrester's protection levels for switching and lightning surges have to be matched to the systems withstand levels with sufficient margin. It has to be ensured the system's withstand levels are higher than the SA's protective levels, but that the permitted OV by the snubber circuit does not trigger the SA. The arrester can then finally be selected by also considering mechanical limitations as well as the necessary creeping distance for the foretasted pollution severity at site. Further and more detailed information can be found in a relevant buyer's guide [48].

It is noteworthy that the SA by itself would not fully protect the coil, as it is incapable of limiting the rate of rise of the transient voltage. Therefore, the turns closest to the CB terminals might be exposed to high OV, despite the installation of a SA.

## 5.5 Conclusion

This chapter introduced and discussed various counter measures to mitigate the discharges observed at the coil. Considering the measurement data available and the limitations of the computer simulation developed in Chapter 3 and 4, mitigating the OV through damping with a RC element was selected as the most promising approach. RC filters in different configurations were incorporated into the simulation and the respective results discussed. Among the selected options, a snubber circuit in parallel with the entire coil proved to be most effective.

However, there are some counter measures which could not be simulated, mainly due to the simplified CB model: the options proposed as item 2b in the initial discussion aim at reducing the probability of occurrence of current chopping by altering the current's power factor or exchanging the CB. The applicability of these methods can be assessed if the proposed solution proves to be not sufficient.

There is one aspect of the subber circuit's integration into the test setup which has not been analysed yet: The circuit's influence on the FRT testing procedure. As mentioned, the RC component will lead to a leakage current around the coil when the CB is closed. With the proposed method to select the RC component, this leakage current is kept as low as possible while reducing the OV to the permitted level. However, without knowing the actual chopping current value $i_c$, the final parameters of the snubber circuit can not be determined. If the snubber is projected to interfere with the FRT testing procedure, an alternative method should be selected or corrective measures have to be taken.

# Chapter 6

# Conclusion and Future Work

*This chapter briefly summarises and concludes the presented work. Afterwards an outlook on the suggested future work is given.*

## 6.1 Summary

The air-core reactor used in a 66 kV FRT test setup for wind turbines is prone to discharges in radial direction at the coil's side. These discharges are projected to delimit the coil's lifetime and pose a fire hazard. Thus, it is of great interest for the commissioner of the test setup, R&D Test Systems A/S, to analyse the root cause of these discharges and find effective methods to mitigate them in the future. The corresponding research question as well as the project's scope, methodology and limitations are presented in Chapter 1.

In Chapter 2, a more detailed description of the discharge incidents is presented. Afterwards, potential root causes are discussed and analysed. It was found that current chopping in the CB used as event switch is likely to occur. The reason is that the CB has a maximum breaking current is far beyond the magnitude of currents occurring in the setup. Due to the coil's inductance, the interrupted currents in the CB are inductive and of relatively small magnitude. This is known to pose the risk of current chopping, which can lead to tremendous OV. Furthermore, the OV can excite internal resonances in the coil, stressing the insulation in some sections particularly.

The coil's response to switching activity can be assessed in a computer model. In Chapter 3, different modelling approaches are discussed. Based on the discussion, the coil is modelled as an equivalent circuit with analytically calculated parameters for the inductance, resistance and capacitance of each turn. The model is validated in the frequency domain by comparing it to a SFRA measurement. To incorporate the coil model into a more resource demanding time-domain simulation, it is simplified by lumping turns together to reduce the number of circuit sections. The lumped model is again analysed in the frequency domain to assure its compliance with the coil's SFRA.

Chapter 4 initially introduces the auxiliary components in the time domain simulation, i.e. the CB and grid model. It is important to realise that the CB in this project had to be modelled as an ideal switch which opens at a defined chopping current value. This simplification had to be taken due to the limited data available. Afterwards, the coil's response to current chopping is assessed comprehensively. The coil gives rise to a significant OV with a magnitude of approximately 11 p.u. and a small rate of decay ($\tau = 0.42\ s$). The spatial voltage distribution in the coil is also analysed but the magnitude of internal oscillations are small compared to the overall OV. The magnitude of the OV is most likely violating the coil's insulation strength, leading to the discharges.

The previous Chapter 5 is dedicated to finding appropriate and effective counter measures against the discharges. Initially, an open discussion on various different approaches to mitigate the discharges is presented. There are multiple theoretically feasible methods. The most promising solution with respect to the model's limitations and effort to incorporate it in the FRT tester in reality is found in damping the oscillation after current chopping by a tuned RC filter or a snubber circuit. These two measures are added to the time-domain simulation in different configurations and are analysed. The most effective solution according to simulation results is the snubber circuit. A method to determine the component parameters based on mathematical optimisation is presented. The simulation results incorporating this snubber circuit are discussed comprehensively. The OV can be reduced to less than 2 p.u., depending on the snubber circuit values and the magnitude on the chopping current.

## 6.2 Conclusion

To conclude, the initial research question formulated in Chapter 1 can be answered by the following:

**According to the comprehensive discussion and root cause analysis carried out in Chapter 2 and considering the measurement results in Chapter 4, OV due to current chopping are the root cause for the discharges observed. Judging from the simulation results in Chapter 5, a snubber circuit with appropriately selected components is an effective solution to mitigate the OV. Alternative solutions to reduce the risk of current chopping, e.g. altering the current's power factor, were not analysed due to the model's limitations but also pose a promising approach on theory.**

Further, the initially formulated working questions can now be answered:

In Chapter 2 multiple potential causes for the discharges were initially presented. Among the presented causes, the transients introduced by switching activity and especially switching OV due to current chopping are the most likely root cause (see Section 2.4). In this context, the system of coil and CB has to be considered as a whole: Due to the physical process of arc quenching in the CB, the currents magnitude, power factor, and CB's properties (shape and material of contacts, insulation material and other) determine the likelihood of current chopping. Based on relevant literature and data provided by R&D Test Systems A/S, this effect is likely to occur because the CB is rated for breaking currents far beyond the currents occurring in the FRT tester.

The impact of current chopping can be analysed by a time-domain simulation, as concluded in the discussion in Chapter 3 and 4. For the simulation, the coil's parameters were calculated analytically, Section 3.4.2. The coil model's frequency response accurately represents the measured SFRA, especially for the first resonance point as seen in Figure 3.6. The CB is modelled as an ideal switch, breaking the current at a defined chopping current $i_c$. This model allows to quantify the OV, if the value $i_c$ is known (Section 4.1.2). Here, a major disconnection between model and reality can be identified: Due to the limited data available, $i_c$ could only be estimated and is most likely incorrect. Therefore, to assess the stress on the coil more accurately using the model developed, the accuracy of this value must be increased. This can be done by measurements at site to verify the selected $i_c$. The expected magnitude of OV would then also be justified.

The simulated voltage can also be visualised as a function of the number of turns as well (see Appendix C). While this yields the stress on the insulation system, with respect to the selected chopping current, its impact on the insulation remains unknown, due to the lack of comprehensive data available on the insulation's strength. An experimental assessment of insulation samples could shed light on the insulation's strength, allowing conclusions regarding the stress' impact. However, the comparison of the observed stress with standards on insulation coordination in substations permits to approximately identify an acceptable level of stress.

Various counter-measures against the discharges were presented in a comprehensive discussion in the beginning of Chapter 5. The discussion showed that multiple approaches are promising in theory. Some of those can also be implemented into the FRT test setup with reasonable effort:

1. Decrease the probability of current chopping by altering the current's power factor or exchanging the CB.

2. Improve the insulation's strength by applying varnish or resin in specific

spots.

3. Damp the oscillation in the coil after current chopping by a tuned RC filter or snubber circuit.

Due to the simple CB model, the impact of the mitigation methods 1 could only be discussed in theory and were thereafter not further analysed. However, they might prove to be an effective measure and could be implemented into the setup if the proposed measure is insufficient.

In similar fashion, improving the insulation strength in item 2 can also not be assessed in the simulation at hand. Due to many influencing factors, e.g. air-filled cavities in the resin, this method should be assessed experimentally in a laboratory. Furthermore, this measure's effectiveness will be highly dependent on the practical implementation at site, i.e. to which degree air-filled cavities are present in the resin or if delamination of the solid insulation and the aluminum foil conductor can be avoided.

The counter measures proposed as item 3 were all identified as feasible in theory. Thus, they were incorporated into the simulation in Sections 5.2, 5.3 and 5.4. The comparison of results showed however that only the snubber circuit is able to mitigate the OV significantly and was therefore analysed in more detail. The tuned RC elements in different configurations only decreased the oscillation's time constant, but do not lead to a significant reduction of the initial transient voltage. Those measures are thus considered insufficient.

As shown in Section 5.4, a snubber circuit provides an effective solution to reduce the transient OV and is the most effective among the methods assessed in the simulation. However, it's implementation is a trade-off between the magnitude of the OV and the leakage current, since the snubber circuit is an impedance in parallel with the coil (sketched in Figure 5.5(b)). In Section 5.4, a method to select the values for the RC components in the snubber circuit based on mathematical optimisation is proposed. The selection resolves around optimising a non-linear problem subject to a non-linear inequality constraint as evident from the cost function (5.9) and constraint (5.7). By selecting the components according to the algorithm presented in Figure 5.7, an optimised solution can be found. With the proposed values, the OV due to a chopping current $i_c = 7\ A$ is reduced from 11 p.u. (Fig. 4.7) to less than 2 p.u. (Fig. 5.8). The leakage current is 7.7 % of the coil's rated current in the worst case, when the coil's entire impedance is utilised. However, the selected component values are highly dependent on the chopping current value and must therefore be recalculated once the chopping current has been measured.

The suggested snubber circuit proved its effectiveness within the time-domain simulation by significantly reducing the OV and dissipating the energy stored in the coil after current chopping quickly. Furthermore, it is known from the theory on the operation of CB (see Section 2.4) that the snubber circuit can help to alleviate stress on the protected device by lowering the risk of restrikes and reignition. The reason is that it decreases the rate of rise of the TRV and thereby the CB is stressed less in the initial moments after arc quenching. However, as previously mentioned, this beneficial aspect of the counter-measure is not visible in the model due to the CB's simple representation. Due to this circumstance and the fact that $i_c = 7\ A$ is an rough estimation only, the method's effectiveness should be assessed experimentally.

## 6.3 Future work

### 6.3.1 Parameter determination and measurements

The most important aspect of the future work is to prudently analyse the snubber circuit's impact on the FRT testing procedures: It is imaginable that the leakage current through the RC component changes the residual voltage and X/R ratio seen by the DUT in the FRT testing application. To minimise the impact, the algorithm presented in Section 5.4 incorporates the leakage current as a constraint. It has to be assessed prudently, to which amount the leakage current can be tolerated. This detailed analysis has thus to be carried out by R&D Test Systems A/S in the future.

Furthermore, an aspect that has been mentioned multiple times is the necessity to carry out a comprehensive measurement campaign. Since current chopping was identified as the most likely root cause for the discharges in Chapter 2, this hypothesis should now be validated by a measurement at site. The measurements would also allow the quantification of the chopping current value, if the measurement's bandwidth is sufficiently high. As outlined in Section 2.4, the process of restrikes is governed by the thermal recovery of the insulation gas in the first few microseconds after current chopping. It may be challenging to measure the current with a sufficiently high bandwidth (> 1 MHz) to observe this effect. A work-around solution could be to measure the voltage across the CB to identify the phase angle at which the arc extinguishes. Knowing the current's power factor, the chopping current could then be calculated. In any case, since current chopping is subject to some intrinsic randomness, the test should be performed multiple times.

The measured value of $i_c$ is important to correctly determine the component values in the snubber circuit to lower the voltage to an acceptable level, as shown in Equation (5.9). The component values will also determine the leakage current and thereby the resistor's power rating and the necessary rated voltage for the capacitor.

### 6.3.2 Alternative mitigation methods

As previously outlined, there is a theoretically promising mitigation approach which was dismissed due to limitations in the time-domain simulation: Reducing the probability of current chopping by altering the current's power factor or exchanging the CB. Since these methods are effective in theory, they should be studied in more detail. With regard to exchanging the CB, it is probably most efficient to contact relevant manufacturers, provide them with a description of the problem and the expected current values to inquire a suggested product. Potentially an alternative CB technology could be a solution as well. To assess the effectiveness of altering the current's power factor to reduce the probability of current chopping, the CB would need to be modelled with greater detail. Some models are suggested and discussed in [17]. A validated and more detailed CB model could also be useful to estimate the chopping current value with sufficient accuracy without a physical measurement.

An alternative mitigation approach which has not been discussed yet is alternative connection schemes for the snubber circuit: In the approach suggested in Chapter 5, the snubber circuit would be connected from 0% to 100% of the coil's winding regardless of the tap configuration of grid and event switch. Potentially, the snubber circuit could also be connected between the grid and the event switch tap, i.e. only in parallel with the utilised coil section (common winding of auto-transformer). In that case, the circuit's parameters would need to be selected according to the worst case scenario, i.e. largest energy stored in the coil. Furthermore, it has to be assessed if it is sufficient to only equip one of the event switches with a snubber circuit and how it should be connected in case both event switches are used (e.g. in double-dip fault tests). Whether this solution proves to be more effective compared to the one presented in Chapter 5 can be assessed using the simulation developed in this project without any major changes. In this case, again, the impact of the snubber circuit on the FRT testing procedure has to be analysed prudently.

# Bibliography


[1] R. Teodorescu, M. Liserre, P. Rodriguez, and F. Blaabjerg, *Grid converters for photovoltaic and wind power systems*, ser. Wiley - IEEE. Chichester, West Sussex: Wiley, 2011, ISBN: 9786613813473.

[2] M. Altın, Ö. Göksu, R. Teodorescu, P. Rodriguez, B.-B. Jensen, and L. Helle, "Overview of recent grid codes for wind power integration," pp. 1152–1160, 2010. DOI: `10.1109/OPTIM.2010.5510521`.

[3] M. Tsili and S. Papathanassiou, "A review of grid code technical requirements for wind farms," *IET renewable power generation*, vol. 3, no. 3, pp. 308–332, 2009. DOI: `10.1049/iet-rpg.2008.0070`.

[4] B. Rona and Ö. Güler, "Power system integration of wind farms and analysis of grid code requirements," *Renewable sustainable energy reviews*, vol. 49, pp. 100–107, 2015. DOI: `10.1016/j.rser.2015.04.085`.

[5] R&D Test Systems A/S, *R&D Engineering Solutions and Consulting*, Last accessed 14.04.2022, 2022. [Online]. Available: `https://www.rd-as.com/`.

[6] E. Kuffel, W. S. Zaengl, and J. Kuffel, *High Voltage Engineering Fundamentals*. Newnes, 2000, ISBN: 0-750-63634-3.

[7] A. Küchler, *Hochspannungstechnik*. Springer, 2017, ISBN: 978-3-662-54700-7.

[8] M. Faramarzi Palangar and M. Mirzaie, "Mathematical modeling of critical parameters on the polluted ceramic insulators under ac voltage: Based on experimental tests," *Arabian Journal for Science and Engineering*, vol. 41, no. 9, pp. 3501–3510, 2016. DOI: `10.1007/s13369-016-2098-2`.

[9] M. T. Gencoglu and M. Cebeci, "Computation of ac flashover voltage of polluted hv insulators using a dynamic arc model," *European transactions on electrical power*, vol. 19, no. 5, pp. 689–701, 2009. DOI: `10.1002/etep.249`.

[10] P. Ghosh and N. Chatterjee, "Arc propagation over electrolytic surfaces under power frequency voltage," *IEEE Transactions on Dielectrics and Electrical Insulation*, vol. 3, no. 4, pp. 529–536, 1996. DOI: `10.1109/94.536732`.

[11] X. Zhang, J. Zhu, S. Bu, Q. Li, V. J. Terzija, and S. M. Rowland, "The development of low-current surface arcs under clean and salt-fog conditions in electricity distribution networks," *IEEE Access*, vol. 6, pp. 15 835–15 843, 2018. DOI: 10.1109/ACCESS.2018.2806885.

[12] N. Dhahbi-Megriche and A. Beroual, "Time – frequency analyses of leakage current waveforms of high voltage insulators in uniform and non-uniform polluted conditions," *IET Science, Measurement and Technology*, vol. 9, Jul. 2015. DOI: 10.1049/iet-smt.2015.0116.

[13] M. E. A. Slama and A. Beroual, "Flashover discharges dynamic with continuous and discontinuous pollution layer under lightning impulse stress," *Electrical Engineering*, vol. 103, no. 6, pp. 2887–2895, 2021, ISSN: 1432-0487. DOI: 10.1007/s00202-021-01258-w.

[14] M. A. Douar, A. Beroual, and X. Souche, "Creeping discharges features propagating in air at atmospheric pressure on various materials under positive lightning impulse voltage – part 1: Noise suppression using the discrete wavelet transform approach," *IET Generation, Transmission & Distribution*, vol. 12, no. 6, pp. 1417–1428, 2018. DOI: 10.1049/iet-gtd.2017.1092.

[15] A. Douar, A. Beroual, and X. Souche, "Study of creeping discharges features propagating in air at atmospheric pressure on various materials under positive lightning impulse voltage, part 2: Modeling and computation of discharges parameters," *IET Generation, Transmission & Distribution*, vol. 12, Sep. 2017. DOI: 10.1049/iet-gtd.2017.1112.

[16] C. L. Bak and F. F. da Silva, *Electromagnetic Transient in Power Cables*. Springer, 2013, ISBN: 978-1-4471-5236-1.

[17] J. Martinez-Velasco and F. Gonzalez-Molina, *Power Systems Transients: Parameter determination*. CRC Press, 2010, ISBN: 9781315218984. DOI: 10.1201/9781420065305.

[18] ABB, "Medium voltage switching devices: Technologies and applications," *ABB Technical Application papers*, no. 26, 2018.

[19] W. J. McNutt, T. J. Blalock, and R. A. Hinton, "Response of transformer windings to system transient voltages," *IEEE Transactions on Power Apparatus and Systems*, vol. PAS-93, no. 2, 1974. DOI: 10.1109/TPAS.1974.293992.

[20] H. Margolis, J. Phelps, A. Carlomagno, and A. McElroy, "Experience with part-winding resonance in ehv auto-transformers: Diagnosis and corrective measures," *IEEE Transactions on Power Apparatus and Systems*, vol. 94, no. 4, pp. 1294–1300, 1975. DOI: 10.1109/T-PAS.1975.31967.

[21] S. Fujita, N. Hosokawa, and Y. Shibuya, "Experimental investigation of high frequency voltage oscillation in transformer windings," *IEEE Transactions on Power Delivery*, vol. 13, no. 4, 1998. DOI: 10.1109/61.714485.

[22] A. De, A. Chakrabarti, and P. Hazra, “Resonant overvoltages produced in EHV transformer windings due to power system transients,” *Proceedings of the IEEE INDICON 2004. First India Annual Conference, 2004.*, 2004. DOI: 10.1109/INDICO.2004.1497709.

[23] T. Abdulahović and T. Thiringer, “Voltage stress in a transformer winding during very fast transients caused by breaker closing event,” *IEEE Transactions on Power Delivery*, vol. 29, no. 4, 2014. DOI: 10.1109/TPWRD.2013.2294379.

[24] M. Babaei and A. Abu-Siada, “Preventing transformer internal resonance under very fast transient overvoltage using rc surge suppressor,” *IEEE Transactions on Dielectrics and Electrical Insulation*, vol. 24, no. 2, 2017. DOI: 10.1109/TDEI.2017.006422.

[25] G. B. Shampa De Abhinandan De, “Self-capacitance grading approach to suppress winding resonance in ehv transformers under oscillatory terminal disturbances,” *High Voltage*, vol. 3, no. 4, 2018. DOI: 10.1049/hve.2018.5028.

[26] ——, “Development of a new multi-graded winding to alleviate resonant characteristic of EHV transformers,” *IET Generation, Transmission and Distribution*, vol. 14, no. 21, 2020. DOI: 10.1049/iet-gtd.2020.0983.

[27] L. Papula, *Mathematische Formelsammlung für Ingenieure und Naturwissenschaftler*. Vieweg+Teubner, 2009, ISBN: 978-3-8348-0757-1.

[28] Y. Shibuya, S. Fujita, and E. Tamaki, “Analysis of very fast transients in transformer,” *Generation, Transmission and Distribution, IEEE Proceedings-*, vol. 148, Oct. 2001. DOI: 10.1049/ip-gtd:20010504.

[29] A. Shintemirov, W. Tang, and Q. Wu, “A hybrid winding model of disc-type power transformers for frequency response analysis,” *IEEE Transactions on Power Delivery*, vol. 24, Apr. 2009. DOI: 10.1109/TPWRD.2008.2007028.

[30] D. Meeker, *Finite element method magnetics*, Last accessed 06.04.2022, 2022. [Online]. Available: https://www.femm.info/wiki/HomePage.

[31] F. Grover, *Inductance calculations: working formulas and tables*. Dover Publications, 2004, ISBN: 0486495779.

[32] S. Rohe, “Investigation of the accuracy of grover’s method when solving for the mutual inductance of two single-layer coaxial coils,” Master Thesis, University of Missouri-Columbia, 2005.

[33] T. H. Fawzi and P. E. Burke, “The accurate computation of self and mutual inductances of circular coils,” *IEEE Transactions on Power Apparatus and Systems*, vol. PAS-97, no. 2, pp. 464–468, 1978. DOI: 10.1109/TPAS.1978.354506.

[34] W. H. Hayt, *Engineering electromagnetics*, 8 ed. Mcgraw hill higher education, 2012, ISBN: 9780071089012.

[35] W. A. Davis, *Radio Frequency Circuit Design.* 2. ed., ser. Wiley Series in Microwave and Optical Engineering. Wiley, 2011, ISBN: 9780470575079.

[36] H. E. Abdelbagi, "Skin and proximity effects in two parallel plates," Master Thesis, Wright State University, 2008.

[37] C. Portela, S. Morais, and J. Teixeira, "Circuit-breaker behaviour in reactor switching: Applicability and limitations of the concept of chopping number," *IEEE transactions on power delivery*, vol. 3, no. 3, pp. 1009–1021, 1988. DOI: 10.1109/61.193881.

[38] T. Chmielewski, P. Oramus, M. Szewczyk, T. Kuczek, and W. Piasecki, "Circuit breaker models for simulations of short-circuit current breaking and slow-front overvoltages in hv systems," *Electric Power Systems Research*, vol. 143, pp. 174–181, 2017. DOI: https://doi.org/10.1016/j.epsr.2016.10.046.

[39] G. F. Moore, *Electric cables handbook.* 3. ed. Oxford: Blackwell Science, 1997, ISBN: 0632040750.

[40] Plexim GmbH, *PLECS User Manual, Version 4.6.5*, Last accessed 02.05.2022, 2022. [Online]. Available: https://www.plexim.com/download/documentation.

[41] A. R. Hileman, *Insulation Coordination for Power Systems*, 1st ed. CRC Press, 1999, ISBN: 0824799577.

[42] M. Seeger, R. Smeets, J. Yan, *et al.*, "Recent trends in development of high voltage circuit breakers with sf6 alternative gases," *PLASMA PHYSICS AND TECHNOLOGY*, vol. 4, no. 1, pp. 8–12, 2017, ISSN: 2336-2626.

[43] D. D. Shipp, T. J. Dionise, V. Lorch, and B. G. MacFarlane, "Transformer failure due to circuit-breaker-induced switching transients," *IEEE Transactions on Industry Applications*, vol. 47, no. 2, pp. 707–718, 2011. DOI: 10.1109/TIA.2010.2101996.

[44] P. E. Sutherland, M. E. Valdes, and G. H. Fox, "Snubber design for transformer protection," *IEEE Transactions on Industry Applications*, vol. 52, no. 1, pp. 692–700, 2016. DOI: 10.1109/TIA.2015.2473137.

[45] Plexim GmbH, *PLECS: Implicit Model Vectorization*, Last accessed 02.05.2022, 2022. [Online]. Available: https://www.plexim.com/content/plecs-vectorization-components.

[46] The MathWorks Inc., *Optimization Toolbox*, Last accessed 21.05.2022, 2022. [Online]. Available: https://se.mathworks.com/products/optimization.html.

[47] J. Arora, *Introduction to Optimum Design.* Academic Press, 2004, ISBN: 0120641550.

[48] Hitachi Energy, *Surge Arrester silicone-housed PEXLIM*, Last accessed 23.05.2022, 2022. [Online]. Available: https://www.hitachienergy.com/de/de/offering/product-and-system/surge-arresters/high-voltage-surge-arresters/silicone-housed-surge-arrester-pexlim.

# Appendix A

# Coil's data sheet

*Due to regulations on the confidentiality of R&D Test Systems A/S' intellectual properties, the information in this appendix had to be omitted in the public version of this report.*

| Parameter | Value | Unit |
|---|---|---|
| Inductance | | H |
| Impedance (50 Hz) | | Ω |
| Resistance (DC) | | mΩ |
| Rated voltage | 72.5 | kV |
| Rated current | | A |
| Short circuit current (AC, 1 sec) | | kA |
| Maximum peak current | | kA |
| Winding cross-section | | mm |
| Insulation cross-section | | mm |
| Insulation material | | |
| Breakdown strength insulation | | kV/mm |
| Number of turns | 1260 | |
| Protection class | IP00 | |

**Table A.1:** Air-core reactor's technical data (RMS-Values)

| Parameter | Value | Unit |
|---|---|---|
| Rated current | 3150 | A |
| Rated voltage | | kV |
| Maximum breaking current | 40 | kA |
| Closing time | | ms |
| Opening time | | ms |

**Table A.2:** Circuit breaker's technical data

# Appendix B

# Grover's method

*In this Appendix, the principle of Grover's method to calculate the mutual inductance of two concentric, single-layer coils is summarised.*

The sketch in Figure B.1 presents the geometric parameters on which Grover's calculations are based. The description of Grover's method can also be found in literature [31], [32].

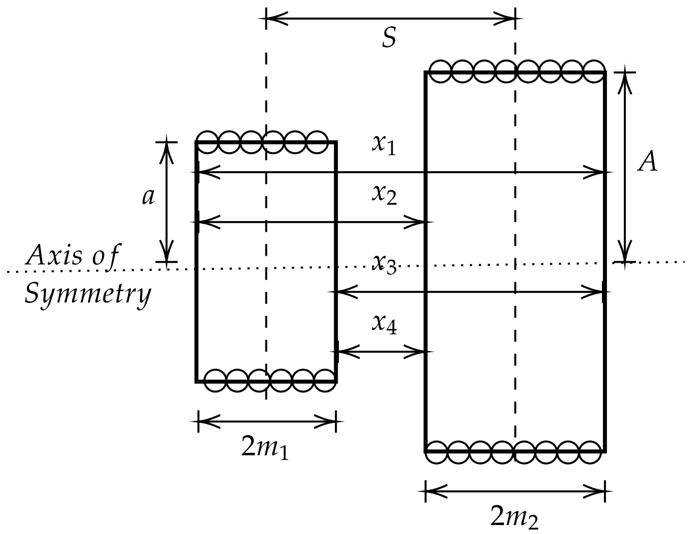


**Figure B.1:** Sketch of geometric parameters for two concentric coils, as presented in [32]

In the context of this project, the coaxial coils will have the same length $2m_1 = 2m_2 = 2m$ and are aligned ($S = 0$). Still, it is worth examining a general arrangement, to understand Grover's method fully. Expressions for $x_1 ... x_4$ using $m_1, m_2$ and $S$ can be found based on the sketch provided. These distances then correspond to the four main diagonals, as shown in (B.1). It is further imperative that

$A > a$ for the coils' radii.

$$\begin{aligned} r_1 &= \sqrt{A^2 + x_1^2};\ r_2 = \sqrt{A^2 + x_2^2} \\ r_3 &= \sqrt{A^2 + x_3^2};\ r_4 = \sqrt{A^2 + x_4^2} \end{aligned} \tag{B.1}$$

The mutual inductance of two single-layer coaxial coils is described by Grover in the following formula, using the expressions presented for diagonals above [31], [32]:

$$M = \mu_0 \cdot \pi \cdot a^2 n_1 n_2 \cdot (r_1 B_1 - r_2 B_2 - r_3 B_3 + r_4 B_4) \tag{B.2}$$

In equation (B.2), the winding density (number of turns divided by coil's length $2m$) is denoted as $n_1$ and $n_2$ for the coils with radius $a$ and $A$ respectively. The constant $\mu_0 = 4\pi \cdot 10^{-7}\ Vs/Am$ is the permeability of vacuum and $B_n$ are constants dependent on the geometric parameters $\rho_n$ and $\alpha$. The latter are used to determine $B_n$ in the tables B.1 and B.2 provided by Grover [31] and cited by Rohe [32]. These references further provide an auxiliary table for large values of $\rho_n$ and $\alpha$, increasing the accuracy of interpolation as $B_n$ changes rapidly in that parametric region.

$$\rho_n^2 = \frac{A^2}{r_n^2};\ \alpha = \frac{a}{A} \tag{B.3}$$

Using $B_n$ and the other geometric parameters, the mutual inductance $M$ can be calculated, according to Formula (B.2).

In the special case in this project, the Formula may be simplified to (B.4), since the coils are aligned, consist only of a single turn and have the same length $2m$.

$$M = \mu_0 \cdot \pi \cdot (\frac{a}{2m})^2 \cdot (r_1 B_1 - A B_2) \tag{B.4}$$

| $\alpha$ | $\rho^2 = 1$ | 0.95 | 0.9 | 0.85 | 0.8 | 0.75 | 0.7 | 0.65 | 0.6 | 0.55 | $\rho^2 = 0.5$ | $\alpha$ |
|---|---|---|---|---|---|---|---|---|---|---|---|---|
| 1 | 0.84833 | 0.87727 | 0.89552 | 0.9102 | 0.92264 | 0.93345 | 0.94298 | 0.95144 | 0.959 | 0.96576 | 0.9718 | 1 |
| 0.95 | 0.86783 | 0.88982 | 0.90561 | 0.91859 | 0.92971 | 0.93944 | 0.94805 | 0.95573 | 0.96261 | 0.96877 | 0.97428 | 0.95 |
| 0.9 | 0.88418 | 0.90175 | 0.91531 | 0.92666 | 0.93655 | 0.94524 | 0.95298 | 0.9599 | 0.96612 | 0.97169 | 0.97668 | 0.9 |
| 0.85 | 0.8987 | 0.91296 | 0.92456 | 0.93444 | 0.94314 | 0.95085 | 0.95774 | 0.96393 | 0.96951 | 0.97452 | 0.97901 | 0.85 |
| 0.8 | 0.91176 | 0.92344 | 0.93329 | 0.94185 | 0.94944 | 0.95622 | 0.96231 | 0.96781 | 0.97276 | 0.97723 | 0.98124 | 0.8 |
| 0.75 | 0.92356 | 0.93318 | 0.9415 | 0.94885 | 0.95542 | 0.96132 | 0.96668 | 0.97151 | 0.97588 | 0.97983 | 0.98338 | 0.75 |
| 0.7 | 0.93426 | 0.94217 | 0.94917 | 0.95543 | 0.96107 | 0.96618 | 0.97082 | 0.97503 | 0.97884 | 0.9823 | 0.98541 | 0.7 |
| 0.65 | 0.94394 | 0.95045 | 0.95629 | 0.96157 | 0.96637 | 0.97074 | 0.97472 | 0.97835 | 0.98164 | 0.98464 | 0.98732 | 0.65 |
| 0.6 | 0.9527 | 0.95803 | 0.96286 | 0.96727 | 0.9713 | 0.97499 | 0.97837 | 0.98146 | 0.98427 | 0.98683 | 0.98913 | 0.6 |
| 0.55 | 0.9606 | 0.96492 | 0.96888 | 0.97252 | 0.97586 | 0.97894 | 0.98176 | 0.98435 | 0.98672 | 0.98887 | 0.99082 | 0.55 |
| 0.5 | 0.96769 | 0.97115 | 0.97434 | 0.9773 | 0.98003 | 0.98256 | 0.98488 | 0.98702 | 0.98897 | 0.99076 | 0.99237 | 0.5 |
| 0.45 | 0.974 | 0.97673 | 0.97927 | 0.98163 | 0.98382 | 0.98584 | 0.98772 | 0.98945 | 0.99103 | 0.99248 | 0.99379 | 0.45 |
| 0.4 | 0.97958 | 0.98169 | 0.98366 | 0.9855 | 0.98721 | 0.9888 | 0.99028 | 0.99164 | 0.99289 | 0.99404 | 0.99508 | 0.4 |
| 0.35 | 0.98444 | 0.98603 | 0.98751 | 0.9889 | 0.9902 | 0.99142 | 0.99254 | 0.99358 | 0.99454 | 0.99542 | 0.99622 | 0.35 |
| 0.3 | 0.98862 | 0.98976 | 0.99084 | 0.99186 | 0.9928 | 0.99369 | 0.99451 | 0.99527 | 0.99598 | 0.99662 | 0.99721 | 0.3 |
| 0.25 | 0.99212 | 0.99291 | 0.99365 | 0.99435 | 0.995 | 0.99561 | 0.99618 | 0.99671 | 0.9972 | 0.99765 | 0.99806 | 0.25 |
| 0.2 | 0.99498 | 0.99547 | 0.99594 | 0.99638 | 0.9968 | 0.99719 | 0.99755 | 0.99789 | 0.99821 | 0.99849 | 0.99875 | 0.2 |
| 0.15 | 0.99718 | 0.99746 | 0.99772 | 0.99797 | 0.9982 | 0.99842 | 0.99862 | 0.99881 | 0.99899 | 0.99915 | 0.9993 | 0.15 |
| 0.1 | 0.99875 | 0.99887 | 0.99899 | 0.9991 | 0.9992 | 0.9993 | 0.99939 | 0.99947 | 0.99955 | 0.99962 | 0.99969 | 0.1 |
| 0.05 | 0.99969 | 0.99972 | 0.99975 | 0.99977 | 0.9998 | 0.99982 | 0.99999 | 0.99987 | 0.99989 | 0.99991 | 0.99992 | 0.05 |
| 0 | 1 | 1 | 1 | 1 | 1 | 1 | 1 | 1 | 1 | 1 | 1 | 0 |

**Table B.1:** Values of $B_n$ dependent on geometric parameters $\alpha$ & $\rho^2$ for use in Grover's formula. Source: [32]

| $\alpha$ | $\rho^2 = 0.5$ | 0.45 | 0.4 | 0.35 | 0.3 | 0.25 | 0.2 | 0.15 | 0.1 | 0.05 | $\rho^2 = 0$ | $\alpha$ |
|---|---|---|---|---|---|---|---|---|---|---|---|---|
| 1 | 0.9718 | 0.97718 | 0.98194 | 0.98612 | 0.98974 | 0.99282 | 0.99535 | 0.99735 | 0.9988 | 0.99969 | 1 | 1 |
| 0.95 | 0.97428 | 0.97919 | 0.98354 | 0.98736 | 0.99066 | 0.99346 | 0.99577 | 0.99759 | 0.99891 | 0.99972 | 1 | 0.95 |
| 0.9 | 0.97668 | 0.98114 | 0.98509 | 0.98855 | 0.99155 | 0.99409 | 0.99618 | 0.99783 | 0.99902 | 0.99975 | 1 | 0.9 |
| 0.85 | 0.97901 | 0.98302 | 0.98658 | 0.9897 | 0.9924 | 0.99469 | 0.99657 | 0.99805 | 0.99912 | 0.99978 | 1 | 0.85 |
| 0.8 | 0.98124 | 0.98483 | 0.98801 | 0.9908 | 0.99322 | 0.99526 | 0.9997 | 0.99827 | 0.99922 | 0.9998 | 1 | 0.8 |
| 0.75 | 0.98338 | 0.98656 | 0.98938 | 0.99185 | 0.99399 | 0.99581 | 0.9973 | 0.99847 | 0.99931 | 0.99983 | 1 | 0.75 |
| 0.7 | 0.98541 | 0.9882 | 0.99068 | 0.99285 | 0.99473 | 0.99633 | 0.99764 | 0.99866 | 0.9994 | 0.99985 | 1 | 0.7 |
| 0.65 | 0.98732 | 0.98975 | 0.9919 | 0.9938 | 0.99543 | 0.99682 | 0.99795 | 0.99884 | 0.99948 | 0.99987 | 1 | 0.65 |
| 0.6 | 0.98913 | 0.99121 | 0.99306 | 0.99467 | 0.99608 | 0.99727 | 0.99825 | 0.99901 | 0.99956 | 0.99989 | 1 | 0.6 |
| 0.55 | 0.99082 | 0.99257 | 0.99413 | 0.9955 | 0.99669 | 0.9977 | 0.99852 | 0.99916 | 0.99963 | 0.9999 | 1 | 0.55 |
| 0.5 | 0.99237 | 0.99383 | 0.99512 | 0.99626 | 0.99725 | 0.99809 | 0.99877 | 0.99931 | 0.99969 | 0.99992 | 1 | 0.5 |
| 0.45 | 0.99379 | 0.99498 | 0.99603 | 0.99696 | 0.99776 | 0.99844 | 0.999 | 0.99944 | 0.99975 | 0.99994 | 1 | 0.45 |
| 0.4 | 0.99508 | 0.99601 | 0.99685 | 0.99759 | 0.99823 | 0.99877 | 0.99921 | 0.99955 | 0.9998 | 0.99995 | 1 | 0.4 |
| 0.35 | 0.99622 | 0.99694 | 0.99758 | 0.99815 | 0.99864 | 0.99905 | 0.99939 | 0.99966 | 0.99985 | 0.99996 | 1 | 0.35 |
| 0.3 | 0.99721 | 0.99774 | 0.99822 | 0.99864 | 0.999 | 0.9993 | 0.99955 | 0.99975 | 0.99989 | 0.99997 | 1 | 0.3 |
| 0.25 | 0.99806 | 0.99843 | 0.99876 | 0.99905 | 0.9993 | 0.99952 | 0.99969 | 0.99982 | 0.99992 | 0.99998 | 1 | 0.25 |
| 0.2 | 0.99875 | 0.99899 | 0.9992 | 0.99939 | 0.99955 | 0.99969 | 0.9998 | 0.99989 | 0.99995 | 0.99999 | 1 | 0.2 |
| 0.15 | 0.9993 | 0.99943 | 0.99955 | 0.99966 | 0.99975 | 0.99982 | 0.99989 | 0.99994 | 0.99997 | 0.99999 | 1 | 0.15 |
| 0.1 | 0.99969 | 0.99975 | 0.9998 | 0.99985 | 0.99989 | 0.99992 | 0.99995 | 0.99997 | 0.99999 | 1 | 1 | 0.1 |
| 0.05 | 0.99992 | 0.99994 | 0.99995 | 0.99996 | 0.99997 | 0.99998 | 0.99999 | 0.99999 | 1 | 1 | 1 | 0.05 |
| 0 | 1 | 1 | 1 | 1 | 1 | 1 | 1 | 1 | 1 | 1 | 1 | 0 |

**Table B.2:** Continued: Values of $B_n$ dependent on geometric parameters $\alpha$ & $\rho^2$ for use in Grover's formula. Source: [32]

# Appendix C

# Spatial voltage distribution in coil

*The Figures on the following pages depict the spatial voltage distribution in the coil as a function of time, after current chopping. Figure C.1 shows the turn voltage, which would be measured by fixing one terminal of a voltmeter at turn one and the other at the turn specified on the z-axis. Figures C.2, C.3 and C.4 show the turn to turn voltage. This voltage could be measured by attaching the voltmeter to adjacent turns. Thus, the turn voltage is the integration of the turn to turn voltage over the number of turns.*

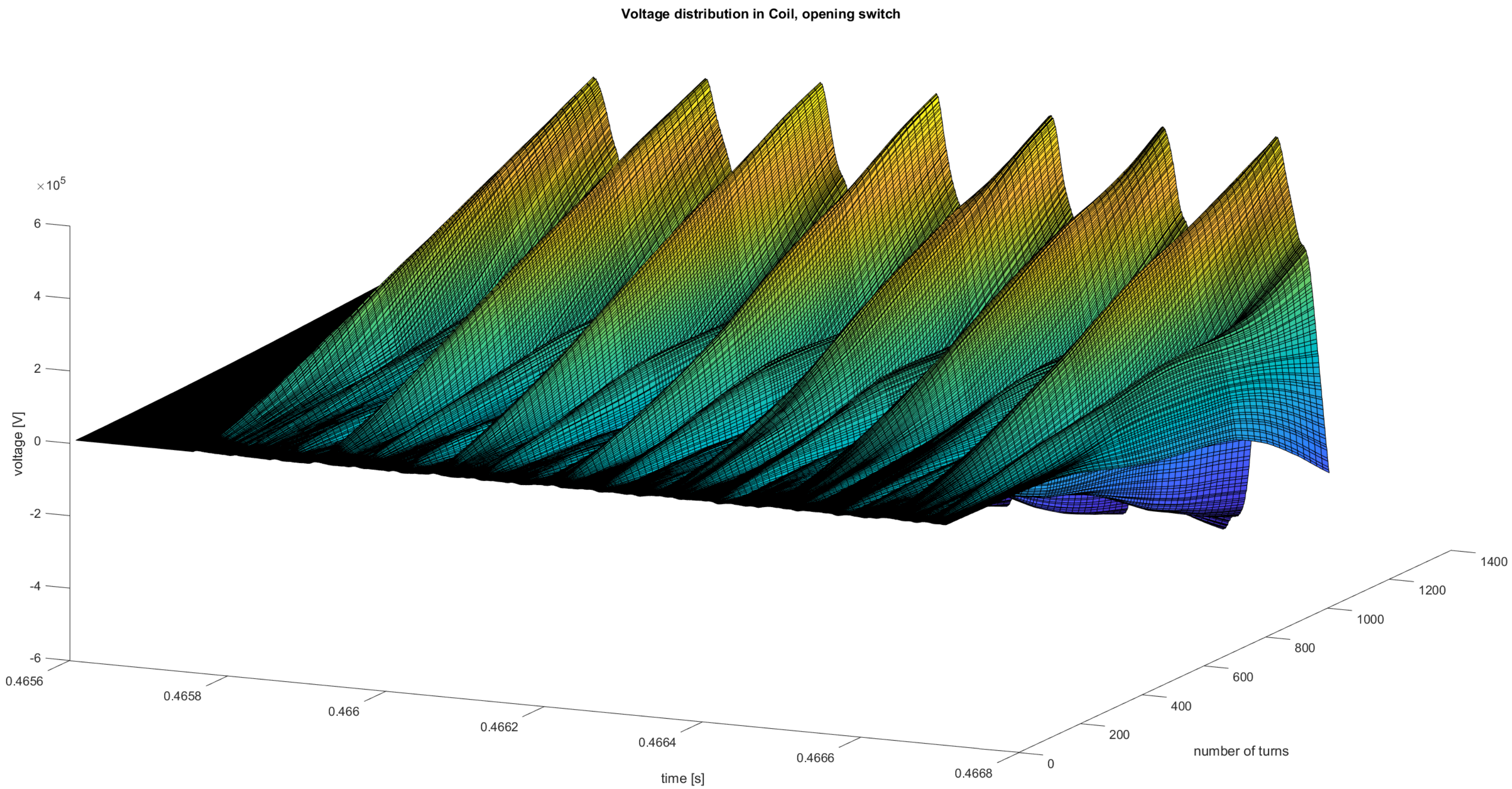


**Figure C.1:** Spatial voltage distribution in coil after current chopping as turn voltage

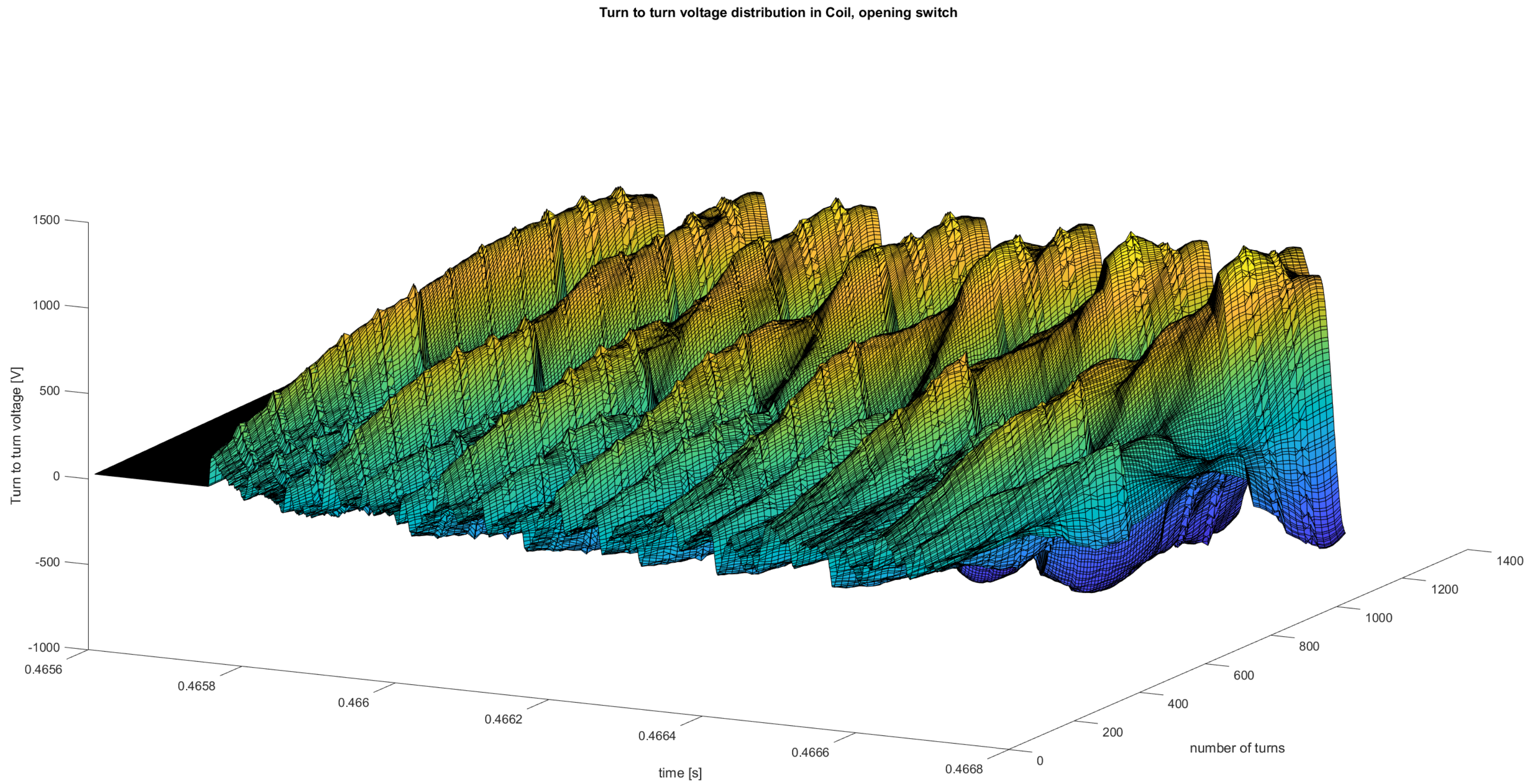


**Figure C.2:** Spatial voltage distribution in coil after current chopping as turn to turn voltage

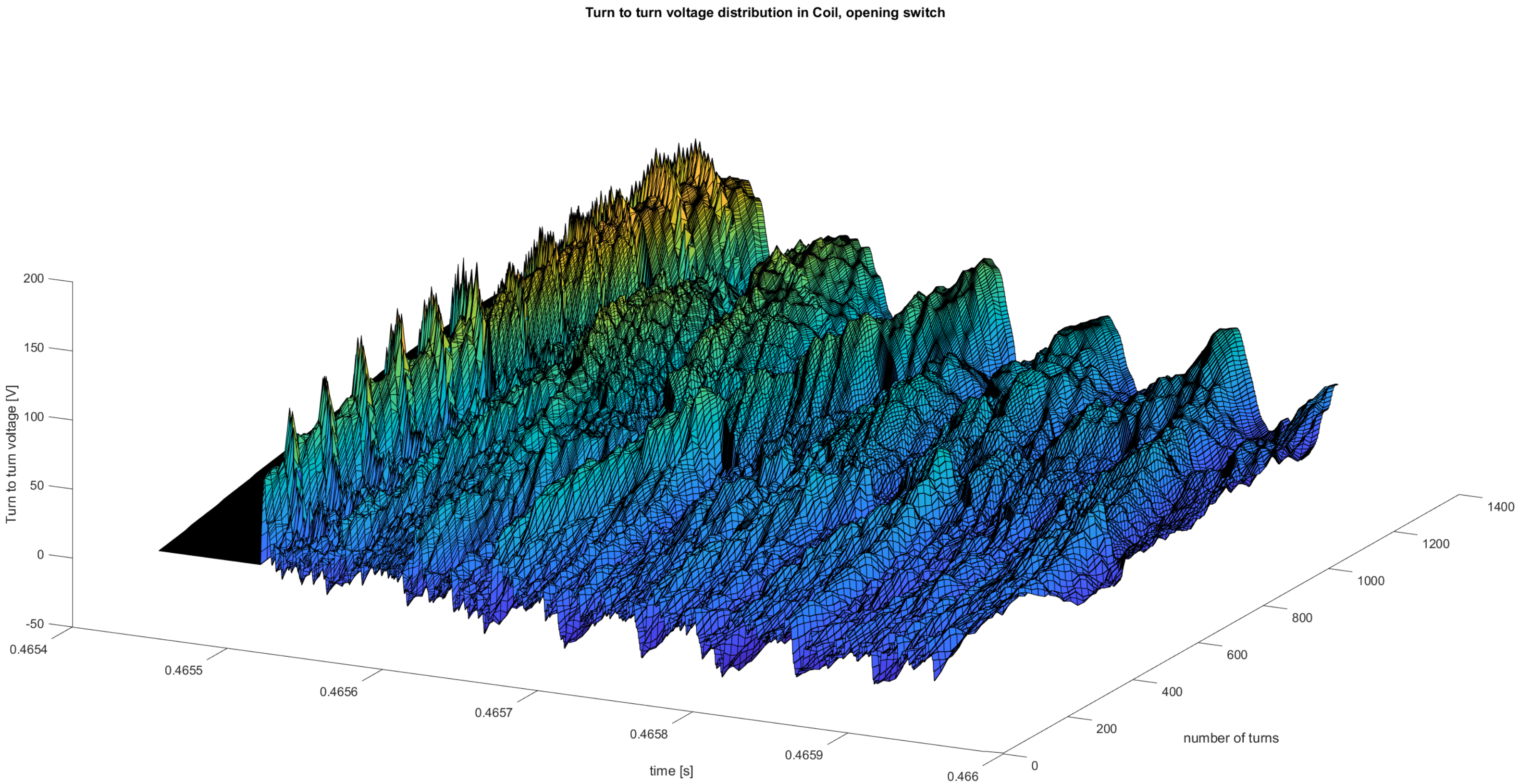


**Figure C.3:** Spatial turn to turn voltage distribution in coil after current chopping with optimised snubber circuit

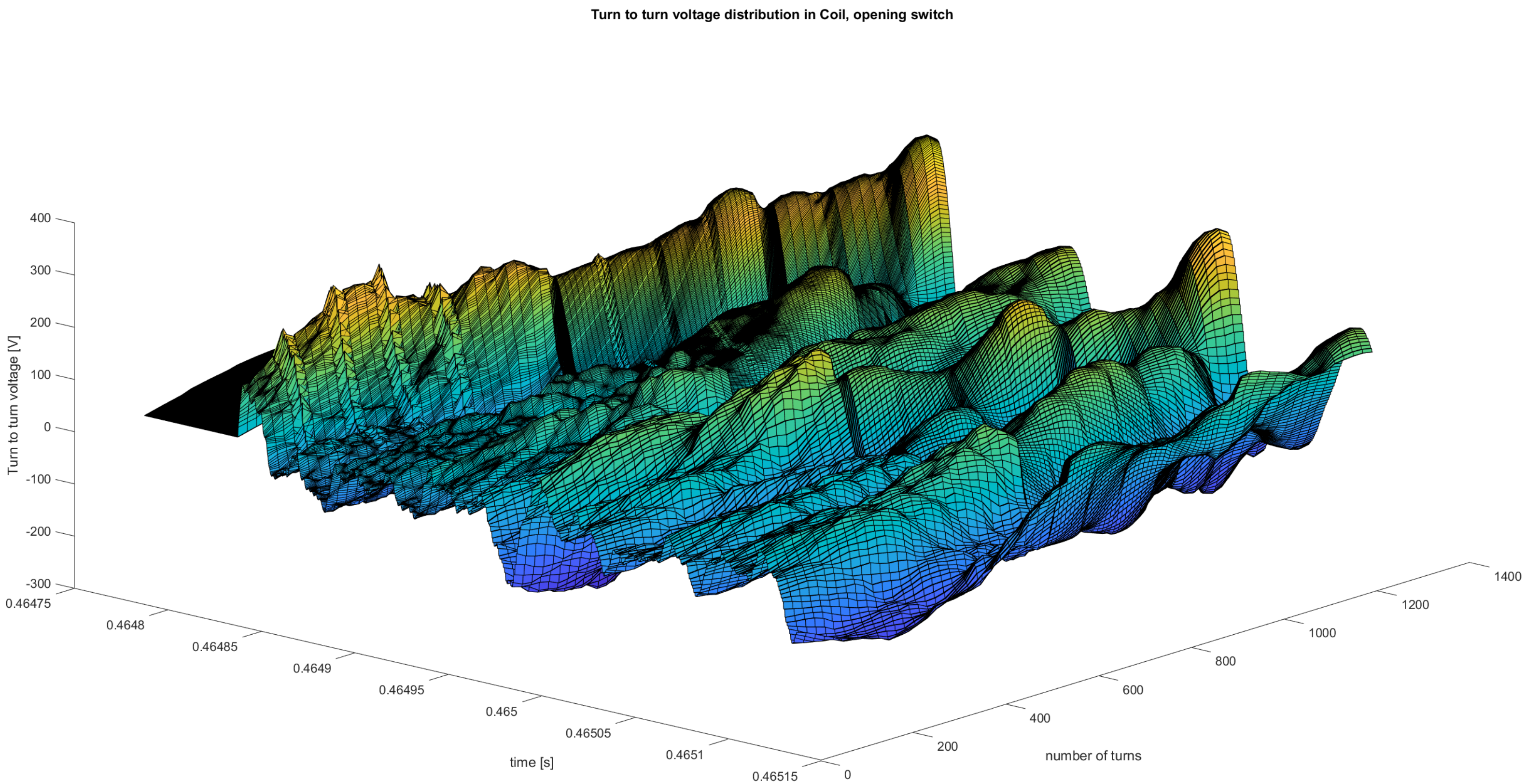


**Figure C.4:** Spatial voltage distribution in partly energised coil after current chopping as turn to turn voltage